NTNU
Norwegian University of
Science and Technology

Lead-free piezoelectric materials for medical application

Silje Marie Dale

Chemical Engineering and Biotechnology
Submission date: March 2018
Supervisor: Mari-Ann Einarsrud, IMA
Co-supervisor: Nikolai Helth Gaukås, IMA
Julia Glaum, IMA

Norwegian University of Science and Technology
Department of Materials Science and Engineering

Preface

This thesis is submitted to the Norwegian University of Science and Technology (NTNU), as part of the requirements for the degree of Master of Science. The work presented in this thesis has been carried out at the Department of Materials Science and Engineering at NTNU, between October 2017 and March 2018. Professor Mari-Ann Einarsrud has supervised the work, and Assoc. Professor Julia Glaum, Ph.D. candidate Nikolai Helth Gaukås and Professor Tor Grande have served as co-supervisors. The nanoindentation experiments was performed by Professor Jianying He at the NTNU Nanomechanical Lab, and sputtering of Pt-electrodes onto the film surface before ferroelectric measurements was conducted by Nikolai Helth Gaukås. All of the other work presented in this paper is performed by the author.

Acknowledgment

The work conducted during this thesis has been challenging, but also inspiring and a very educational experience, and several people deserve recognition for their contributions to the project.

First of all, I would like to give a special thank to my main supervisor, Professor Mari-Ann Einarsrud. Your impressing amounts of knowledge on many topics, and guidance have been very much appreciated. Also, thank you for always believing in my abilities, and for pushing me to trust my instincts and knowledge as a chemist. It has been sometimes challenging, but very inspiring. Secondly, I

would like to thank all of my co-supervisors: Professor Tor Grande, for helpful feedback and discussions during my presentations at the group meetings. Assoc. Professor Julia Glaum, for valuable feedback, support and motivation, and for always having an open door. Ph.D. candidate Nikolai Helth Gaukås, for always being positive and supporting, and for all valuable discussions and motivational help during this project.

I would also like to thank my fellow members of the Research Group on Ferroics, Porous and Nanosynthesis for feedback on presentations and discussions throughout the semester. Special credit goes to Senior Engineer Kristin Høydalsvik Wells for helping out with X-ray diffraction measurements and to Professor Jianying He at NTNU Nanomechanical Lab for performing, and for giving me an introduction to, nanomechanical experiments. It has been very valuable for this study. Finally, I would like to acknowledge the technical staff at NTNU NanoLab and the Department of Materials Science and Engineering for giving me equipment training and help with various technical problems.

Trondheim, 2018-03-23

Silje Dale

Silje Marie Dale

Abstract

In this work, $K_{0.5}Na_{0.5}NbO_3$, (KNN) and $K_{0.495}Na_{0.495}Ca_{0.005}NbO_3$ thin films for biomedical applications have been prepared from an aqueous precursor solutions with 2.5 or 5.0 mol% of alkali excess. Ca^{2+} was introduced as dopant to enhance the hygroscopic properties of KNN. The precursor solutions were deposited on $SrTiO_3$ substrates by spin coating with subsequent pyrolysis at 550 °C and final annealing in air at 700 °C. X-ray diffraction and scanning electron microscopy revealed that 5 mol% alkali excess is necessary to obtain phase pure thin films with homogeneous microstructure.

Nanoindentation was used to investigate the effect of doping with 0.5 mol% Ca^{2+}, on the hygroscopicity of KNN thin films. This was done by looking at the change in mechanical properties after exposure the films to an aqueous solution at 37 °C for 0 to 14 days. The mechanical properties showed relatively small changes after soaking, and only marginally improved stability of the mechanical properties was observed with Ca^{2+} doping.

Although both KNN and Ca-KNN thin films displayed weak and leaky ferroelectric hysteresis loops, doping with 0.5 mol% Ca^{2+} subtly improved the saturation polarisation, and slightly enhanced the piezoelectric coefficient (18.6 ±0.16 $\mathrm{pC\,N^{-1}}$) compared to pure KNN thin films (17.44 ±0.69 $\mathrm{pC\,N^{-1}}$).

The results from this work imply that further improvements of the ferroelectric and piezoelectric properties are necessary. However, the mechanical measurements are promising, and show that KNN thin films are potential candidates for biomedical applications.

Sammendrag

I denne masteroppgaven har det blitt fremstilt $K_{0.5}Na_{0.5}NbO_3$ (KNN) og $K_{0.495}Na_{0.495}Ca_{0.005}NbO_3$ (Ca-KNN) tynnfilmer, for biomedisinske applikasjoner, fra en vannbasert forløperløsning med 2.5 eller 5.0 mol% alkalioverskudd. Ca^{2+} ble brukt som dopant for å forbedre de hygroskopiske egenskapene til KNN. Forløperløsningen ble deponert på $SrTiO_3$ substrater før spin coating og påfølgende pyrolyse ved 550 °C, og gløding i luft ved 700 °C. Røngendiffraksjon og elektronmikroskopi viste at 5.0 mol% alkalioverskudd var nødvendig for å lage faserene tynnfilmer med homogen mikrostruktur.

Nanoinntrykk-målinger ble utført for å undersøke hvordan doping med 0.5 mol% Ca^{2+} påvirker de hygroskopiske egenskapene til KNN tynnfilmer. Dette ble undersøkt ved å se på hvordan de mekaniske egenskapene endres etter 0 og 14 dager i vannløsning ved 37 °C. Oppholdet i vannløsningen ga lite endring i de mekaniske egenskapene, og kun marginal forbedring av de mekaniske egenskapenes stabilitet ble observert ved Ca^{2+}-doping.

Selv om både KNN- og Ca-KNN-tynnfilmer hadde svake ferroelektriske hystereseløkker med spor av lekkstrøm, viste 0.5 mol% Ca^{2+}-doping en subtil økning av mettet polarisasjon, og noe forbedret piezoelektrisk koeffisient (18.6 ± 0.16 pCN^{-1}) sammenlignet med udopet KNN-tynnfilmer (17.44 ± 0.69 pCN^{-1}).

Resultatene fra denne oppgaven tilsier at det er nødvendig å forbedre de ferroelektriske og piezoelektriske egenskapene. Likevel er de mekaniske målingene lovende, og viser at KNN-tynnfilmer er potensielle kandidater for *in vivo* biomedisinske applikasjoner.

Contents

Preface i

Acknowledgment i

Abstract iii

Sammendrag v

1 Motivation 1

2 Introduction 5

2.1 Piezoelectricity 5

2.1.1 Basic principles of ferroelectricity 6

2.1.2 Ferroelectric domains and hysteresis loops . . 6

2.1.3 Perovskite oxide ferroelectrics 8

2.2 Biomaterials 9

2.2.1 Development of biomaterials 10

2.2.2 Material selection 11

2.3 Potassium Sodium Niobate (KNN) 12

2.3.1 Structure and properties 13

2.3.2 Modifications of KNN 15

2.4 Deposition of oxide thin films 16

2.4.1 Chemical solution deposition 16

2.4.2 Synthesis of KNN thin films 22

2.4.3 KNN thin films for biomedical applications . . 24

2.5 Mechanical properties of thin films 26

2.5.1 Nanoindentation 26

2.5.2 Mechanical properties of KNN thin films . . . 29

3 Experimental 31

3.1 Solution preparation 33

3.1.1 Niobium precursor solution 33

3.1.2 Calcium precursor solution 35

3.1.3 $K_{0.5}Na_{0.5}NbO_3$ 35

3.1.4 $K_{0.495}Na_{0.495}Ca_{0.005}NbO_3$ 36

3.2 Thin film preparation 37

3.2.1 Solution deposition 37

3.3 Characterisation 38

3.3.1 Powder characterisation 38

3.3.2 Thin film characterisation 40

4 Results 45

4.1 Precursor properties 45

4.1.1 Stochiometry of the precursor solutions 45

4.1.2 Crystal structure of calcined powders 46

4.1.3 Termogravimetric analysis 48

4.2 Thin film properties 48

4.2.1 Phase purity and solubility measurements . . 48

4.2.2 Surface morphology and film thickness 51

4.2.3 Mechanical properties 60

4.2.4 Piezo- and ferroelectric properties 64

5 Discussion 67
5.1 Precursor stability and phase purity 67
5.1.1 Effect of alkali excess 68
5.1.2 Effect of doping with calcium 70
5.2 Thin film properties 70
5.2.1 The effect of alkali excess 71
5.2.2 The effect of heating rate 73
5.2.3 The effect of doping with calcium 74
5.3 Further work 80

6 Conclusion 83

Bibliography 84

A Thermal treatments 93
A.1 Thermogravimetric standardisation 93
A.2 Calcination temperatures 94

B Additional x-ray diffractograms 97

C Pawley refinements 103

D Surface morphology 105

E Nanoindentation 111

Chapter 1

Motivation

The piezoelectric effect was first discovered in 1880 by the Curie brothers, Jacques and Pierre, and is the phenomenon where a mechanical field induces an electric polarization, or vice verse, where an electric field causes macroscopic strain.[1] State of the art materials for commercial piezoelectric applications have been based on lead-containing ceramics, such as lead zirconate titanate (PZT).[2] In 2003, a directive on the restriction of hazardous substances (RoHS) by the European Union limited the use of lead in electrical and electronic equipment due to the toxicity of lead.[3] Although exceptions being made for materials such as PZT in piezoelectric devices, due to the lack of suitable alternatives, the directive has motivated search for lead-free piezoelectric ceramics with comparable properties to PZT.[2,4]

The use of piezoceramics in medical technology is widespread, and among the applications are ultrasonic transducers for medical imaging, medical sensors, drug delivery (micro)devices, and actuators in micropumps and switches. Although most of these applications are used *ex vivo*, medical technology is rapidly developing to improve tools for medical treatment and diagnosis. Further advances rely on development of implants, actuators and sensors to be used *in vivo*. Thus, new piezoelectric materials for *in vivo* applications need to be biocompatible and without any toxic elements. For most biomedical applications, the chemical and mechanical properties of the implanted material are of great importance. Interaction between the host environment and the implanted device may change the material's properties over time. These changes must be anticipated and accounted for when selecting and designing new materials for biomedical applications.

Among the lead-free piezoelectric candidates, potassium sodium niobate ($K_{0.5}Na_{0.5}NbO_3$, KNN) has shown promising results with respect to toxicity for use *in vivo*,[5,6] and also encouraging piezoelectric performance.[7] Most studies on KNN thin films to date have focused on the electrical properties,[2,4,7–12] and less on mechanical properties.[8,13,14] Reports on how mechanical properties and surface characteristics of KNN are affected when thin films are exposed to water solutions are scarce. It is crucial to understand these properties, and also how they change over time when introducing KNN *in vivo*, in order to evaluate the potential use of KNN as an implantable piezoelectric material. A major problem in KNN is the volatility of Na and K during processing. The evaporation of Na and K affects the stochiometry, leading to changes in properties and influencing the hygroscopic nature of the material.[4] The standard method to compensate these losses, and obtain phase pure KNN, is by adding excess amount of alkali metals to the precursor solutions.[2,4] Also, substitution of alkaline earth metals at the A-site may improve the hygroscopic and piezoelectric properties of KNN thin films.[11,13]

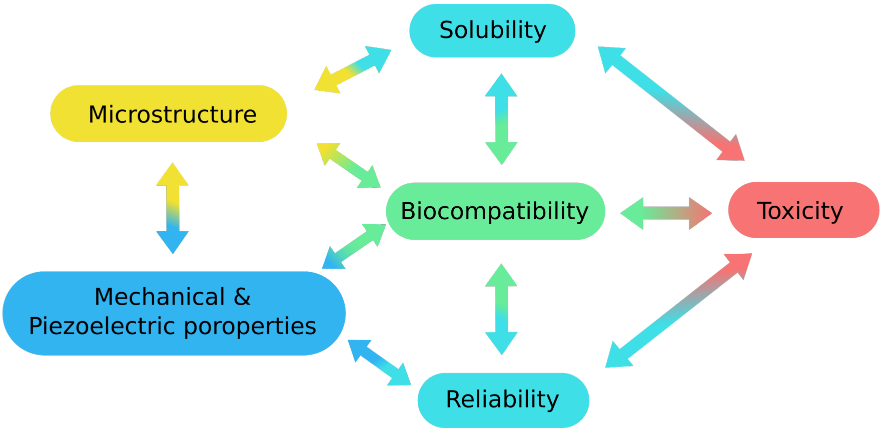

Figure 1.1: Schematic presentation of the coupling between material properties and important considerations when designing a piezoceramic for use inside the body.

Aim of work

Chemical solution deposition is a common and inexpensive technique for preparing KNN thin films. However, most studies are usually based on expensive metal-alkoxides mixed with toxic organic solvents.[10,15,16] Hence, a cheap and non-toxic synthesis route is strongly preferable. Piezoelectric materials for implantable devices must have appropriate mechanical and ferroelectric properties. Figure 1.1 shows the connection between some important properties and considerations when designing piezoelectric materials for use *in vivo*.

This master's thesis aims to develop piezoelectric KNN-based thin films for biomedical applications through an environmentally friendly synthesis route. The main objective is to study how the microstructure, phase purity and mechanical properties may change when the films are exposed to a biological environment. KNN and calcium-modified KNN thin films will be prepared by chemical solution deposition of an aqueous precursor solution. Chemical stability and mechanical properties of thin films upon exposure to a biological environment will be studied in a simplified system of water at 37 °C over different lengths of time. The effect of adding low amounts of Ca^{2+} (0.5 mol%) on the solubility of KNN thin films will be studied by nanoindentation and pH measurements. Ferroelectric and piezoelectric (d_{33}) measurements will be conducted to evaluate the performance of the films. Also, the effect of alkali excess in the precursor solutions on the phase purity and microstructure of the films will be investigated by adding different amounts of alkali excess to the precursor solutions.

Chapter 2

Introduction

2.1 Piezoelectricity

A piezoelectric material generates an electrical charge when pressure, or mechanical stress, is applied. This is also known as the *direct* piezoelectric effect. This effect is also reversible, where an applied electric field produces mechanical strain in the material, causing it to contract or expand (*converse* piezoelectric effect).[1] The piezoelectric effect is illustrated in Figure 2.1. In order for piezoelectricity to exist several properties are required. The material has to be dielectric, or non-conductive, meaning that the material will polarise and not allow charge transport. The material must also possess one polar axis and the the crystal structure must be non-centrosymmetric.

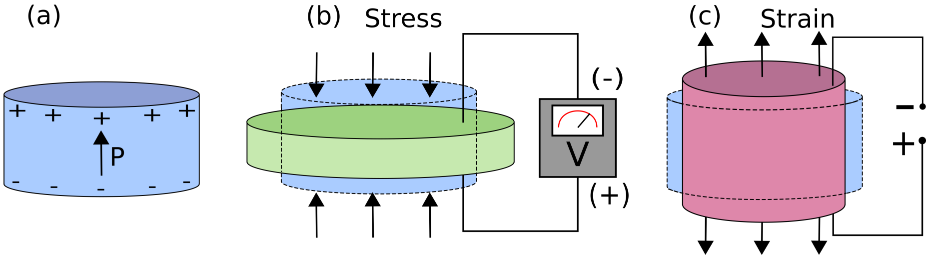

Figure 2.1: Illustration of the piezoelectric effect: (a) A crystal with an internal polarisation. (b) The direct effect: Generation of an electric voltage when mechanical stress is applied. (c) The converse effect: Generation of strain when an electric field is applied.[17,18]

2.1.1 Basic principles of ferroelectricity

Ferroelectric materials are a subgroup of the pizoelectric materials, which means that all ferroelectrics are piezoelectric, but not all piezoelectrics are necessarily ferroelectric. A general definition of a ferroelectric, is a material which has a electric polarisation that can be reversed by an applied electric field. Most ferroelectrics have a phase-transition temperature, T_C, and above this temperature they become paraelectric. The switchable polarisation in a ferroelectric material makes it possible to *pole* the material, and make a ferroelectric polycrystalline material macroscopically polarised. Thus, a ferroelectric material has a remanent polarisation. A material can be piezoelectric without being ferroelectric, but a polycrystalline material must be ferroelectric in order to align individual polarisation directions and create an overall net polarisation. Piezoelectricity can be predicted from the point group symmetry of the material, while ferroelectricity needs to be experimentally verified.

2.1.2 Ferroelectric domains and hysteresis loops

One common feature in ferroelectric materials is the existence of ferroelectric domains, which is defined as regions with uniform spontaneous polarisation. Adjacent domains are separated by domain walls, where the geometry is determined by the crystal symmetry.[19,20] In order to understand ferroelectric performance it is important to study how the domains respond to external factors such as temperature, stress and electric field. A defining feature of ferroelectrics is the ferroelectric hysteresis loop, as shown in Figure 2.2. Every ferroelectric material has its own unique hysteresis loop where

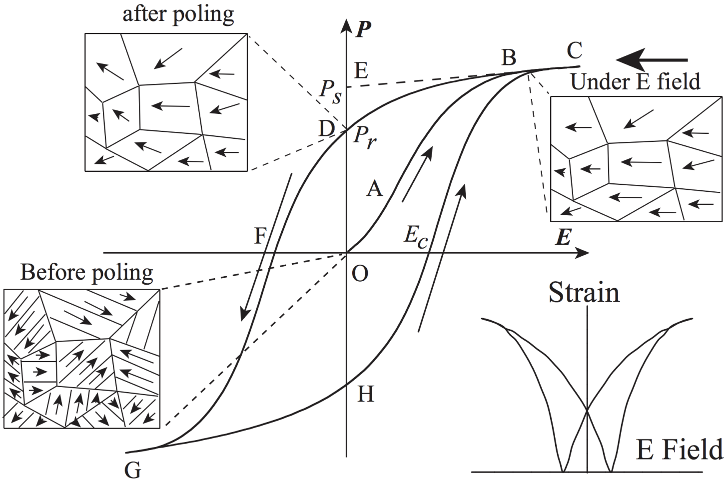

Figure 2.2: Ferroelectric hysteresis (P-E) loop with corresponding strain-electric field curve. (P_s), (P_r) and (E_c) are the saturation and remanent polatisation, and the coercive field, respectively. Some of the domain structures at selected stages are included.[19]

characteristic parameters such as coercive field (E_c), saturation polarisation (P_s) and remanent polarisation (P_r) can be determined. An unpoled ferroelectric ceramic usually has a zero net polarisation. When introducing an external electrical field, the spontaneous polarisation direction within the domains can be switched. This is also known as poling, in which the domains well aligned with the applied field will grow on the expense of the less aligned domains, resulting in a maximum attainable alignment of polarisation (P_s) in the material. When the applied field is removed, most of the altered domains will remain in their new state, resulting in a permanent polarisation (P_r) in the material and giving rise to macroscopic piezoelectric behaviour. At negative field strengths, the domains reorient and realign in the opposite direction.

2.1.3 Perovskite oxide ferroelectrics

Ferroelectricity was first discovered in Rochelle salt (single-crystal) in 1921 and further in polycrystalline barium titanate ($BaTiO_3$) during the mid 1940s.[1,2] Some well known ferroelectric ceramics are the tungsten-bronzes, hexagonal manganites, phyrochlores, bismuth layered structures and perovskites. Most of the common ferroelectric ceramics are oxides with a perovskite structure such as barium titanate (BT), bismuth sodium titanate (BNT), barium zirconate titanate (BZT), lead zirconate titanate (PZT) and potassium sodium niobates (KNN).[2]

Structure

A general illustration of the perovskite (ABO_3) structure is given in Figure 2.3 (a), showing the ideal cubic perovskite structure of KNN. The A-cations (Na and K) are 12-fold coordinated with respect to oxygen, and the B-cation (Nb) is octahedrally coordinated by oxygen. The stability and symmetry of the perovskite structure can be predicted from the Goldschmidt tolerance factor[21,22] (t) given in Equation 2.1, based on the radii (r_i) of the A-site, B-site and O-ions.

$$t \; \frac{r_A+r_O}{\sqrt{2}(r_B+r_O)} \tag{2.1}$$

The ideal cubic perovskite structure is found to when the tolerance factor is close to 1. However, the tolerance factor in perovskites are known to vary from 0.8-1.06.[21] For $t > 1$ the A-cation is larger or the B-cation is slightly smaller than required, causing a tetragonal distortion in the unit cell (Figure 2.3 (b)). Or, if the A-site cation is

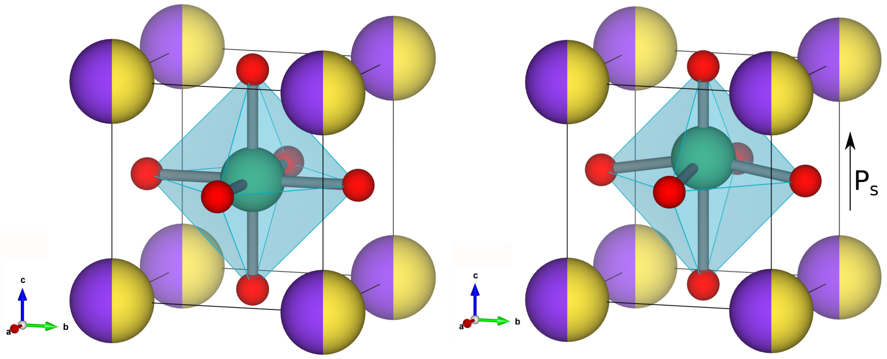

(a) (b)

Figure 2.3: Two different polymorphs of KNN. Sodium and potassium are represented by yellow and purple color respectively, oxygens are red and niobium in green. (a) Illustrates the non-piezoelectric cubic structure (P$m\bar{3}m$) and (b) illustrates the tetragonal structure (P4mm), one of the KNN polymorphs which exhibit piezoelectric properties. The structures were created by using the VESTA software.[23]

too large (t>1.06) hexagonal face-sharing polytypes will be formed. If $t < 1$, the A-site cations are to small resulting in tilting and rotation of the BO_6 octahedra, giving rise to either orthorhombic or rhombohedral distortion of the perovskite structure.[2]

2.2 Biomaterials

Biomaterials are materials designed to interact with with biological systems, primarily used for medical purposes.[24] Some well known biomaterial applications are heart valve protheses, artificial hip joints, dental implants and pacemakers. The concept of biocompatibility is important and essential when designing new biomaterials. Whether or not there exists a precise definition of biocompatibility is still argued, and the definition has evolved throughout the years, depending on the intention of the implanted biomaterial.[24,25] The modern definition is *"the ability of a material to perform with an appropriate host response in a specific situation"*.[26] This broad term is not only dependent on the characteristics of the material, but also on the situation in which the material is used. Given this term, no material can be assumed to be universally biocompatible, since a material designed for e.g. the kidney, will not necessarily be suitable for every conceivable application inside the body.

2.2.1 Development of biomaterials

Today, biomaterials are widely used in medical applications and dentristy, but the word "biomaterial" is relatively new. Although, biomaterials have been used since the earliest days of human civilisation,[24] this section will focus on the foundation of biomaterials between the 1940s and 1980s, and how these are connected to the development of new biomaterials.

The first generation of biomaterials, or implantable devices, developed from the 1940s to the 1980s was intended to remain in the body for a long time. Common for these materials were their "biological inertness". These *bioinert* or *biopassive* materials were designed to reduce the immune response from the body on the implanted materials.[25,27] During the 1980s the development of *"bioactive"* materials started, and instead of being ignored by the biological tissue, the materials were designed to specifically interact. Materials such as glass-ceramics, bioactive glasses, ceramics and composites were taken into use as bioactive materials for dental and orthopedic applications. Materials constructed to chemically break down inside the body were also developed in this second generation of biomaterials. One example of these "resorbable biomaterials" is biodegradable suture made of polymers.[28] While the second generation of biomaterials were designed to either be bioactive or resorbable, the third generation of biomaterials are designed to stimulate cellular responses. Thus, this biomaterials combines the bioactive and resorbable properties to help the body to heal itself.[27]

2.2.2 Material selection

During the last decades, advances have been made in the development of new biomaterials. The definiton of biocompatibility has evolved and become more broad, depending not only on the material's characteristics, but also the situation in which they are used. Surface characteristics and mechanical properties of the biomaterial becomes important in the interaction process between the host and the implanted material. These interactions are ongoing throughout the lifetime of the material, and some general criteria should be taken in consideration when selecting materials for new implantable devices. Also, economic aspects are important when selecting materials, and it is beneficial to choose inexpensive and abundant materials. Some important material properties are given in Table 2.1.

Figure 2.4 shows the cost and toxicity of potential elements of interests when developing new lead-free piezoelectric ceramics. Materials such as cadmium (Cd), thallium (Tl), antimony (Sb) and lead (Pb) are marked as toxic, while sodium (Na), calcium (Ca), aluminium (Al) and niobium (Nb) are regarded non-toxic. It is noteworthy that potassium is regarded slightly toxic, as elevated levels (higher than 5.5 $\mathrm{mmol\,L^{-1}}$) of K^+ in the blood might increase the risk

Table 2.1: General considerations when selecting lead-free materials for piezoelectric and biomedical applications,[2,24,29,30] reprinted from.[17]

Property	**Criterion**
Biocompatibility	It has to perform with a proper host response inside the body i.e. it has to be non-toxic, blood-compatible and non-allergic.
Physical properties	Proper strength, flexibility, degradation resistance and resistance to sterilisation techniques.
Reliability	Proper performance and durability dependent on the time scale in which the host is exposed to the implantable device.
Cost and sustainability	The use of inexpensive and non-rare raw materials, as well as inexpensive and environmentally friendly processing routes are beneficial.

of hyperkalemia which causes muscle weakness, muscle pains, and in the worst-case abnormal heart rate that may result in death.[31]

2.3 Potassium Sodium Niobate (KNN)

Among the most investigated lead-free piezoelectric materials are the alkali-niobates, $K_xNa_{1-x}NbO_3$ (KNN), due to large piezoelectric coefficient, d_{33}, and high T_c.[2,4] Although the ferroelectricity in KNN was discovered in the early 1950s,[32–34] the major breakthrough for the material happened in 2004. That year, Saito *et al.*[7] reported a superb piezoelectric coefficient of $d_{33} = 416$ pCN^{-1} in textured KNN, modified with lithium (Li), tantalum (Ta) and antimony (Sb). This discovery lead to an increased interest in KNN-based materials and other lead-free piezoceramics.[2,8,9]

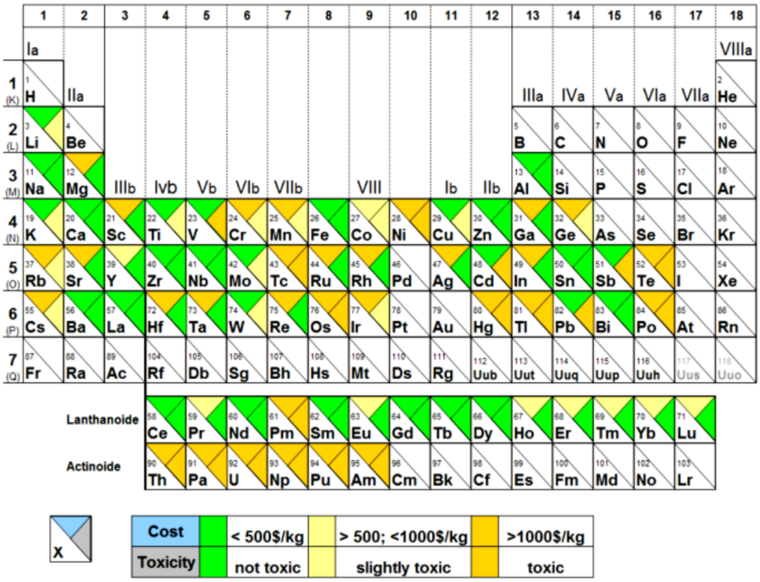

Figure 2.4: Periodic table, illustrating the relative cost and toxicity of interesting elements. The toxicity degree of the elements is divided into three categories, non-toxic, slightly toxic and toxic, when they are prepared as either carbonates or oxides.[2]

2.3.1 Structure and properties

The term KNN is often used in reference to different compositions of the solid solution between $KNbO_3$ (KN) and $NaNbO_3$ (NN), though unless something else is specified, KNN refers to the composition at x = 0.5. Both KN and NN are perovskites and orthorhombic at room temperature. KN is ferroelectric and goes through the following polymorphs: Cubic (C) above ~435 °C, tetragonal (T) below 435 down to ~225 °C, orthorhombic (O) from ~225 °C down to room temperature and rhombohedral (R) below −10 °C. NN was originally reported as ferroelectric,[32] but later as antiferroelectric[35] and has a more complexed polymorphism than KN, due to oxygen octahedral

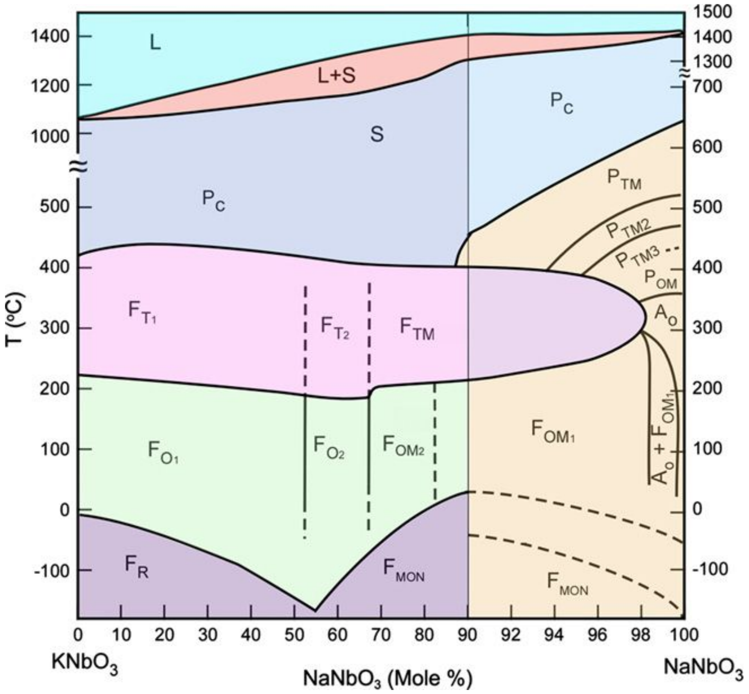

Figure 2.5: Phase diagram of the pseudo-binary KNbO3-NaNbO3 system, from Jaffe *et al.*[1], modified by Li *et al.*[9].

tilting.[9] The polymorphs of KNN are the same as for KN, but with slightly lower phase transition temperatures. A pseudo-binary phase diagram of the KN-NN-system is shown in Figure 2.5.[1,9]

As mentioned previously, KNN is regarded as orthorhombic at room temperature. However, recent publications suggests that the unit cell has a small monoclinic distortion with 90.32°$\leq \beta \leq$ 90.34°.[36,37] This small distortion may be the reason why many publications report the use of an orthorhombic unit cell for refinements of the cell parameters of KNN at room temperature.[4,13,14]

2.3.2 Modifications of KNN

When developing new ferroelectric materials, construction or utilisation of phase boundaries becomes important, since piezoelectric response usually increases close to a phase transition.[9] Two important phase boundaries are the morphotropic phase boundary (MPB) and polymorphic phase boundary (PPB). The latter is a temperature induced phase transition and appears as a horisontal line in a phase diagram. The temperature dependence makes it hard to utilise in applications with varying temperatures. The first is used to describe a temperature independent transition between two ferroelectric phases, over a narrow change in composition. An example of a system containing a MPB is PZT, which has superior piezoelectric properties. Whether or not KNN posesses a MPB around the composition $x = 0.5$ is debated in the literature,[2,9] although, it is still an agreement that the piezoelectric performance is enhanced close to this composition. Chemical alternations of KNN by using different additives are used to induce PPB's by shifting the phase transition temperatures like T_{O-R}, T_{O-T} and T_C, and enhance the piezoelectric properties of KNN. Equivalent metal ions such as Li^+, Sb^{5+} and Ta^{5+} are commonly used for this purpose, where Li^+ substitutes the A site, and Sb^{5+} and Ta^{5+} the B site.[2,4] Microstructural modifications are also possible for improving the piezoelectric properties and is done by texturing the material, e.g. by forming a microstructure with the same grain orientation. Saito *et al.*[7] used both chemical and structural modification techniques when they successfully reported the aforementioned KNN with superb piezoelectric coefficient.

2.4 Deposition of oxide thin films

Thin films are defined as thin material layers with thickness from nano-metres to several microns.[38] Various deposition techniques can be utilised to produce oxide thin films, and most processes are based on chemical reactions in solids, liquids or gases. When fabricating nanoscale materials the bottom-up and top-down approches are normally used. The latter is a method where the final product is made by using controlled tools to cut, mill or shape it from a bigger piece, while bottom-up approaches creates the structure from smaller building blocks, atom by atom or molecule by molecule. For thin film fabrication, bottom-up approaches are commonly used, and among some of the deposition techniques are physical vapor deposition (PVD), chemical vapor deposition (CVD), and chemical solution deposition (CSD). In PVD, thin films are formed by atoms being transported directly from a source to the substrate through a gas phase without any reactions on the substrate surface, while in CVD, the gas phase precursor reacts or decomposes on the surface of the substrate.

2.4.1 Chemical solution deposition

Chemical solution deposition (CSD) is a rather new technique and the first electronic oxide thin films were prepared by CSD in the 1980s.[40] A general flow chart of the CSD process is illustrated in Figure 2.6. In CSD, thin films are formed during thermal treatment of a starting chemical solution (precursor solution) being deposited by spin coating, dip coating or spray coating.[41] Thermal treatment is usually divided into two different stages: Low-temperature and high-

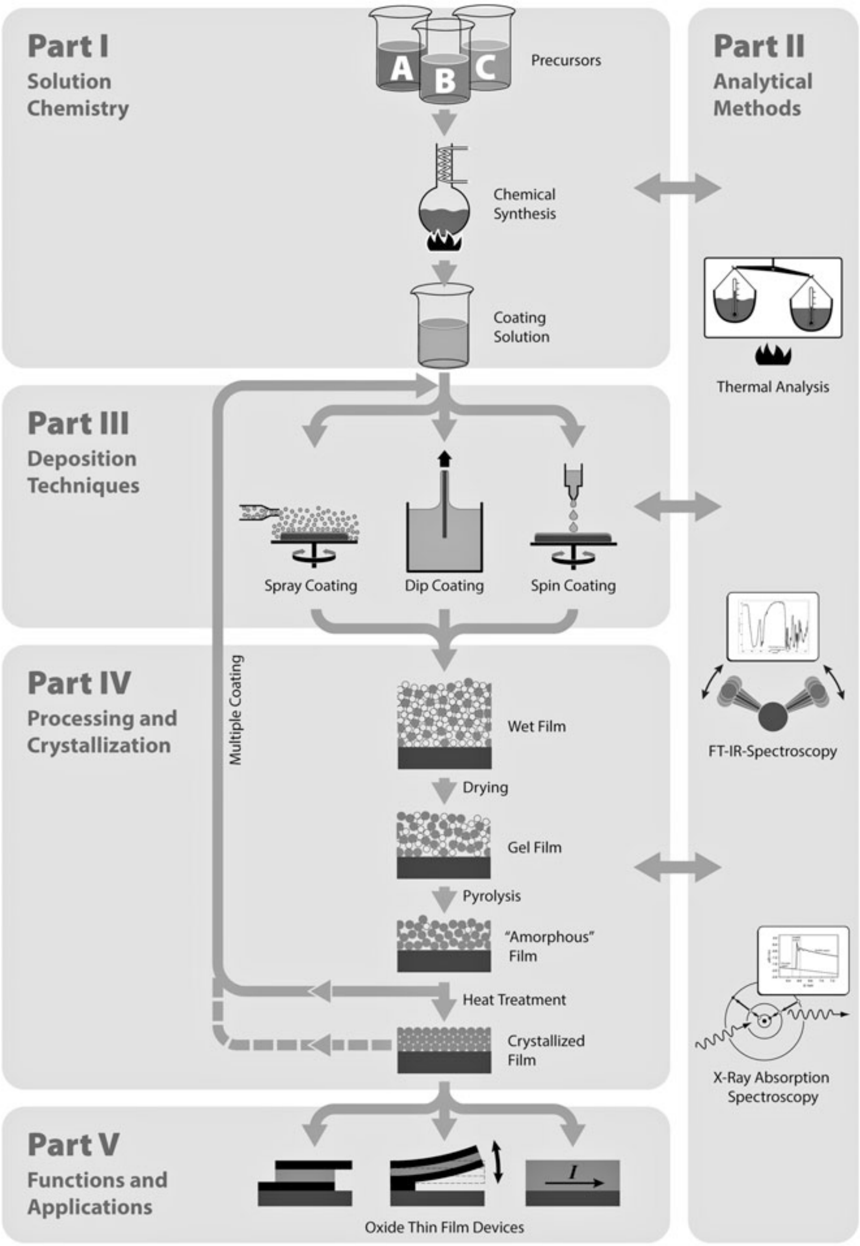

Figure 2.6: Flow chart illustrating the different stages in the chemical solution deposition process, taken form[39].

temperature treatment.[39] The first stage transforms the wet film into a "gel film" before pyrolysis of organic species forms an amorphous film, while the latter is necessary for crystallisation and densification of the film. The main advantages of the CSD process are the control of film composition, relatively low cost and the process is easy to upscale. The main disadvantages are the challenging deposition of ultrathin films (<100 nm) and controlling the microstructure such as texturing.[40]

Considerations

In order to successfully produce thin films by the CSD technique it is important to understand the chemical reactions and physical phenomena during each step of the process. The first part in CSD (Part I, Figure 2.6) starts with the solution synthesis of a precursor system, and some preconditions have to be fulfilled for the precursor system in order to produce a high quality thin film:[17,39,40]

i) **Choice of solvent:** All starting products (metal ions, counter ions and stabilising agents) must be soluble in the solvent.

ii) **Reactivity:** Counter ions or ligands introduced by one metal ion should not lead to precipitation of another metal ion in a multimetal precursor system.

iii) **Long-term stability:** The precursor solution should be stable, without any precipitation for a longer term. One month is a reasonable minimum time.

iv) **Wettability:** The precursor solution should adequately wet the substrate.

v) **Thermal treatment:** All counter ions and ligands should decompose during thermal treatment. Additionally there should be no macroscopic phase separation of the precursor components or crack formation during pyrolysis or crystallisation.

vi) **Environment and cost:** It is advantageous to choose less expensive solvents and starting products as well as non-toxic and environmentally friendly chemicals.

Water-based precursor systems

Most precursor systems for CSD of thin oxide films are based on metal carboxylate or -alkoxide mixed with organic solvents such as 2-methoxy-ethanol (ME). Water-based precursor solutions, with water as solvent, are less costly and more environmentally friendly, which makes them suitable choices for CSD. The most challenging step when making a water-based precursor, especially with high-valent metal ions, is the preparation of a starting solution in which all metal ions are dissolved. When metal salts are solved in water, the metal cation (M^{n+}) is solvated by water molecules. The number of water molecules depends on the size and charge of the metal cation, as well as the polarisation strength. Large cations with low valency, like the alkali metals, have relatively weak electrostatic interactions with water, while increasing valency of the cation will increase the electrostatic interactions leading to stronger covalent character between the cation and the surrounding water molecules. Higher valent metal ions tend to go through *hydrolysis*, where a proton (H^+) is released from the water molecule due to electron transfer from the water molecule orbitals to the metal cation.[39] Aqua ($M-OH_2$) ligands becomes hydroxo ($M-OH$) ligands and further hydrolysis forms oxo (M=O) ligands. The three ligand types are represented in Equation 2.2:

$$[\mathrm{M{-}OH_2}]^{z} \xleftrightarrow{\mathrm{H_2O}} [\mathrm{M{-}OH}]^{(z-1)}\ \mathrm{H_{aq}} \xleftrightarrow{\mathrm{H_2O}} [\mathrm{M{=}O}]^{(z-2)}\ 2\,\mathrm{H_{aq}} \tag{2.2}$$

Both the charge of the cation and the pH of the solution affects the ligand's coordination of the surrounding metal cation.[42] Partially hydrolysed metal ions may undergo condensation reactions leading to precipitation of oxides (acid environments) or hydroxides (alkaline environments). Whether a solution is stable or not depend on a numbers of parameters, such as pH of the solution, concentration of the solution, total ionic concentration, temperature and amount of chelating and stabilising agents. Molecules with electron donor molecular groups (ligands) might be added to compete with the aqua-, oxo- and hydroxo ligands preventing hydrolysis and condensation reactions, and thus stabilise the metal ions in the solution. Examples of ligands used in water-based systems are anions from citric acid, malic acid, oxalic axic and ethylenediaminetetraacetic acid (EDTA).[39,43]

Film crystallisation and microstructure

After deposition the film may be described as a viscoelastic solid containing an inorganic network bound by organic moieties, and solvent trapped within the pore structure of the film. Both the solvent and the organic groups have to be removed from the film prior to the crystallisation, which requires significant structural rearrangement. *Pyrolysis* is often used to describe the heat treatment where the organic groups are removed through decomposition to volatile organic molecules such as CO_2. Pyrolysed films are typically amorphous and may transform into a crystalline state upon further heat treatment (annealing) by a nucleation and growth process.[40]

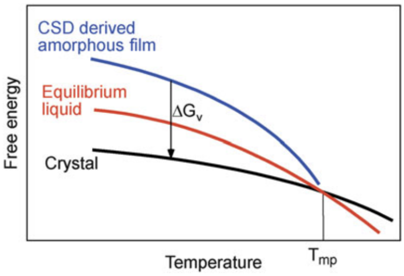

Figure 2.7: Schematic description of the free energy vs. temperature for amporphous, equillibrium liquid and crystalline materials. ΔG_v is the energy difference between amorphous and crystalline state. T_{mp} is the melting temperature.[17,39,40,44]

Figure 2.7 illustrates the differences in free energy (ΔG_v) between the crystalline phase and the solution derived amorphous film. The driving force for both nucleation and growth is related to reduction or minimisation of the Gibbs free energy by forming a new phase. Nucleation is the formation of a distinctive thermodynamic phase. If the nucleation occurs spontaneously and randomly without any preferential nucleation sites, the process is called homogeneous nucleation. Heterogenous nucleation occurs at nucleation sites on surfaces and is more common due to a smaller energy barrier towards the phase transition. Both nucleation and growth rate define the final microstructure of the film. A high nucleation rate and a low growth rate will result in a fine-grained structure, while a low nucleation rate and a high growth rate results in a more coarse-grained structure. Nucleation and growth rate share similar characteristics, but the nucleation rate dominates at lower temperatures, while the growth rate dominates at higher temperatures.[39,45]

2.4.2 Synthesis of KNN thin films

Various deposition techniques have been used to produce KNN thin films, such as physical depositon, e.g. Pulsed Laser Deposition (PLD)[4,7] or radio-frequency magnetron sputtering (RF-MS),[4,46,47] as well as Chemical Solution Deposition (CSD).[4,10,15,16,48,49] PLD and RF-MS often uses $K_xNa_{1-x}NbO_3$ ceramics, made from K_2CO_3, Na_2CO_3 and Nb_2O_5, as targets. Some preparation conditions, electrical and mechanical properties from previous studies on KNN thin films made by CSD are given in Table 2.2.

Table 2.2: Ferroelectric and mechanical (piezoelectric constant d_{33}, film modulus (E_f) and hardness (H_f)) properties of KNN thin films manufactured by chemical solution deposition.

Substrate	**Solvent**	d_{33} **[pm/V]**	E_f**[GPa]**	H_f **[GPa]**	**ref**
$Pt/SiO_2/Si$	2-methoxyethanol	30.6-83.3	-	-	[50]
$Pt/SiO_2/Si$	2-methoxyethanol	40	-	-	[10]
$Pt/SiO_2/S$	2-methoxyethanol	46			[15]
Pt/Al_2O_3	Acetic acid	-	91	4.5	[51]
$Pt/SiO_2/Si$	Acetic acid	-	71	4.5	[51,52]

$K_xNa_{1-x}NbO_3$ made by CSD has traditionally been based on metal alkoxide precursor solutions with niobium(V)ethoxide as niobium source, and with 2-methoxyethanol as the solvent, mixed with either alkali ethoxides or acetates.[10,15,16,53] The main reason for using 2-metoxyethanol as solvent, is the sensitivity of alkoxides to moisture.[39] This sensitivity often requires use of chelating agents, such as acetylacetone, polyvinylpyrrolidone, polyehyleneglycol, diethanolamine, citric acid or EDTA, to stabilise the system.[50] Demanding synthesis conditions, toxicity and relatively high costs of the solvents, precursors and some of the chelating agents, makes aqueous alternatives preferable.

KNN thin films from a water based solutions containing ammonium oxalate oxoniobate ($NH_4NbO(C_2O_4)_2$) and alkali nitrates (KNO_3 and $NaNO_3$) have been reported by Pham[54] and Lorentzen[55]. The main challenges with this synthesis route are the formation of niobium-rich secondary phases during processing, and the easy formation of insoluble oxalate salts with metal ions such as alkaline earth metals, which is undesirable in a multi-metal precursor.[39] Camargo *et al.* have reported chemical syntheses of phase pure $NaNbO_3$[56] and $LiNbO_3$[57] powders by using a water-soluble niobium malic acid complex. Haugen[18] and Madaro[58] have reported alkali niobate powders synthesised by spray pyrolysis, using aqueous solution of a similar niobium precursor. Unlike oxalate, malic acid is not known for making insoluble salts, which makes it more versatile.

As mentioned, a major issue when processing KNN thin films is the loss of volatile alkali metals during heat treatment, promoting undesired alkali-deficient secondary phases.[4] Some of these secondary phases are known for being hygroscopic,[59,60] which may change the solubility properties of KNN if they are present. Excess amounts of Na and K in the precursor solution is a common way to compensate the alkali loss during heat treatment. Nakashima *et al.*,[15] Ahn *et al.*[10] and Kupec *et al.*[16] have reported phase pure KNN thin films by adding various amounts of alkali excess from

4 to 30 mol%. Although the alkali excess prevents the formation of secondary phases, the amount of excess has a large impact on the microstructure of the thin films. Nakashima *et al.*[15] observed an increase of both surface roughness and grain size with increasing amount of alkali excess in films with 0-10 mol% of K and Na, and both Ahn *et al.*[10] and Kupec *et al.*[16] observed similarly coarsened microstructure when adding 0-20 mol% and 0-10 mol% excess amounts of Na and K, respectively.

2.4.3 KNN thin films for biomedical applications

KNN is reported as biocompatible through cytotoxicity and degradation tests, although the hygroscopic nature of potassium (K) and sodium (Na) causes ion release from the KNN material in aqueous systems.[5,6] Ion release may induce structural distortion in the material and affect both piezoelectric and mechanical properties, which is adverse for implantable biomedical applications. One way to reduce the solubility is by substituting some of the A-site K and Na with less soluble metal ions. Metals such as lithium (Li), magnesium (Mg), calcium (Ca), strontium (Sr) and barium (Ba) have been introduced as A-sites dopants, in order to enhance the sinterability of bulk KNN.[6,13,61,62] Increased density of KNN by doping with Li have been reported by Yu *et al.*,[6] but release of Li ions during soaking increased the cytotoxicty. Alkaline earth (AE) dopants are less soluble and have similar ionic radii compared to K and Na, with the exception of the Mg^{2+}-ion that is noticeably smaller, as seen in Table 2.3.[63] The AE are regarded non-toxic[2], although Sr is a competing element to Ca inside the body, and can replace Ca as a mineral in the bone.[64] For a child, this may lead to bone growth problems.[64] Doping with AE introduces A-site vacansies into the perovskite lattice as shown in Equation 2.3:[4,13]

$$\mathrm{AEO} \xrightarrow{\mathrm{A_2O}} \mathrm{AE}_{\mathrm{A}}^{\bullet} + \mathrm{V}_{\mathrm{A}}' + \mathrm{O}_{\mathrm{O}}^{\times} \tag{2.3}$$

where AE represents the alkaline earth dopant, A is the A-site in the perovskite and V is a vacancy. Ahn *et al.*[65] have reported Ba-rich secondary phases in barium modified KNN after adding more than 1.5 mol% Ba, and Malic *et al.*[13] have reported Ba-rich secondary phases at even lower (0.5 mol%) amounts. Enhanced densification and piezoelectric coefficient d_{33} in KNN was also found by doping with 0.5 mol% Ca or Sr. It should be noted that both Sr and Mg are quite expensive (Figure 2.4), which is disadvantageous, leaving Ca as the most promising candidate as a A-site dopant in KNN.

Table 2.3: Ionic radii, charge and coordination number (CN) of sodium, potassium, niobium and selected alkaline earth cations.[63]

Element	**Symbol**	**Ionic charge**	**CN**	**Ionic radii [nm]**
Sodium	Na	+1	12	0.139
Potassium	K	+1	12	0.164
Magnesium	Mg	+2	6	0.072
Magnesium	Mg	+2	12	N/A
Calcium	Ca	+2	12	0.134
Strontium	Sr	+2	12	0.144
Barium	Ba	+2	12	0.161
Niobium	Nb	+5	6	0.064

2.5 Mechanical properties of thin films

The main challenge when determining the mechanical properties of thin films is the thickness of the film. Since the films are very thin, ranging from about 10 nm to a few microns, the use of conventional mechanical characterisation is limited. Indentation hardness tests are commonly used to determine the hardness of materials, and is a process where an indenter of known geometry is pressed into the surface of the material under a fixed load. The resulting area of the impression, or the depth of the penetration, can be used to determine the resistance of the material to damage. Indentation testing is fast, easy, and allows several measurements on one sample. Also, relatively inexpensive sample preparation makes it beneficial to use for mechanical measurements in the industry as well.

2.5.1 Nanoindentation

Nanoindentation is commonly performed by using an indenter with a triangular pyramid geometry (Berkovich indenter), but several indenter geometries are available.[66] In order to minimise the contribution of the indenter to the measurements, diamond is the most common used material for the indenter tip, due to its large elastic modulus and hardness.[66] During nanoindentation low loads are used, resulting in very small indentation depths and areas. In order to investigate the size of the area, time consuming instruments like atomic force microscopy, transmission- or scanning electron microscopy are required. Therefore, it has become important to extract the data from the loading-displacement curves. Instrumented indentation allows control of the penetration as a function of load where a loading-displacement curve is recorded during the indentation, and the hardness (H) and elastic modulus (E) can be extracted from the recorded curve according to the Oliver and Pharr's theory.[67–69] A typical load-displacement (P-h) curve is shown in Figure 2.8 (a) and Figure 2.8 (b) illustrates the schematic of the surface while in contact with an indenter and after unloading the tip.

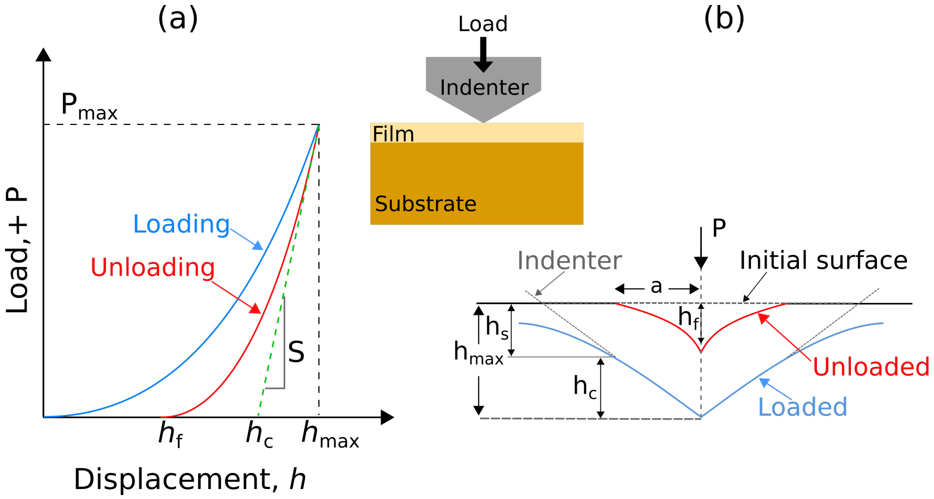

Figure 2.8: Illustration of (a) a typical load-displacement curve, and (b) an indenter penetrating a sample and the indentation pattern of an elastic-plastic material with parameters characterising the process, remade from Oliver and Pharr.[68] P_{max} and h_{max} is the maximum load and penetration, respectively, h_c is the contact depth, h_s is the sink-in of the material during indentation and h_f is the final displacement after unloading. The slope S is the unloading stiffness defined as $S\ \frac{dP}{dH}$

P is the load to the sample and h is the displacement relative to the initial surface. P_{max} and h_{max} is the maximum load and penetration, respectively. The contact depth (h_c) is calculated by the recovery displacement after indentation and h_f is the final displacement after unloading. When conducting nanoindentation it is assumed that both plastic and elastic deformation occurs during loading, and only elastic displacements are recovered during unloading.[67,68] The hardness of the material can be estimated from Equation 2.4:

$$H \quad \frac{P_{max}}{A} \tag{2.4}$$

where A is the contact area under loading, and is expressed as a function of the contact depth h_c. This area function is dependend on the indenter geometry and can be obtained by calibrations.[70] For an ideal Berkovich tip, $A = 24.5h_c^2$.[66]

The unloading stiffness is defined as $S \ \frac{dP}{dH}$, and is the slope of the upper part of the unloading curve. When measuring the elastic modulus it is assumed that the Young's modulus of elasticity (E) is constant and independent of indendation depth. The elastic modulus is measured from its relationship to unloading stiffness and contact area, given in Equation 2.5:[68]

$$S \quad \frac{dP}{dh} \quad \frac{2}{\sqrt{\pi}} E_r \sqrt{A} \tag{2.5}$$

where E_r is the effective elastic modulus, defined by the displacements occurring in the specimen with Young's modulus (E) and Poisson's ratio ν, and in the indenter with Young's modulus (E_i) and Poisson's ratio ν_i shown in Equation 2.6:[68]

$$\frac{1}{E_r} \quad \frac{1-\nu_i^2}{E_i} \quad \frac{1-\nu_s^2}{E_s} \tag{2.6}$$

The contact stiffness (S) can be calculated from the recorded load-displacement curve, while the contact area (A) of the indenter has to be determined on a standard fused quartz sample before the measurements.[70] Based on the equations above, the reduced, or effective elastic modulus (E_r) and hardness (H) can be calculated.

2.5.2 Mechanical properties of KNN thin films

Most reports on KNN thin films are focused on optimising the electrical properties,[2,4,7,9,10,15,16,49] while reports on mechanical properties are more or less absent. The few reports on mechanical properties of KNN show that the hardness and elastic modulus are strongly dependent on surface morphology, substrates, average grain size and deposition temperature.[14,47,51,52] Mahesh and Pamu[14] reported hardness values varying from 1.0-9.4 GPa, and elastic modulus varying from 26.7-100.2 GPa in KNN thin films prepared by RF-MS. Kugler *et al.*[47] have reported the highest values of hardness (12 GPa) and elastic modulus (207 GPa) on KNN thin films, also made by RF-MS.

Chapter 3

Experimental

The development of the synthesis route was performed in several laboratories at NTNU. The precursor solutions were synthesised in a wet-chemical laboratory, and the thin film deposition was performed in a coating laboratory, both at the Department of Materials Science and Engineering (IMA). Substrsates used for the deposition were oxygen plasma cleaned in an ISO 7 class cleanroom at NTNU NanoLab prior to film deposition. Characterisation of mechanical properties was performed at NTNU Nanomechanical Lab, by Professor Jianying He. The sputtering of platinum electrodes on the film surface where conducted by Ph.D. candicate Nikolai Helth Gaukås. The precursor solutions and thin film preparation are based on previous work of Madaro,[58] Pham[54], Lorentzen[55] and the author.[17] Figure 3.1 illustrates the synthesis route for deposition, the soaking process and the nanomechanical characterisation of the thin films.

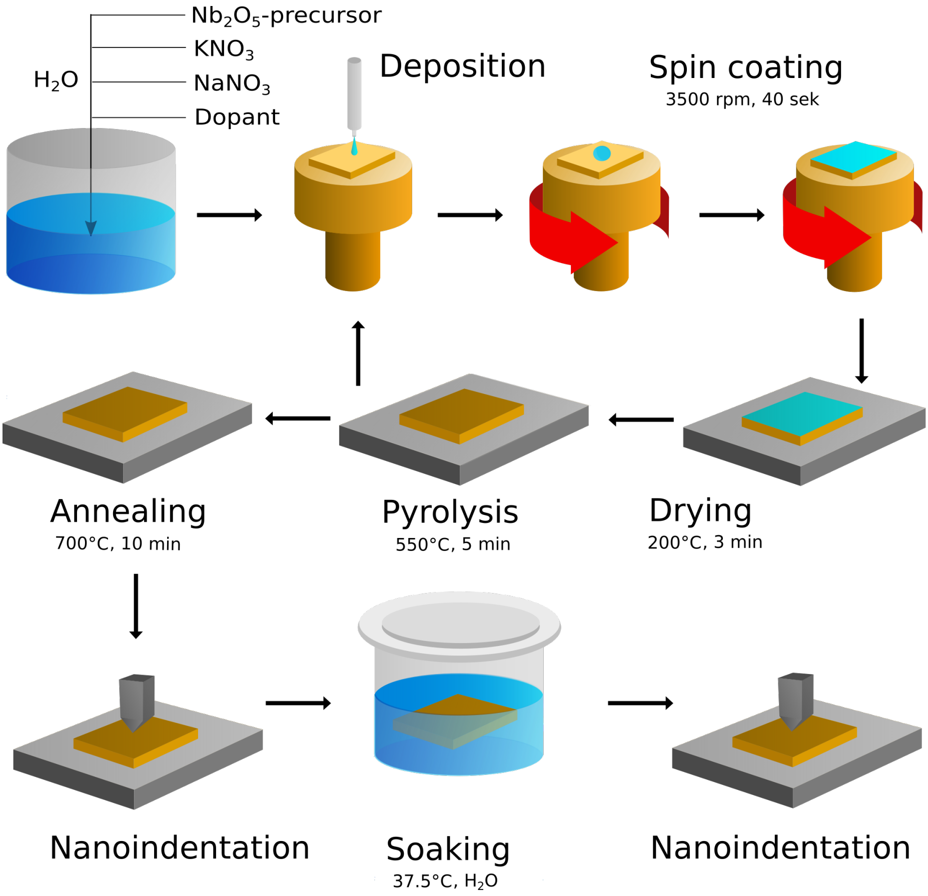

Figure 3.1: An overall illustration of the synthesis route. First, precursors are dissolved in water, then deposited on cleaned (100)-oriented $SrTiO_3$-substrates before being spin-coated, and dried on a hot plate with subsequently pyrolysis on a rapid heating plate (RHP). Deposition, spin-coating, drying and pyrolysis are repeated until sufficient thickness is achieved, before the film is finally annealed. Then the films are characterised by XRD. Nanoindentation is performed before and after soaking in water-solution for different time durations.

3.1 Solution preparation

Table 3.1 present all the chemicals used in the experimental work in this thesis.

Table 3.1: List of all the chemicals used to prepare solutions in this work.

Chemical	Molecular formula	Purity [%]	Manufacturer
Potassium nitrate	KNO_3	99	Alfa Aesar
Sodium nitrate	$NaNO_3$	99	Sigma-Aldrich
Calcium nitrate tetrahydrate	$Ca(NO_3)_2 \cdot 4H_2O$	99	Sigma-Aldrich
Ammonium niobate (V) oxalate hydrate	$C_4H_4NNbO_9 \cdot nH_2O$	99.99	Sigma-Aldrich
Malic acid (MA)	$C_4H_6O_5$	99	Sigma-Aldrich
Ethylenediaminetetraacetic acid (EDTA)	$C_{10}H_{16}N_2O_8$	99	Sigma-Aldrich
Ammonium hydroxide (25 % in H_2O)	NH_4OH		VWR Chemicals

3.1.1 Niobium precursor solution

A niobate malic acid complex was prepared according to the procedure given by Madaro.[58] A flow chart showing the synthesis route is given in Figure 3.2. $NH_4NbO(C_2O_4)_2 \cdot nH_2O$ (NAmOx, ~0.12 mol) was dissolved in preheated (100 °C) distilled water (600 mL), and stirred at 70 °C for 3 h until all the NAmOx was dissolved. Ammonia (NH_4OH, 25 %) was added to adjust the solution to pH = 11, precipitating niobic acid ($Nb_2O_5 \cdot nH_2O$), and then stirred at 70 °C for 2 h before aged at room temperature for 12 h. The oxalate containing fluid was decanted, and the niobic acid was washed and centrifuged (10 000 rpm, 5 min) three times with NH_4OH (1 %) to remove remaining oxalate ions. DL-malic acid (MA) was used as complexing agent. The precipitated niobic acid was dissolved in a MA solution (0.33 M) with a molar ratio of [Nb]:[MA] = 1:2, followed by stirring at 70 °C for 2 h before filtered and stabilised at pH = 7

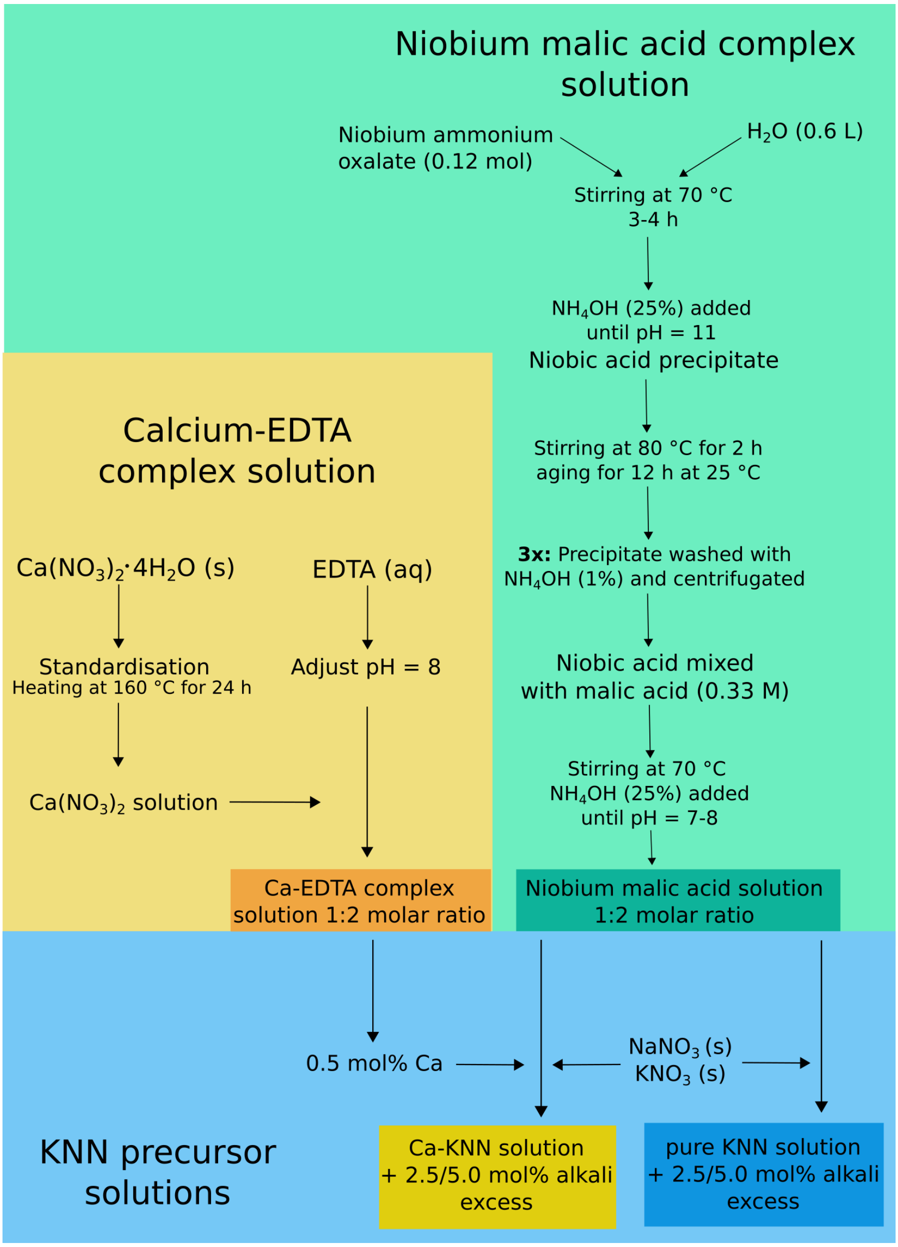

Figure 3.2: Flow chart showing the preparation procedure of niobium and calcium precursor solutions, and the preparation procedure of Ca-KNN and pure KNN precursor solutions.[58].

by adding NH_4OH (25 %). The molal concentration of niobium was calculated to $0.0994(0)\,\mathrm{mmol\,g^{-1}}$solution by thermogravimetric standardisation of the niobium precursor solution, based on the weight of Nb_2O_5, after calcination at 1100 °C. The temperature program used for standardisation is given in Figure 3.3, and detailed description of the thermogravimetric standardisation procedure is included in Appendix A.1

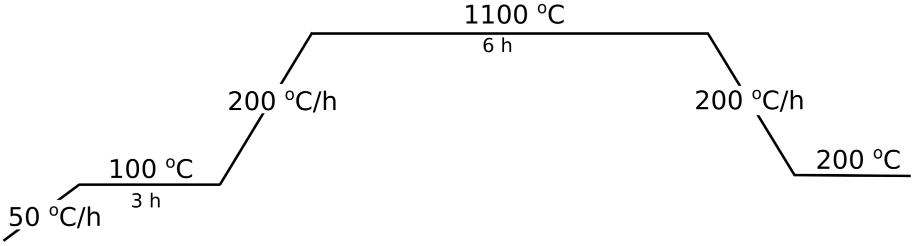

Figure 3.3: Temperature program used for the standarisation of the niobium precursor solution.

3.1.2 Calcium precursor solution

$Ca(NO_3)_2$ (s) was standardised by heating solid $Ca(NO_3)_2 \cdot 4\,H_2O$ (s) at 160 °C for 24 h before weighted. Ethylenediaminetetraacetic acid (EDTA) was used as complexing agent, and the dried $Ca(NO_3)_2$ (s) was added to a water solution with an additional amount of EDTA giving the ratio [Ca]:[EDTA] = 1:2. The solution was stabilised at pH = 8, by using NH_4OH (25 %), after the $Ca(NO_3)_2$ (s) was dissolved. The concentration of Ca^{2+} in the solution was calculated to (0.0323 M).

3.1.3 $K_{0.5}Na_{0.5}NbO_3$

Three pure KNN precursor solutions were made with different amounts of alkali excess, given in Table 3.2. Predried (140 °C, 12 h) KNO_3 (s) and $NaNO_3$ (s) were added into the niobium malic acid precursor solution, giving a concentration of 0.1 M. The solutions were stirred at 50 °C until all KNO_3 (s) and $NaNO_3$ (s) were dissolved.

Table 3.2: Abbreviations and synthesis parameters for the preparation of pure KNN precursor solutions. All solutions were made with predried (140 °C, 12 h) KNO_3 (s) and $NaNO_3$ (s) as alkali precursors and a niobium malic acid complex solution as niobium precursor.

Composition	**Concentration** [M]	**Excess alkali** [%]	**Abbreviation**
$K_{0.5}Na_{0.5}NbO_3$	0.1	0.0	KNN00
$K_{0.5}Na_{0.5}NbO_3$	0.1	2.5	KNN25
$K_{0.5}Na_{0.5}NbO_3$	0.1	5.0	KNN50

3.1.4 $K_{0.495}Na_{0.495}Ca_{0.005}NbO_3$

Two calcium modified KNN precursor solutions (Ca-KNN) were made with different amounts of alkali excess, given in Table 3.3. Predried (140 °C, 12 h) KNO_3 (s) and $NaNO_3$ (s), and complexed Ca-EDTA solution (0.5 mol% Ca^{2+}) were added into the niobium malic acid precursor solution, giving a concentration of 0.1 M. The solutions were stirred at 50 °C until all KNO_3 (s) and $NaNO_3$ (s) were dissolved.

Table 3.3: Abbreviations and synthesis parameters for the preparation of calcium modified Ca-KNN precursor solutions. All solutions were made with predried (140 °C, 12 h) KNO_3 and $NaNO_3$ as alkali precursors, $CaNO_3$-EDTA solution as calcium precursor and a niobium malic acid complex solution as niobium precursor.

Composition	**Concentration** [M]	**Excess alkali** [%]	**Abbreviation**
$K_{0.495}Na_{0.495}Ca_{0.005}NbO_3$	0.1	2.5	Ca05KNN25
$K_{0.495}Na_{0.495}Ca_{0.005}NbO_3$	0.1	5.0	Ca05KNN50

3.2 Thin film preparation

The precursor solutions were deposited on either (100)-oriented $SrTiO_3$ (STO) or noibium modified (100)-oriented Nb:STO substrates. All substrates were cleaned with oxygen plasma before deposition in order to activate the substrate surface and enhance the wetting properties. Characteristics of the substrates, which characterisation methods they were used for and which precursor solutions that were deposited onto the substrates are given in Table 3.4.

Table 3.4: List of substrate properties, characterisation method and the precursors used

Substrate	Orientation	Size [mm^3]	Manufacturer	Solutions	Characterisation
$SrTiO_3$ (STO)	(100)	10x10x0.5	CRYSTAL GmbH	KNN25	Mechanical
				KNN50	Mechanical
				Ca05KNN25	Mechanical
				Ca05KNN50	Mechanical
Nb:$SrTiO_3$ (Nb:STO)	(100)	10x10x0.5	CRYSTAL GmbH	KNN50	Ferroelectric
				Ca05KNN50	Ferroelectric

3.2.1 Solution deposition

KNN- and Ca-KNN precursor solutions, containing 2.5 or 5.0 mol% alkali excess, were spin coated onto Nb:STO- or STO-substrates at 3500 rpm for 40 s, using a spin coater (WS-400B-6NPP-LITE/AS, Laurell Technologies). The wet films were dried at 200 °C for 3 min on a hotplate. Dried films were placed on a silicon wafer with a quartz glass on top before pyrolysed at 550 °C in air for 5 min, using a heating rate of 100 °C min^{-1}, on a homemade setup (Rapid Heating Plate, RHP). An illustration of the setup is shown in Figure 3.4. The deposition was repeated 15 times until a desired thickness of about

180 nm was achieved. The thin films were then annealed at 700 °C for 10 min in air, using a heating rate of 100 °C min^{-1}, on the RHP.

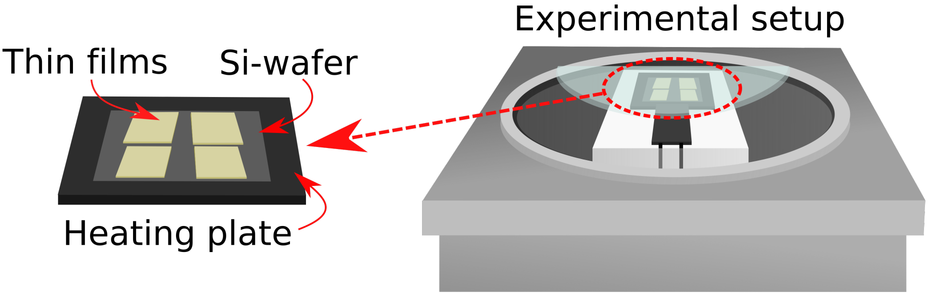

Figure 3.4: Illustration of the Rapid Heating Plate (RHP) used for thermal treatment during the synthesis of the thin films.

3.3 Characterisation

This section is divided into two parts: Characterisation of powders from dried KNN- and Ca-KNN precursor solutions and characterisation of the KNN- and Ca-KNN thin films.

3.3.1 Powder characterisation

The KNN and Ca-KNN precursor solutions were dried to gels at 160 °C for 12 h before grounded into fine powders. Grounded powder were calcined at different temperatures using the heating program as illustrated in Figure 3.5. All calcination temperatures are included in Appendix A.2.

Thermal gravimetric analysis (TGA)

Thermal gravimetric analysis (TGA, STA 449C, Netzsch, Selb, Germany) and mass spectroscopy (MS, QMS 403C, Netzsch, Selb, Germany) were used to measure and analyse the mass loss of pre-dried gels from the KNN and Ca-KNN precursor solutions. The heat treat-

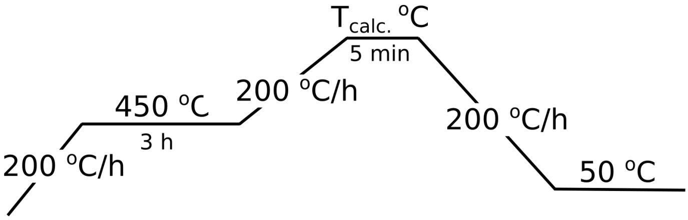

Figure 3.5: Heating program used when calcining the KNN- and Ca-KNN precursor solutions.

ment was conducted in synthetic air from 40 °C to 900 °C using a heating rate of 10 °C min^{-1}.

X-ray diffraction (XRD)

Cu Kα radiation was used to investigate the phase purity of KNN and Ca-KNN powders in Bragg-Brentano geometry (D8 Advance DaVinci X-ray Diffractometer, Bruker, Germany). θ-2θ scans were recorded in the 2θ range of 10-75 ° with a variable divergence slit of 6 mm, step size of 0.013° and a scan time of 1 s per step. All diffractograms were searched and matched with scans from the PDF-4+ database (International Centre for Diffraction Data) using Bruker AXS DIFFRACT.EVA (Version 5) software. Scans run on KNN and Ca-KNN powders calcined at 800 °C were used for Pawley refinements, using Bruker AXS Topas version 5 software, in order to calculate the lattice parameters. Instrument and correction settings for the software is given in Table 3.5.

Table 3.5: Instrument and correction settings, and the input lattice parameters from Tellier *et al.*,[37] used for Pawley refinement on the XRD scans.

Parameters	**Value**
Primary and Secondary radii	280 mm
Linear PSD angle rate	3°
Variable Divergence Slits irradiated length	6 mm
Source and Receiving slit length	12 mm
Sample length	15 mm
Primary and Secondary soller	2.5°
N Beta	30
Lorentz-Polarisation factor	0
Input values for the lattice parameters	
a lattice parameter (Pm)	4.0046 Å
b lattice parameter (Pm)	3.9446 Å
c lattice parameter (Pm)	4.0020 Å
Beta angle (Pm)	90.3327°

3.3.2 Thin film characterisation

The KNN and Ca-KNN thin films were soaked in distilled water (10 mL) and kept in an furnace holding 37 °C for different periods of time, in order to obtain an idea of how the structural and mechanical properties will be affected inside the human body. The different soaking periods are given in Table 3.6. The pH of the water solutions were measured prior to, and after the soaking by using a pH meter (S20 SevenEasy™, Mettler Toledo). The pH meter was calibrated by using two different buffer solution with pH 7.00 and pH 4.01.

Grazing incidence X-ray diffraction (GI-XRD)

Thin film samples were prepared by mounting the films in a sample holder with modelling clay. Phase purity of the thin films was

Table 3.6: List of soaking time and which precursor solution for different KNN and Ca-KNN thin films.

Precursor Solution	Soaking time [days]
KNN25	0
KNN25	1
KNN25	3
KNN25	6
KNN25	10
KNN25	14
Ca05KNN25	0
Ca05KNN25	1
Ca05KNN25	3
Ca05KNN25	6
Ca05KNN25	10
Ca05KNN25	14
KNN50	0
KNN50	2
KNN50	6
KNN50	14
Ca05KNN50	0
Ca05KNN50	2
Ca05KNN50	6
Ca05KNN50	14

investigated prior to and after the soaking by performing GI-XRD, using an X-ray diffractometer (D8 A25 Advance DaVinci, Bruker, Germany) with Cu Kα radiation. The incidence angle was set at 2°, with step size of 0.030° and total scan time of 2 h.

Nanoindentation

Mechanical properties of the thin films were investigated by using a nanoindentation testing system (Hysitron Triboindenter 950, Bruker, Germany) with a Berkovitch diamond indenter tip. Preparation of the samples before measurements was done by gluing the films to magnetic substrates (Atomic Force Microscopy (AFM) stainless steel discs) as seen in Figure 3.6. The first samples, KNN25 and Ca05KNN25 thin films, were attached by using epoxy, while the second run, KNN50 and Ca05KNN50 thin films, were attached by using super glue (Loctite ethyl-2-cyanoacrylate, Henkel). The super glue was used to avoid air bubbles between the sample and the magnetic substrate, caused by the long drying time of the epoxy. 6-9 effective indents were made on each sample and the maximum load was set to 300 µN. A loading-displacement curve was recorded for each indent, and the reduced modulus and hardness were extracted from these curves, based on the equations (Equation 2.4-2.6) in the Introduction part 2.5.1, in the Hysterion Triboindenter 950 Analysis Software. Average reduced modulus, hardness and standard deviations were calculated based on all the indents on each sample. All measurements and calculations were conducted by Jianying He at the NTNU Nanomechanical lab.

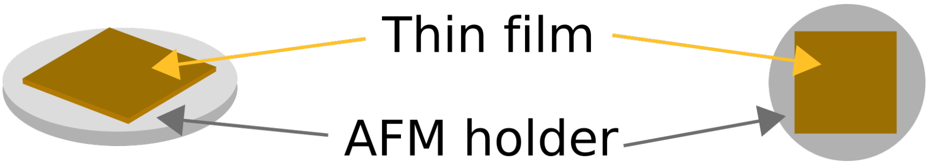

Figure 3.6: Illustration of the preparation of the thin films before nanoindentation.

Ferroelectric measurements

Platinum (Pt) electrodes were sputtered on the surface of Ca05KNN50 and KNN50 thin films deposited on Nb:STO substrates by using a sputtering machine (Custom ATC-2200V, AJA International Inc.). Surface Pt-electrodes acted as top electrode, while the Nb:STO substrate was the bottom electrode for the ferroelectric measurements. An electrode mask with small electrode area = 0.7859 mm^2 and big electrode area = 4.9087 mm^2 was used to get the Pt-electrode configuration as seen in Figure 3.7 (c). The electrode mask was attached onto the surface of the film before the sputtering. Ferroelectric hysteresis loops were obtained by using a TF Analyzer 2000 (AixACCT Systems GmbH, Germany) in FE module (Ferroelectric standard testing) and a aixACCT 200V (AixACCT Systems GmbH, Germany) as high voltage amplifier. The films were placed on aluminium foil, and one of the probes was placed on a Pt-electrode on the film surface (top electrode), while the other was placed on the aluminium foil as illustrated in Figure 3.7 (a). An illustration of the ferroelectric setup is given in Figure 3.7 (b).

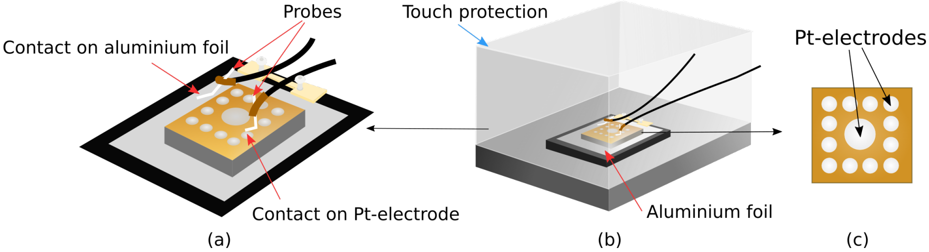

Figure 3.7: Illustration of the set up used for ferroelectric measurements. (a) Close up illustration of how the probes where placed in order to measure the ferroelectric properties, (b) the set-up and (c) the platinum (Pt) electrode configuration on the film surface.

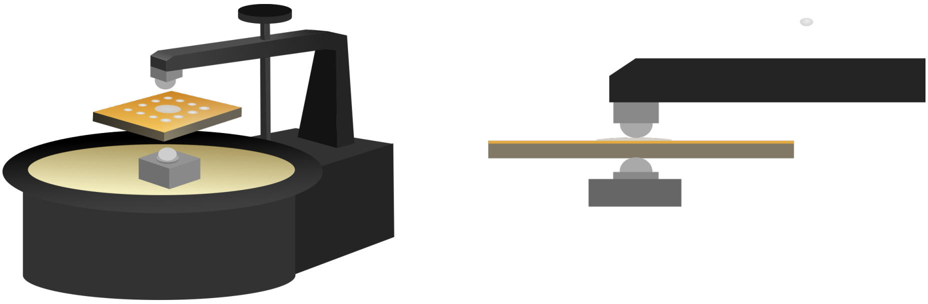

Figure 3.8: (a) Illustration of the set up used for d_{33} measurements and (b) close up illustration of the clamping of the sample between the top and bottom probes.

Piezoelectric measurements

The piezoelectric coefficient (d_{33}) was measured by a Berlincourt piezo d_{33} meter (YE2730A Piezoelectric Constant (d33) Calibrator, APC International, Ltd., USA). The large Pt-electrode on each of the thin films were clamped between the top and bottom probes as seen in Figure 3.8.

Chapter 4

Results

This chapter is divided into two parts; analysis of the precursor solutions, and the characterisations of the produced thin films.

4.1 Precursor properties

4.1.1 Stochiometry of the precursor solutions

As seen in Figure 4.1, pure KNN and Ca-KNN were formed above 550 °C for the KNN and Ca-KNN precursor solutions with 2.5 and 5.0 mol% alkali excess. The peak observed at 27.3° in the calcined Ca05KNN25 powder at 550 °C is believed to belong to noise during the measurements. A niobium rich secondary phase ($K_4Nb_6O_{17}$) was formed in the stochiometric KNN00 powder calcined at 550 °C (marked with ▼ in Figure 4.1). All precursor solutions formed pure KNN or Ca-KNN above 550 °C, additional X-ray diffractograms are included in Appendix B. All diffractograms were matched against the PDF card 00-061-0315 for KNN in the software DIFFRACT.EVA.

Some important key observations can be made when comparing the peaks in the diffractograms. First, the niobium rich secondary phase ($K_4Nb_6O_{17}$) present in KNN00, which disappears at calcination temperatures higher than 550 °C, should be noticed. Previous work on development of KNN thin films from aqueous solutions, done by Pham[54] and Lorentzen[55], have shared the same observation in

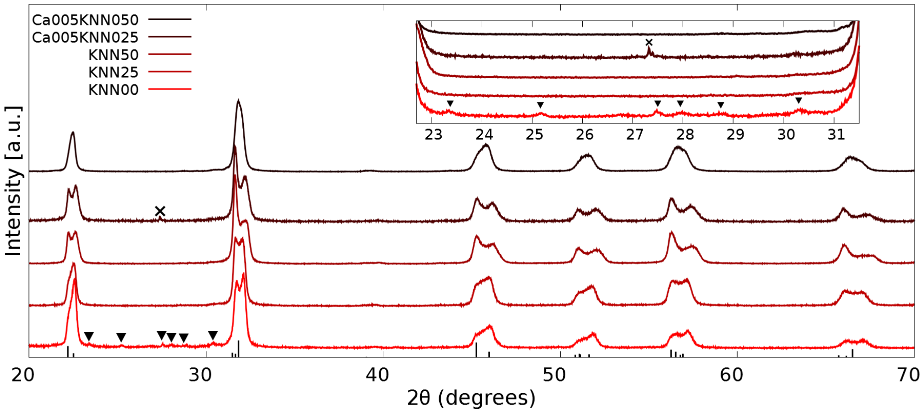

Figure 4.1: X-ray diffractogram of powders from the precursor solutions calcined at 550 °C for 5 min. × is assigned to unknown phase in Ca05KNN25. ▼ (KNN00) reflections are assigned to $K_4Nb_6O_{17}$. Diffraction lines of $K_{0.5}Na_{0.5}NbO_3$ are included as references at the bottom (black, PDF card 00-061-0315)

precursor solutions based on a niobium oxalate complex, instead of the niobium malic acid complex. Another distinction between the diffractograms is the shape of the peaks. The KNN powders show more narrow, sharp peaks, while the Ca-KNN powders show less sharp and more rounded peaks, suggesting higher degree of nanocrystallinity in Ca-KNN.

4.1.2 Crystal structure of calcined powders

Pawley refinements were conducted on the diffractograms obtained from dried powders of the precursor solutions calcined at 800 °C for 5 min. Table 4.1 shows the refined lattice parameters, angles and R_{wp} obtained within the space group *Pm*. The refined parameters are compared to those obtained by Tellier *et al.*[37] (a = 4.0046 Å, b = 3.94464 Å, c = 4.00200 Å and β = 90.3327). The Ca-doped KNN is characterised by a slightly increase in the unit cell angle β and a

Table 4.1: Lattice parameters, unit cell volume, angle (β) and the weighted profile R-factors (R_{wp}) from the Pawley refinement of the diffractograms of calcined dried powders from the precursor solutions.

Compund	***a*** **[Å]**	***b*** **[Å]**	***c*** **[Å]**	β [°]	**Volume [Å^3]**	$\mathbf{R_{wp}}$
Ca05KNN25	3.9992(2)	3.9352(2)	3.9783(3)	90.31(1)	62.60(7)	9.52
Ca05KNN50	3.9969(1)	3.9538(5)	3.9874(2)	90.31(5)	63.01(2)	7.33
KNN25	3.9992(8)	3.9459(3)	3.9840(6)	90.259(6)	62.869(4)	9.27
KNN50	4.0179(5)	3.9564(1)	3.99747(1)	90.257(8)	63.372(9)	9.13

slightly decrease in the unit cell volume. Figure 4.2 shows the Pawley refinements (within space group *Pm*) of the diffractorgram for the KNN50 sample. The difference between the refined and measured data is included to indicate how well the refinements fit. Pawley refinements of KNN25, Ca05KNN25 and Ca05KNN50 are given in Appendix C.

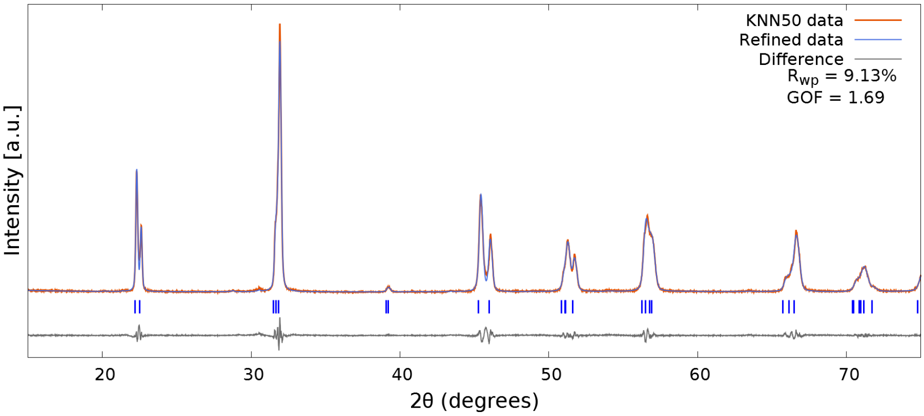

Figure 4.2: Pawley refinement of KNN50 powders calcined at 800 °C, within the *Pm* space group. The grey line at the bottom represents the difference between the measured and refined data. The blue lines are the indexed peak positions for $K_{0.5}Na_{0.5}NbO_3$ from PDF card 00-061-0315.

4.1.3 Termogravimetric analysis

The mass losses upon heating to 900 °C of dried powders from KNN00, KNN25, KNN50, Ca05KNN25 and Ca05KNN50 precursor solutions are presented in Figure 4.3. The total weight loss was about 70 % for each of the samples, and all precursors show the same decomposition characteristics upon heating. The large weight losses (about 50 %) between 500 °C and 560 °C are related to the combustion of organic species and is accompanied by crystallisation of the perovskite KNN phase. No further mass loss was observed after reaching 570 °C. These observations were used to select the pyrolysis temperature (550 °C) for the thin film preparation.

4.2 Thin film properties

4.2.1 Phase purity and solubility measurements

pH measurements were conducted in order to investigate the solubility of KNN in the water solutions. The pH development in the water solutions after soaking the KNN25 and Ca05KNN25 thin films for different periods of time is given in Figure 4.4. No reliable measurements were obtained of the water solutions after soaking the KNN50 and Ca05KNN50 thin films due to instrument failure, which caused no saturated pH during the calibration procedure before the measurements. The measurements plotted in Figure 4.4 show a slight decrease in pH during the first days of soaking before the pH somehow raises and stabilises around pH = 7.0-7.2.

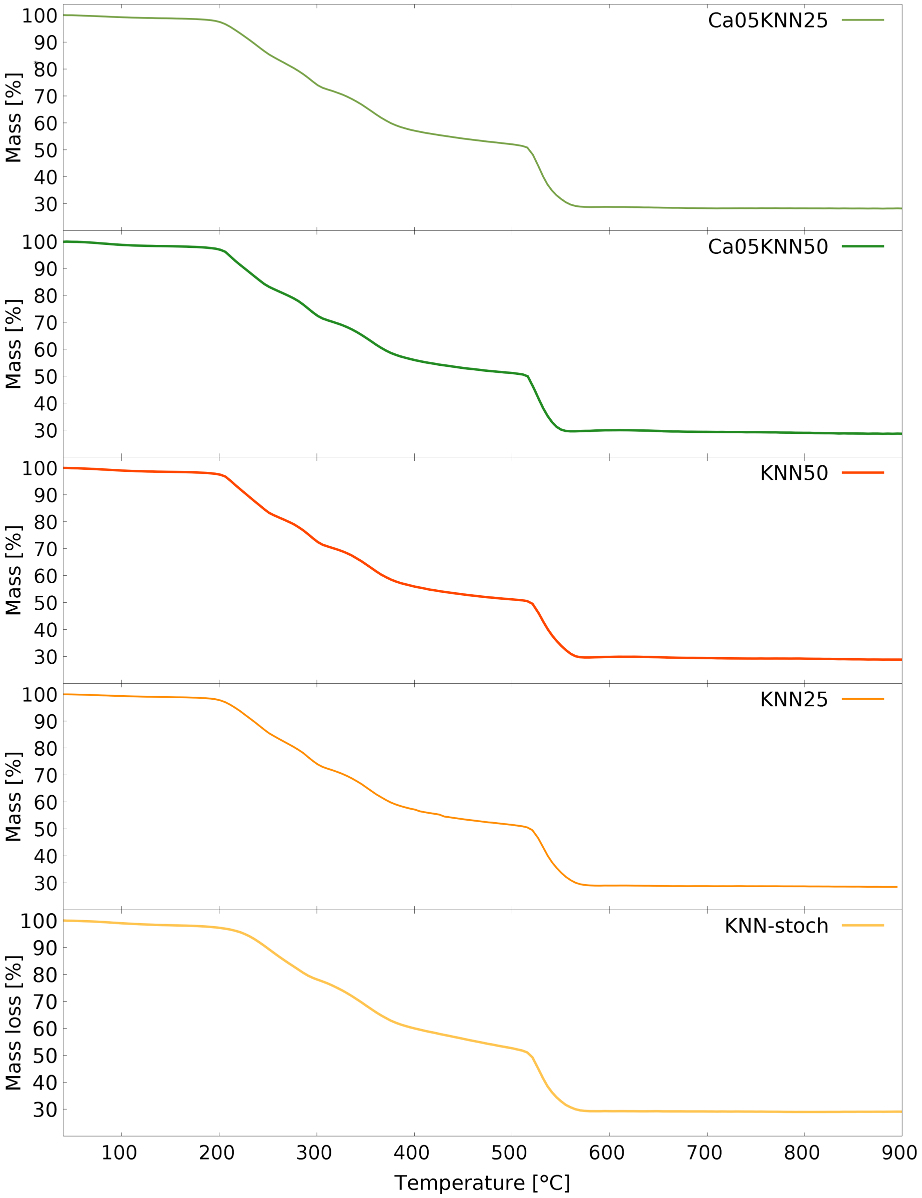

Figure 4.3: Thermogravimetric analysis of the dried powders from the Ca-KNN and KNN precursor solutions, showing the mass losses upon heating to 900 °C.

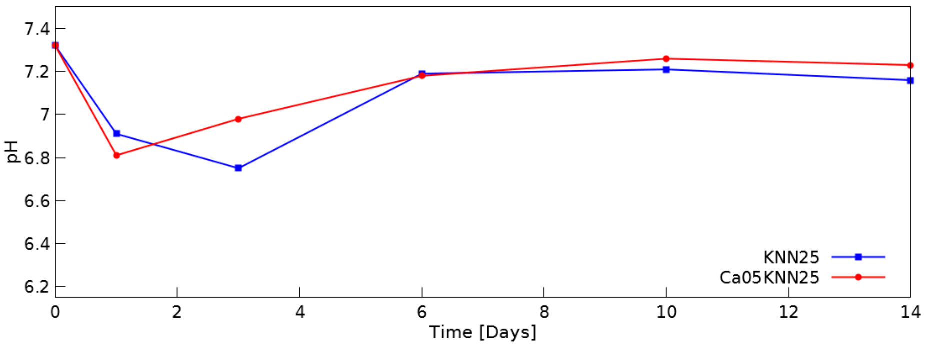

Figure 4.4: Development of the pH after soaking the KNN25 and Ca05KNN25 films for different periods of time.

GI-XRD-patterns of the KNN and Ca-KNN thin films, with 2.5 and 5.0 mol% alkali excess, deposited on $SrTiO_3$ substrates and annealed at 700 °C are presented in Figure 4.5. Phase pure thin films were obtained from the KNN50 and Ca05KNN50 precursor solutions (5.0 mol% alkali excess), while the thin films produced from KNN25

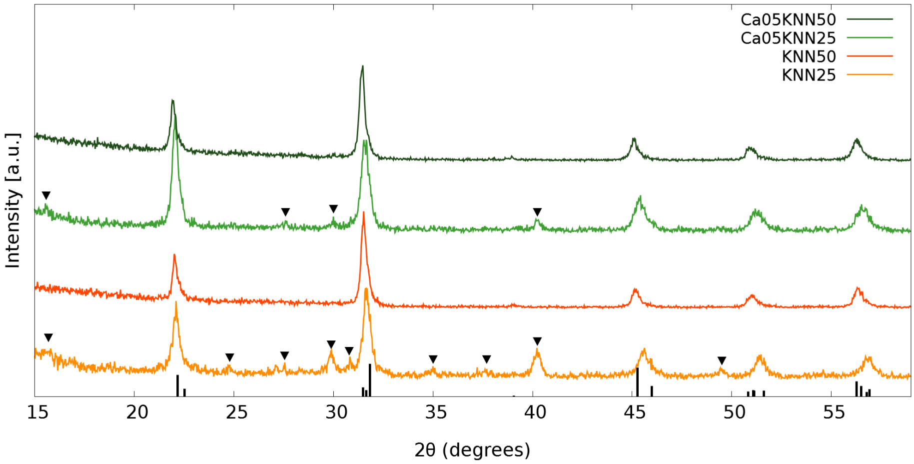

Figure 4.5: GI-XRD patterns of annealed KNN and Ca-KNN thin films on (100)-STO substrates. ▼ reflections are assigned to the niobium rich secondary phase, $K_4Nb_6O_{17}$. Diffraction lines of $K_{0.5}Na_{0.5}NbO_3$ are included as references at the bottom (black, PDF card 00-061-0315)

and Ca05KNN25 precursor solutions (2.5 mol% alkali excess) showed presence of a niobium rich secondary phase ($K_4Nb_6O_{17}$, PDF card 04-009-6408) after annealing.

Figure 4.6 and Figure 4.7 show the GI-XRD patterns of KNN25 and Ca05KNN25 after being soaked for various time lengths. The broad shaped peaks from 15-25° are believed to belong to spilled epoxy on the surface of the thin films when they were mounted onto the AFM-holders before nanomechanical testing. As seen from the Figures, the niobium rich secondary phase $K_4Nb_6O_{17}$ disappeared during the soaking. These observations are in agreement with $K_4Nb_6O_{17}$ being known to be highly hygroscopic,[59,60] and the secondary phase is believed to dissolve in the water solution. As seen in Figure 4.8 and Figure 4.9, no change in phase purity was observed for the KNN50 and Ca05KNN50 thin films after soaking.

4.2.2 Surface morphology and film thickness

The SEM cross-section of 153 ± 4 nm thick KNN50 thin films, and 168 ± 6 nm thick Ca05KNN50 thin films deposited on $SrTiO_3$ substrates and annealed at 700 °C are shown in Figure 4.10 and Figure 4.11, respectively. The images show homogeneous thickness and that the films grow in a columnar structure.

The microstructures of non-soaked KNN25, Ca05KNN25, KNN50 and Ca05KNN50 thin films are presented in Figure 4.12. The KNN50 and Ca05KNN50 thin films (Figure 4.12 (c) and (d)) displayed a uniform grain structure consisting of small, spherical-like grains. The SEM images of KNN25 and Ca05KNN25 thin films (Figure 4.12 (a) and (b)) show an inhomogenous microstructure consisting of small

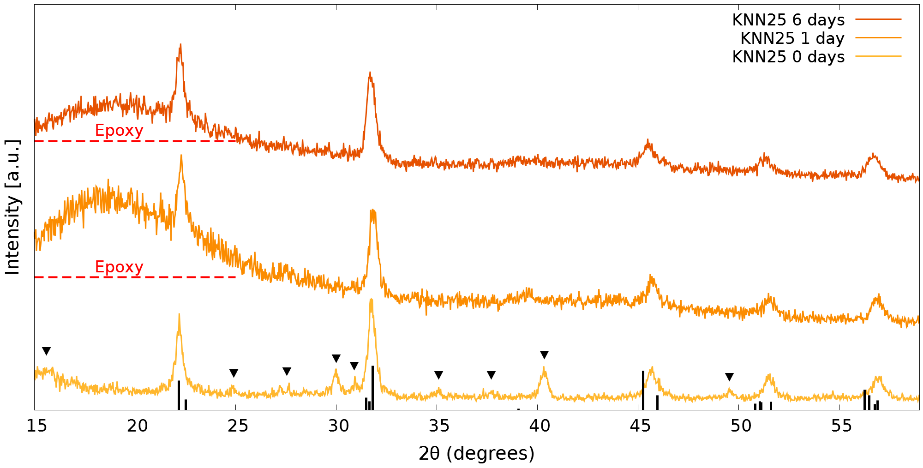

Figure 4.6: GI-XRD patterns of KNN25 thin films on (100)-STO substrates before and after soaking in distilled water. ▼ reflections are assigned to the niobium rich secondary phase, $K_4Nb_6O_{17}$. Diffraction lines of $K_{0.5}Na_{0.5}NbO_3$ are included as references at the bottom (black, PDF card 00-061-0315)

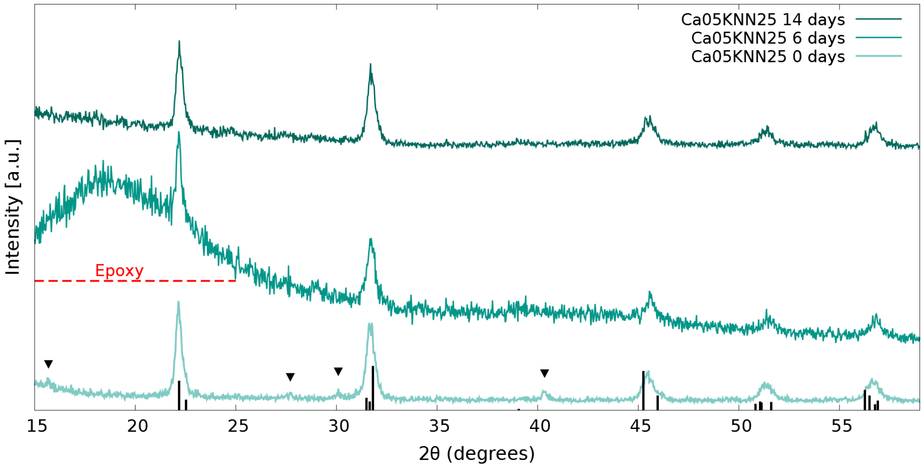

Figure 4.7: GI-XRD patterns of annealed KNN and Ca-KNN thin films on (100)-STO substrates before soaking in distilled water.▼ reflections are assigned to the niobium rich secondary phase, $K_4Nb_6O_{17}$. Diffraction lines of $K_{0.5}Na_{0.5}NbO_3$ are included as references at the bottom (black, PDF card 00-061-0315)

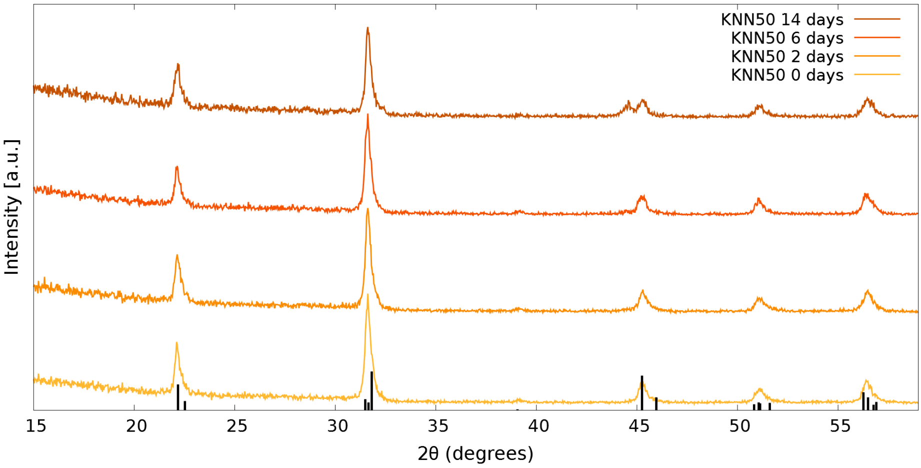

Figure 4.8: GI-XRD patterns of KNN50 thin films on (100)-STO substrates before and after soaking in distilled water for different periods of time. Diffraction lines of $K_{0.5}Na_{0.5}NbO_3$ are included as references at the bottom (black, PDF card 00-061-0315)

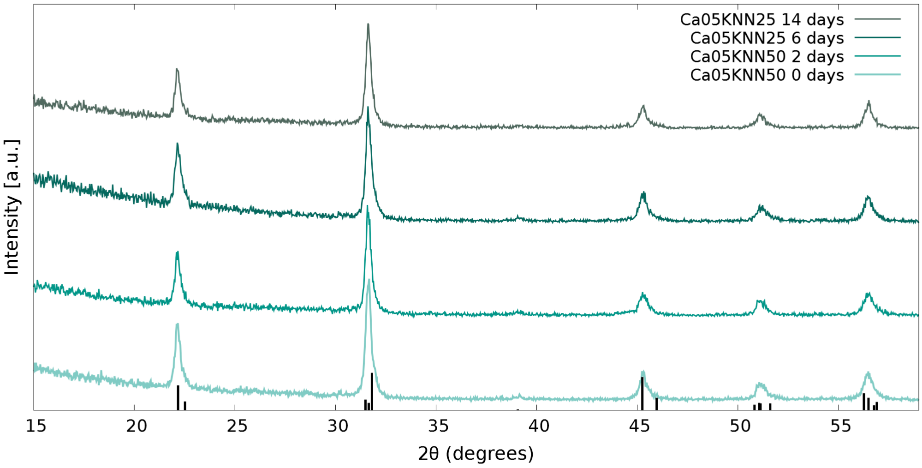

Figure 4.9: GI-XRD patterns of Ca05KNN50 thin films on (100)-STO substrates before and after soaking in distilled water for different periods of time. Diffraction lines of $K_{0.5}Na_{0.5}NbO_3$ are included as references at the bottom (black, PDF card 00-061-0315)

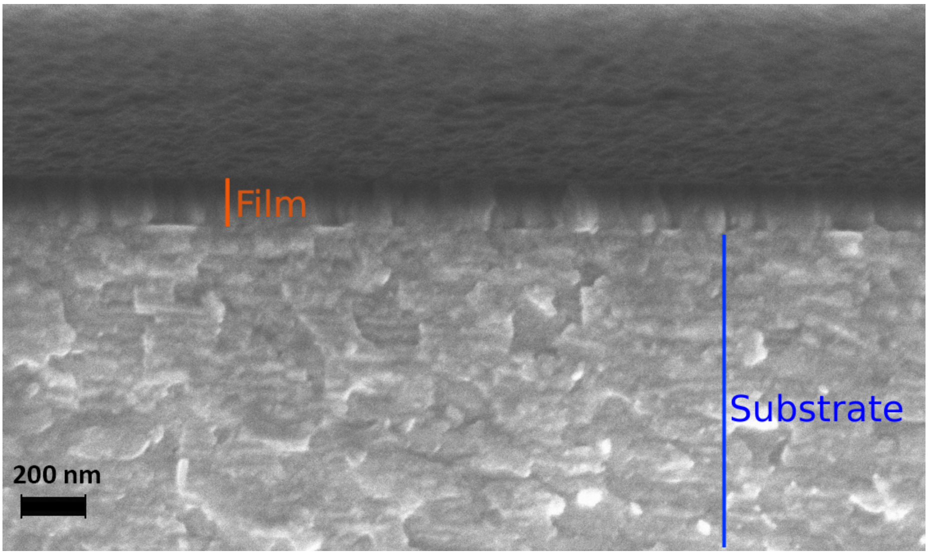

Figure 4.10: SEM pictures showing the cross-section of selected KNN50 thin film before soaking. The thin film grows in a columnar structure and the thickness is about 153 nm.

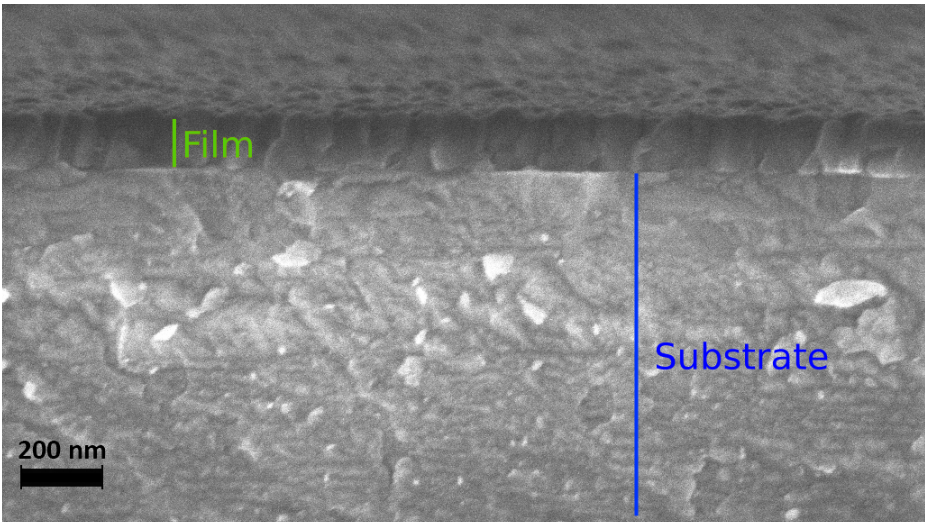

Figure 4.11: SEM pictures showing the cross-section of selected Ca05KNN50 thin film before soaking. The thin film grows in a columnar structure and the thickness is about 168 nm.

spherical-like grains where the grain boundaries are almost featureless, and larger spherical and squared grains. The average grain size of the KNN25 and Ca05KNN25 thin films were estimated to 102 ± 10 and 128 ± 10 nm, respectively, which is a bit larger compared to the KNN50 and Ca05KNN50 thin films with estimated average grain size = 86 ± 8 nm and 82 ± 8 nm, respectively.

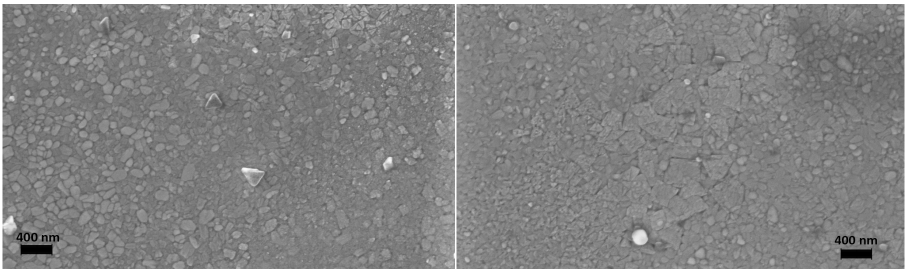

(a) KNN25 **(b)** Ca05KNN25

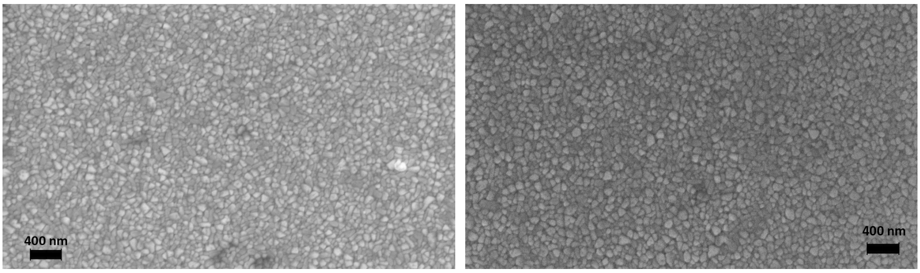

(c) KNN50 **(d)** Ca05KNN50

Figure 4.12: SEM images of KNN and Ca-KNN with 2.5 mol% alkali excess (a) and (b), and KNN and Ca-KNN with 5.0 mol% alkali excess (c) and (d).

No change in film thickness was observed after soaking the films for various time lengths. However, a change in the surface morphology was observed in the KNN25 and Ca05KNN25 thin films. Figure 4.13 (a)-(f) show the change in surface morphology of Ca05KNN25 during soaking in distilled water at 37 °C. The dark areas evolving during the soaking were first believed to belong to $K_4Nb_6O_{17}$ dissolving, but as seen from the SEM cross section image in Figure 4.14, and the SEM surface images in Figure 4.15 and Figure 4.16 the dark areas were revealed to be something growing on, instead of dissolving from, the surface. It is possible that the growing matters on the surface, and the substrate cross-section, are some kind of bacteria from the water solutions, since the dimensions are in the same magnitude (1-10 µm). No further investigation of the growing matter on the surface was done, but the findings were used to improve the sample preparation of the KNN50 and Ca05KNN50 thin films before mechanical testing. The grain structure of the KNN50 and Ca05KNN50 thin films seems unchanged after soaking, but the films had partly dissolved some places on the surface, as seen in Figure 4.17.

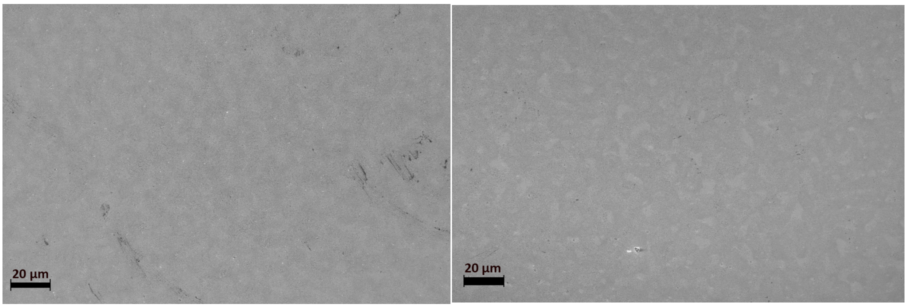

(a) Non-soaked **(b)** 1 day

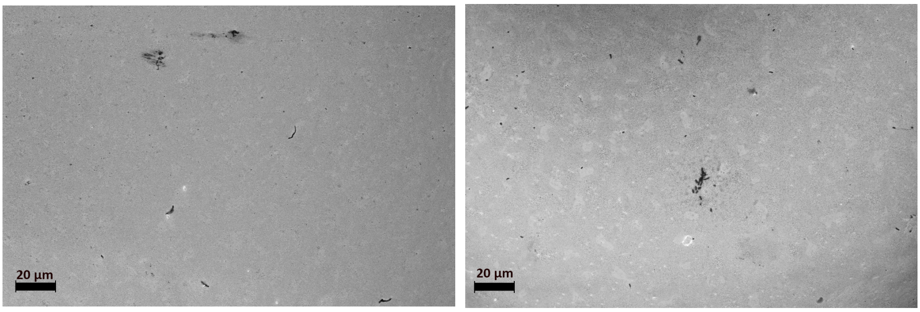

(c) 3 days **(d)** 6 days

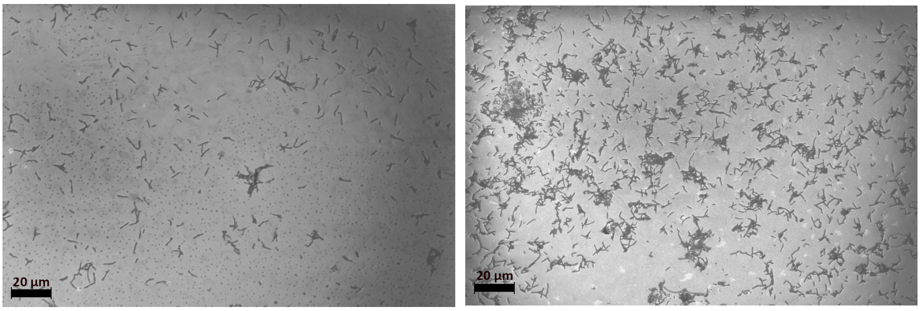

(e) 10 days **(f)** 14 days

Figure 4.13: SEM images of Ca05KNN25 thin films showing the development of potential bacteria on the surface during soaking of the films in distilled water at 37 °C.

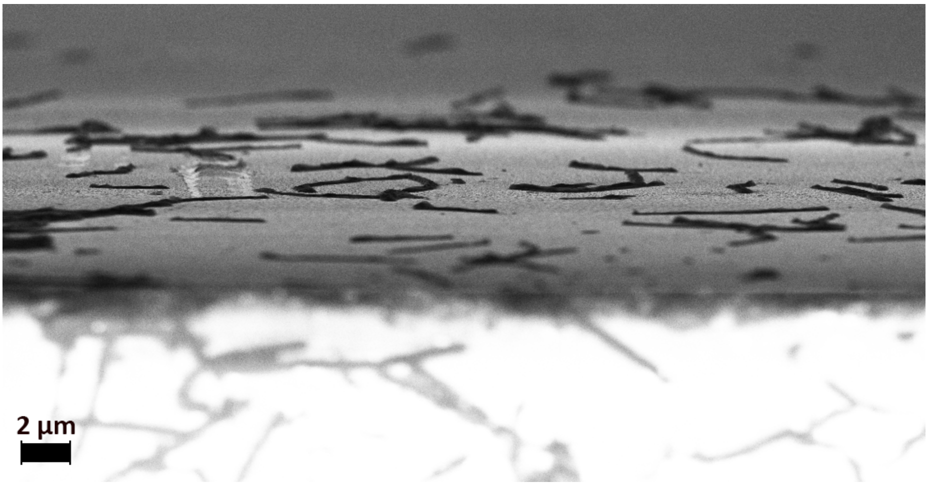

Figure 4.14: SEM cross section image showing the potential bacteria on the surface of the Ca05KNN50 thin films.

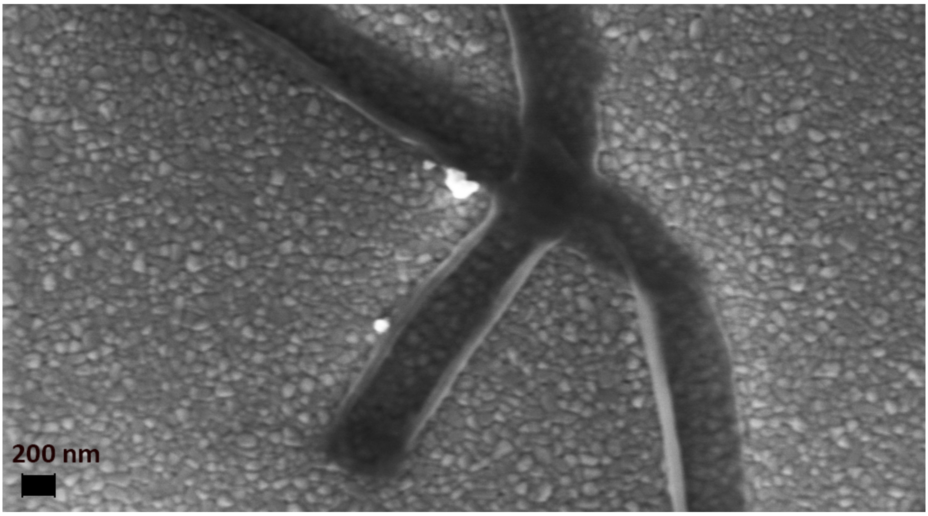

Figure 4.15: SEM image showing the potential bacteria on the surface of the Ca05KNN50 thin films.

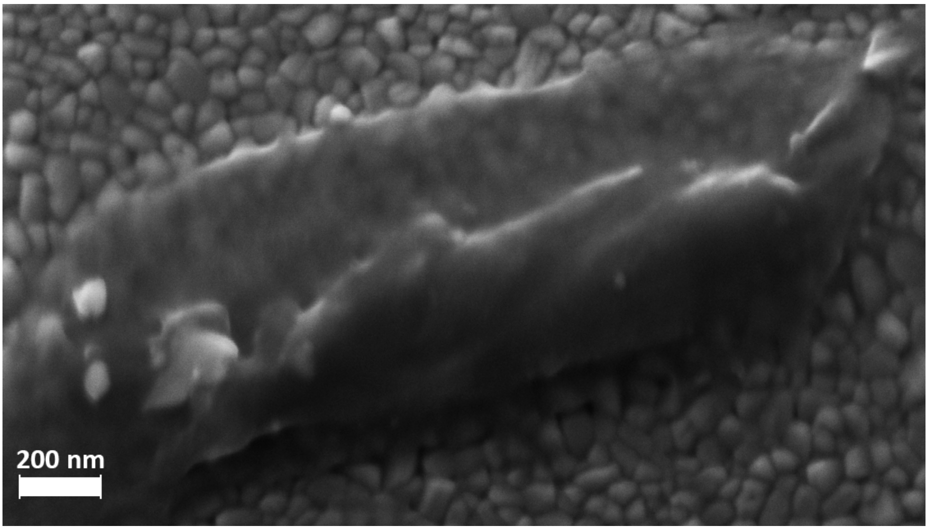

Figure 4.16: SEM image showing the potential bacteria on the surface of the Ca05KNN50 thin films.

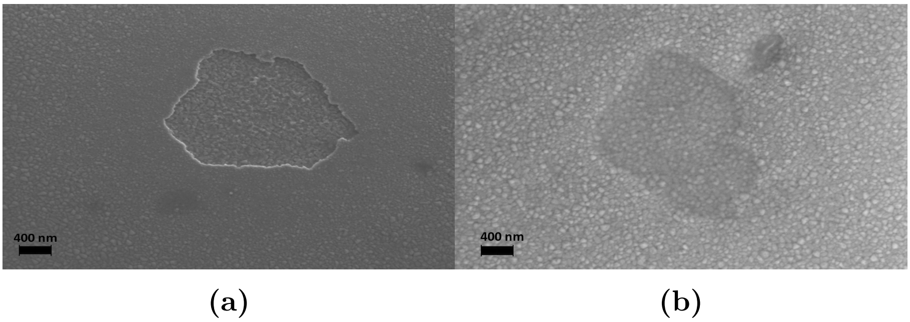

(a) **(b)**

Figure 4.17: SEM images of Ca05KNN50 thin films soaked for 2 (a) and 14 (b) days. The images show parts of the surface where the films are partly dissolved.

4.2.3 Mechanical properties

Figure 4.18 shows one set of the loading-displacement curves obtained from the nanoindentation on the KNN25 and Ca05KNN25, KNN50 and Ca05KNN50 thin films. All recorded loading-displacement curves are included in Appendix E.

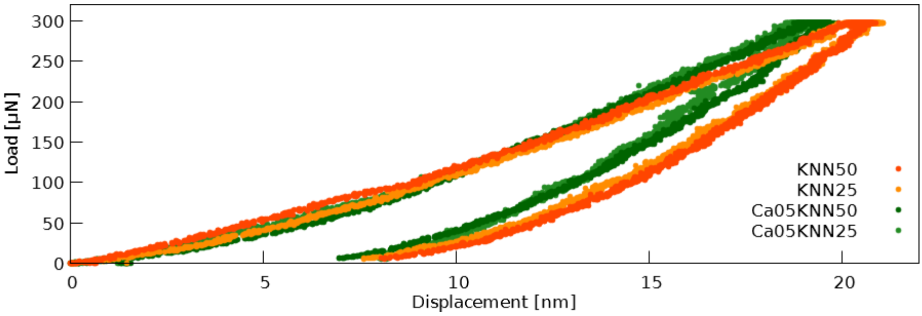

Figure 4.18: One set of the loading curves from nanoindentation measurements on KNN25, KNN50, Ca05KNN25 and Ca05KNN50 thin films.

Average reduced modulus (E_r) and hardness (H), and standard deviations were measured based on 6-9 indents on each of the KNN25 and Ca05KNN25 thin films, and 9 indents on the KNN50 and Ca05KNN50 thin films. Number of indents on each sample, calculated average reduced modulus and hardness values, and standard deviations are included in Appendix E.

Figure 4.19 and Figure 4.20 show the calculated average reduced modulus and hardness of the KNN25 and Ca05KNN25 thin films, respectively, and how the values changes during soaking time. As seen in the Figures, the obtained standard deviations, from 6-9 indents on KNN25 and Ca05KNN25 thin films, are quite large. This is believed to be a result of an inhomogeneous surface structure and

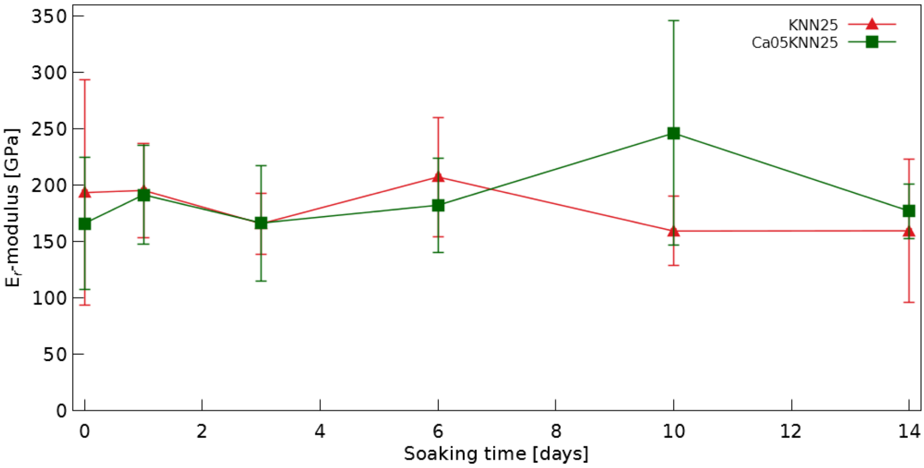

Figure 4.19: Average reduced modulus (E_r-modulus) varying with soaking time for KNN and Ca-KNN with 2.5 mol% alkali excess.

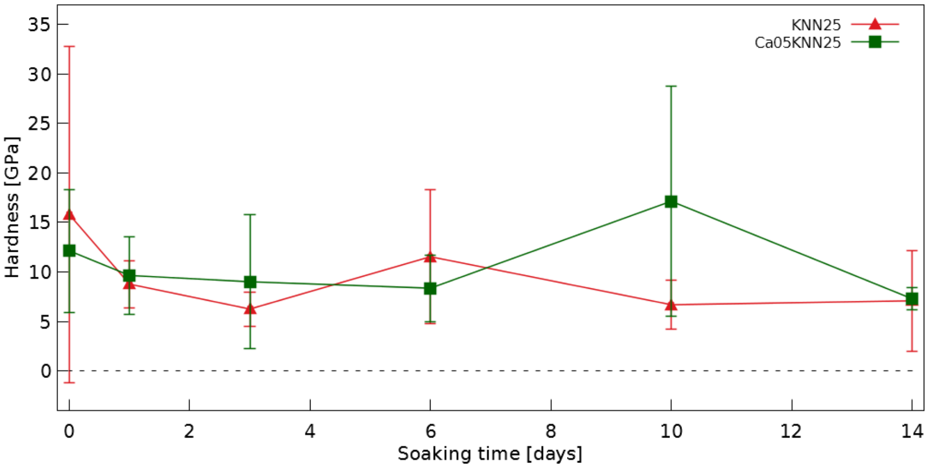

Figure 4.20: Average hardness varying with soaking time for KNN and Ca-KNN with 2.5 mol% alkali excess.

improper sample preparation before the indentation. The E_r varies from 159-206 and 165-245 GPa, and the H from 6.2-15.7 and 7.3-17.1 GPa for KNN25 and Ca05KNN25 thin films, respectively. Some key observation should be noticed when looking at the Figures. First, disregarding the high deviations, the trends are quite stable during the soaking time. Secondly, both the calculated E_r and hardness of the Ca05KNN25 thin film after being soaked for 10 days are noticeable larger compared to the other values.

The change in the calculated average E_r and average hardness during soaking time of

the KNN50 and Ca05KNN50 thin films is presented in Figure 4.21 and Figure 4.22, respectively. The standard deviations are much smaller in these measurements, and is believed to be due to improved sample preparation before the indentation measurements. The E_r varies from 172-210 and 190-203 GPa, and the H from 6.2-10.7 and 8.9-10.3 GPa for KNN50 and Ca05KNN50 thin films, respectively. The average reduced moduls in the KNN50 and Ca05KNN50 thin films is not remarkable affected by the soaking. Also, the trend in average hardness is quite stable although, the changes are more noticeable compared to the average reduced moduls.

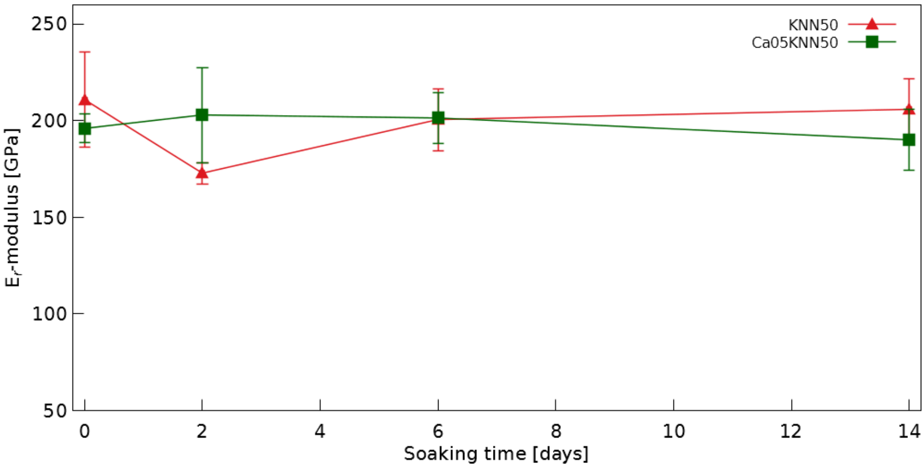

Figure 4.21: Average reduced modulus (E_r-modulus varying with soaking time for KNN and Ca-KNN with 5.0 mol% alkali excess.

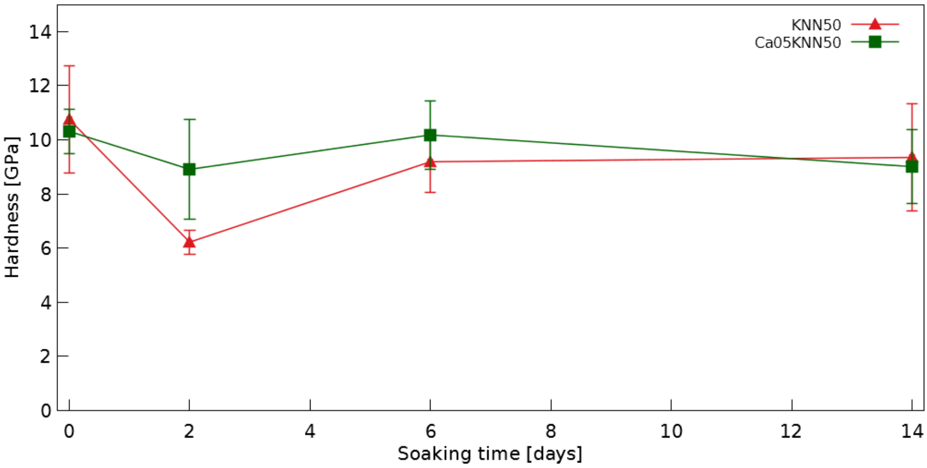

Figure 4.22: Average hardness varying with soaking time for KNN and Ca-KNN with 5.0 mol% alkali excess.

4.2.4 Piezo- and ferroelectric properties

Table 4.2 shows the measured piezoelectric coefficients (d_{33}) of the KNN50 and Ca05KNN50 thin films deposited on (100)-oriented Nb:STO substrates. The d_{33} value of Ca05KNN50 is slightly larger compared to KNN50.

Table 4.2: Measured piezoelectric coefficient (d_{33}) of KNN50 and Ca05KNN50 thin films deposited on (100)-oriented Nb:STO substrates.

Sample	d_{33} **[pC/N]**
KNN50	17.44 ± 0.69
Ca05KNN50	18.59 ± 0.16

Hysteresis curves of polarisation vs. electric field are shown in Figure 4.23 and Figure 4.24 for KNN50 and Ca05KNN50 thin films deposited on conducting (100)-oriented Nb:STO substrates, respectively. The hysteresis loops are all similar in shape, with the exception of the Ca05KNN50 thin film measured at 1.0 V, which is more rounded than the other measurements. The other measurements are more similar to ferroelectric hysteresis loops, however the rounded shape before the saturation polarisation indicates high leakage current in all of the samples.

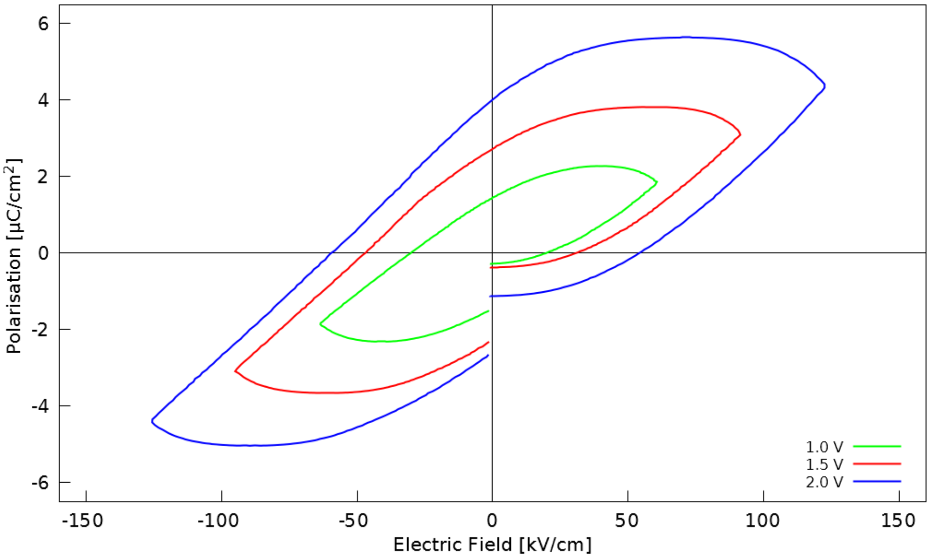

Figure 4.23: Measured hysteresis curves of polarisation vs. electric field at 1 Hz frequency of KNN50 thin films deposited on (100)-oriented Nb:STO substrates.

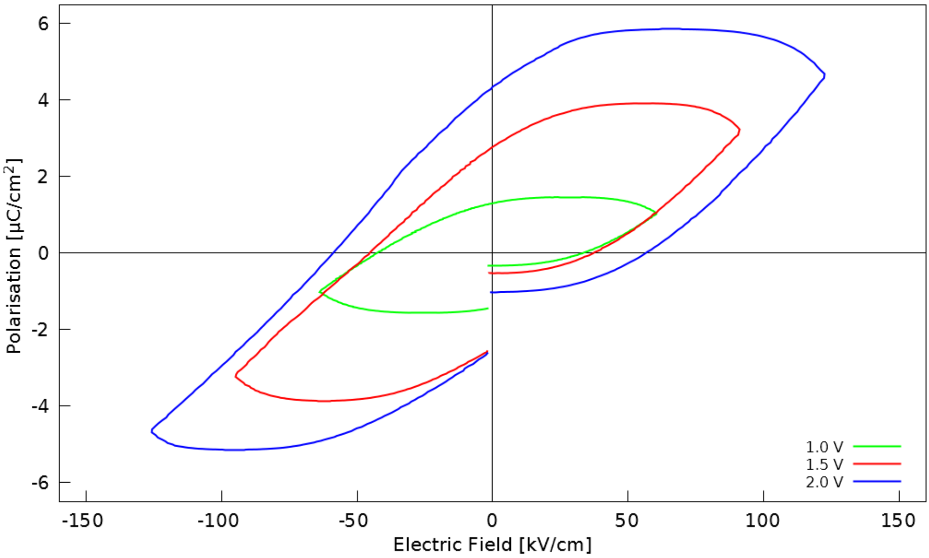

Figure 4.24: Measured hysteresis curves of polarisation vs. electric field at 1 Hz frequency of Ca05KNN50 thin films deposited on (100)-oriented Nb:STO substrates.

Chapter 5

Discussion

The overall goal is to produce high quality KNN thin films, which can be used for biomedical applications. Excess amounts of alkali metal ions are introduced to prevent formation of unwanted secondary phases after pyrolysis and annealing. The introduction of calcium (Ca^{2+}) to the perovskite lattice may reduce the hygroscopic nature of KNN when exposed to an aqueous environment. The first part of this Chapter discuss the effect of introducing Ca^{2+} and excess amounts of alkali metal ions in the precursor solutions, while the second part focuses on the thin film properties and how they are affected by alkali excess, introduction of Ca^{2+} and soaking time.

5.1 Precursor stability and phase purity

All $K_{0.5}Na_{0.5}NbO_3$ (KNN) and $K_{0.495}Na_{0.495}Ca_{0.005}NbO_3$ (Ca-KNN) precursor solutions were stable for more than four months, while the complexed niobium malic acid precursor solution started to precipitate after three to four weeks. High valency cations with small radius like Nb^{5+} are very sensitive to hydrolysis, and consequently condensation reactions.[39] If the pH of the solution is too low, the niobium complex will break down by shifting the deprotonation equilibrium of the carboxylic acid as seen in Figure 5.1. Precipitation of a hydrated niobium oxide after a few weeks indicates a quite slow

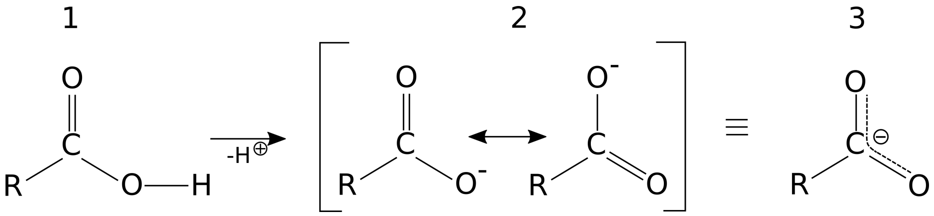

Figure 5.1: Schematic illustration of deprotonation of the carboxylic acid.[39]

hydrolysis rate. Although, one month stability can be regarded as acceptable in industrial production, the stability of the niobium precursor solution can be improved by increasing the pH between 7 and 8. The KNN and Ca-KNN precursor solution were stable for about 4-5 months. This can be explained by the basic nature of the alkali metals rising the pH, and thus the stabilisation, when mixed with the niobium precursor.

5.1.1 Effect of alkali excess

As seen in Figure 4.1, the KNN-precursor solution without any alkali excess (KNN00) forms a niobium rich secondary phase ($K_4Nb_6O_{17}$) after calcination at 550 °C, while all precursor solution containing either 2.5 mol% or 5.0 mol% alkali excess formed phase pure KNN with diffraction patterns fitting well to the space group *Pm*. Calcined powders from KNN precursor solutions based on niobium oxalate, instead of the niobium malic acid complex, also forms niobium rich secondary phases at lower temperatures.[17,54,55] Even though the secondary phase disappears at higher calcination temperatures (above 500 °C), it has been a challenge to produce phase pure thin films from the precursor solutions that contains secondary phases at lower calcination temperatures. Due to this knowledge, only KNN and Ca-KNN precursor solutions with excess amounts of alkali were used for the thin film preparation.

The refined parameters in Table 4.1 show a slightly increase in the lattice parameters *a, b* and *c*, and consequently the unit-cell volume, with increasing excess amounts of alkali from 2.5 mol% to 5.0 mol%, while the β angle remained unchanged. The increased unit-cell volume might be explained by either elimination of A-site vacancies, or by a higher K/Na-ratio in the perovskite KNN phase with increasing amounts of alkali excess. All the unit-cell parameters are a bit smaller compared to the lattice parameters obtained by Tellier *et al.*[37] on bulk powders. This is opposite of what to expect, since noncrystalline powders tends to show a expansion in the unit cell due to finite-size effects.[71] However, the synthesis routes are quite different, and the variations in lattice parameters may vary due to different amount of strain or slightly variations in composition within the materials.

Volatility of K and Na during heat treatment of KNN is well known and causes A-site vacancies, compansated by oxygen vacancies, in the perovskite phase.[9,10,15,16] Excess amounts of alkali metals in the precursor solution inhibits the formation of A-site vacancies during heating, and is in agreement with the increased unit-cell volume. Haugen *et al.*[18] have reported that K is more volatile than Na during sintering at high temperatures. Tellier *et al.*[37] have reported systematic increase in the unit-cell volume when increasing the K/Na ratio from 0.67 to 1.5. However, there is not enough data from the results to say anything about the K/Na ratio. Also, since the amount of alkali excess in the solutions are even for K and Na, it is more likely to expect the increased unit-cell volume due to reduction of A-site vacancies.

5.1.2 Effect of doping with calcium

A marginal decrease in unit-cell volume can be observed from the refined parameters in Table 4.1, as well as a slightly increase in the β angle, when introducing Ca to the precursor solutions. Introduction of Ca^{2+} to the perovskite lattice creates A-sites vacancies, according to Equation 5.1:

$$\mathrm{AEO} \xrightarrow{\mathrm{A_2O}} \mathrm{AE}_{\mathrm{A}}^{\bullet} + \mathrm{V}_{\mathrm{A}}' + \mathrm{O}_{\mathrm{O}}^{\times} \tag{5.1}$$

Hence, a decrease in the unit-cell volume should be expected if Ca takes place at the A-site. More A-site vacancies may also alter the monoclinic distortion somehow, and might explain the slightly increased β angle. It should be kept in mind that the amount of Ca in the precursor solutions is very low (0.5 mol%), and the number of samples with refined data are not significant. However, the results indicates that Ca have been introduced to the KNN perovskite phase.

5.2 Thin film properties

Only the KNN and Ca-KNN precursor solutions with 2.5 mol% or 5.0 mol% alkali excess were used for thin film preparations, in order to avoid formation of niobium rich secondary phases during film processing.

5.2.1 The effect of alkali excess

As seen in Figure 4.5, both KNN25 and Ca05KNN25 thin films formed the $K_4Nb_6O_{17}$ secondary phase after annealing at 700 °C, although calcined powders from the precursor solutions showed a phase pure KNN phase at the same temperature. Thin films have a higher surface area per mass, compared to bulk powder, and the film surface is also more exposed to surrounding air during the heating process. This makes the evaporation of K and Na more easy from the film surface during heating, and may explain why the niobium secondary phase is formed in the thin films, and not the powders. The results confirm that the formation of phase pure KNN strongly depends on K and Na excess amounts, especially when working with thin films. Nakashima *et al.*[15] reported 10 mol% alkali excess to be optimal for compensating loss and improve ferroelectric properties. Ahn *et al.*[10] have suggested 20 mol% excess in order to obtain phase pure KNN thin films with optimum ferroelectric properties, while Kupec *et al.*[16] reported only 5 mol% of potassium to be sufficient for the phase purity and ferroelectric properties. Hence, depended on the synthesis and precursor systems, different amounts of alkali excess are needed, and it is clear that more research are required in order to know how much alkali excess there is needed.

The $K_4Nb_6O_{17}$ secondary phase formed in the Ca05KNN25 and KNN25 films is known to be highly hygroscopic.[59,60] This is also confirmed by the X-ray diffractograms obtained after soaking the thin films for several days, where the secondary phase seems to be dissolved. Figure 4.6 and Figure 4.7 show that the peaks from the niobium rich secondary phase disappears only after one day, and no peaks are detected after 14 days in water at 37 °C. The pH developement plottet in Figure 4.4 show a reduction in pH during the first soaking days, which is opposite to what was found in previous pH measurements on bulk powders.[17] An explanation may be that dissolved $K_4Nb_6O_{17}$ from the films contains Nb^{5+} ions, that are high valency and small cations with an acid nature, and an increase in pH would be expected if Nb^{5+} ions are released into the water. Also, the further increase in pH after two days until six days might be explained by either condensation of the dissolved niobium ions,[39] or by KNN dissolving from the film surface. Although more experiments like ion-release tests are needed in order to confirm this theories, the obtained x-ray diffractograms after soaking the films show promising results on the phase purity, and the potential use of KNN thin films *in vivo*.

The amount of alkali excess also affects the microstructure of the films. As seen in Figure 4.12 KNN50 (c) and Ca05KNN50 (d) have a uniform and homogeneous grain structure, with a quite small grain size, while the KNN25 (a) and Ca05KNN25 (b) show a more inhomogeneous microstructure with different grain morphologies. The formation of niobium rich secondary phases at the surface are expected to give different grain structures. Work presented by Pham[54] has suggested the niobium secondary phase to have an elongated grain structure. However, such grain stuctures were not seen from the SEM images of the surface. The amount of niobium secondary phases in the KNN25 and Ca05KNN25 films are much lower compared to those in Phams work, although there is a possibility that the inhomogenous grain structure is caused by a secondary phase on the surface.

Both the nucleation- and growth rate are of the greatest importance in order to obtain a homogeneous fine-grained structure. Kupec *et al.*[16] have reported different microstructures on the surface of KNN thin films depended on the amount of alkali excess. They also reported high K/Na compositional inhomogeneity on the surface of stochiometric KNN thin films, which where reduced by increasing the amount of alkali excess. Thus, the inhomogeneous grain structure in KNN25 and Ca05KNN25 can be explained by different K/Na atomic ratio, or different nucleation- and growth rates due to different amounts of alkali excess.

5.2.2 The effect of heating rate

Previous work, done by the author,[17] showed two different grain morphologies (Figure 5.2) with different roughness on the surface of KNN thin films with 5 mol% alkali excess, made by the same precursor solution. This feature has not been observed in the KNN50 and Ca05KNN50 thin films produced during this project and is believed to be due to different thermal processing during pyrolysis and annealing. The same pyrolysis (550 °C) and annealing (700 °C) temperatures were used based on same thermogravimetric analysis results (Figure 4.3). The procedure in this work has been done by using a heating source below the substrate, instead of a heating source above, which may have influenced the nucleation and crystal growth during the film deposition. The annealing of the thin films produced in the earlier work where conducted in a tube furnace with a considerably slower heating rate ($200\,^{\circ}\mathrm{C\,h^{-1}}$). The heating rate during annealing, in this work, where much faster ($100\,^{\circ}\mathrm{C\,min^{-1}}$), and the process were conducted on the same heating plate as the pyrolysis. As seen in the SEM images, this implies that a faster heating rate prevents distinct grain growth, and thus gives a homogeneous grain structure. Also, the rapid heating plate set-up seems to be beneficial for columnar growth (Figure 4.10 and Figure 4.11), which is promising regarding the potential of making textured thin films.

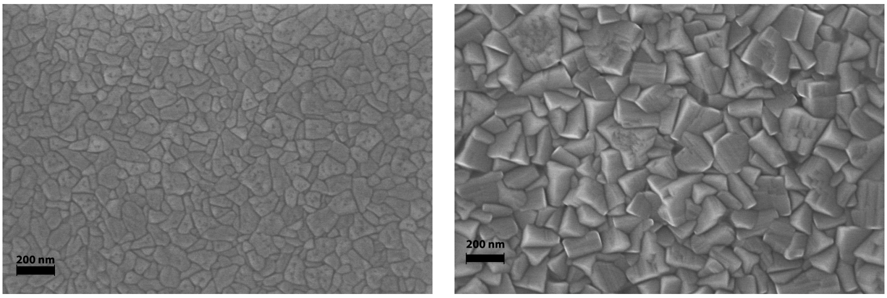

(a) Fine area. **(b)** Coarse area.

Figure 5.2: SEM images of KNN thin films with 5 mol% alkali excess, showing two different grain morphologies and their distribution on the surface, reprinted from previous work.[17]

5.2.3 The effect of doping with calcium

The revealed amount of $K_4Nb_6O_{17}$ secondary phase in Ca05KNN25 thin films are smaller compared to the KNN25, which might indicate Ca^{2+} being introduced into the KNN perovskite lattice. During heat treatment, Ca^{2+} may compensate the alkali loss by occupy the A-sites of the perovskite, and suppressing the formation of the niobium rich secondary phase. Due to the reduced amount of secondary phase in Ca doped KNN thin films, with 2.5 mol% alkali excess, it is acceptable to assume some of the Ca^{2+} occupying the A-sites in the KNN perovskite lattice.

Microstructural changes

As seen in Figure 4.12 Ca doping in KNN with 5.0 mol% alkali excess results in almost unchanged grain structure, while Ca doping in KNN with 2.5 mol% alkali excess produces phases containing larger cubic grains on the surface. Taub *et al.*[61] have reported similar development in bulk KNN doped with 0.5 - 2.0 mol% Ca, and this is believed to be related to the substitution of Na^+ or K^+ with Ca^{2+}, causing A-site vacancies in which promotes grain growth.[61,62] These larger cubic grains are only observed in the Ca05KNN25 and not in the KNN25 thin films, which may verify that Ca^{2+} are introduced in the KNN lattice. As previously discussed, increased amounts of alkali excess prevents grain growth and may explain why larger cubic grains are only seen in the Ca05KNN25 thin films.

Mechanical properties

The nanoindentation measurements were conducted to evaluate the mechanical properties and how they changes when KNN and Ca-KNN thin films were exposed to water solution for various time lengths. As seen in Figure 4.19 and Figure 4.20, large standard deviations were obtained from the measurements conducted on KNN and Ca-KNN thin films with 2.5 mol% alkali excess. The inhomogeneous microstructure of KNN25 and Ca05KNN25 thin films (Figure 4.12) may bring large deviations, due to very small displacement and deformation volume during the experiments. Also, if an indent is made on some of the potential bacteria on the surface (Figure 4.14 - Figure 4.16), it would influence the values and deviations during the experiments, since the bacteria are expected to be much softer. Thus, an evaluation of exact values and changes are not possible, due to high standard deviations in the measurement. However, the trends indicates that both the hardness and reduced modulus are quite stable after 14 days of soaking, which is promising regarding the biocompatibility and reliability of KNN thin films inside the body.

Smaller deviations in the measurements conducted on the KNN and Ca-KNN thin films with 5.0 mol% alkali excess might be explained by a more homogeneous grain structure (Figure 4.12), and also removal of the potential soft bacteria from the surface, due to new sample preparation. The trends in Figure 4.21 and Figure 4.22 show only small changes in the avarage reduced modulus or hardness, when doping with calcium, and both KNN50 and Ca05KNN50 share the same trends throughout the 14 days of soaking. However, the results might suggest that the reduced modulus and hardness are slightly more stable during soaking for the Ca-doped KNN films.

The obtained hardness and reduced modulus of the KNN50 and Ca05KNN50 thin films are much larger compared to those previously reported on sol-gel prepared KNN thin films by Bruncková *et al.*[51,52] (E_r = 91 and 71 GPa, and H = 4.5 GPa). This might be explained by the use of different substrates ($SrTiO_3$) in this work, compared to Bruncková *et al.* (Pt/Al_2O_3 and $Pt/Si_2/Si$), which have been reported to influence the microstructure and thus the mechanical properties of thin films.[51] The elastic modulus reported by Kugler *et al.*[47] (207 and 205 GPa), and the hardness (11 and 12 GPa) are in the same range as the results obtained during this work, although the preparation method (magnetron sputtering) and the substrate (SiO_2/Si) are different. These results confirm that the mechanical properties are strongly influenced by the substrate, and the microstructure and surface structure of the thin films.[47,52]

Ferroelectric- and piezoelectric properties

Both the KNN50 and Ca05KNN50 thin films exhibit weak and leaky ferroelectric *P*-*E* hysteresis loops (Figure 4.23 and 4.24), which indicates high conductivity within the films.[19] Large conductivity submerges the polarisation caused by domain switching and makes it hard to extract the ferrolectric properties from the obtained *P*-*E* hysteresis loops.[20] However, the results show some hysteresis characteristics like a slightly saturated polarisation and concave shape that may evidence for ferrolectricity.[19]

The weak ferroelctric hysteresis loops may be explained by the small grain size (82-86 nm) and thickness (153-168 nm) of the KNN50 and Ca05KNN50 thin films, as seen in Figure 4.12 (c) and (d), and Figure 4.10 and 4.11. The dielectric permittivity tends to decrease with decreasing grain size, which affects the ferroelectric properties.[20] Both the domain structure and domain wall motions are depended on the grain size of the material. When the grain size decrease below 100 nm, it approaches the ferroelectric domain size. Thus, polycrystalline thin films with small grain sizes tends to have high domain wall density, but low domain wall mobility compared to bulk ceramics, due to self-clamping effects.[19,20] This restricts domain switching and polarisation rotation, and may be an explanation of the weak hysteresis loops.

Extrinsic thermal stresses will be induced upon cooling if there is a mismatch between the thermal expansion coefficients of the film and substrate. There are, to the best of the authors knowledge, no published data on the thermal expansion coefficient of KNN. However, if it is smaller compared to the Nb-doped STO substrate, tensile stresses within the film induces domains with polarisation vectors in the plane, instead of out of the plane.[72] Thus the weak ferroelectric hysteresis loops may be explained by the out of plane measurements on the films.

A combined plot of polarisation vs. electric field of the KNN50 and Ca05KNN50 thin films is given in Figure 5.3. The region where the polarisation is saturated seems to be somewhat wider for the Ca05KNN50 thin films compared to the KNN50 thin films, indicating some smaller degree of leakage current. Ahn *et al.*[10] proposed generated holes ($h^{\bullet}$) to be the carrier of leakage current in KNN thin films, due to heavy loss of K and Na during thermal treatment forming A-site vacancies, accompanied by oxygen vacancies. The oxygen vacancies might be reoccupied by oxygen from the atmosphere, generating $h^{\bullet}$, which increases the leakage current.[10] Addition of Ca^{2+} might compensate these charge defects generated from loss of alkali in the pure KNN thin films, and thus slightly enhance the leakage properties. In order to verify this hypothesis, more measurements on the leakage current have to be performed.

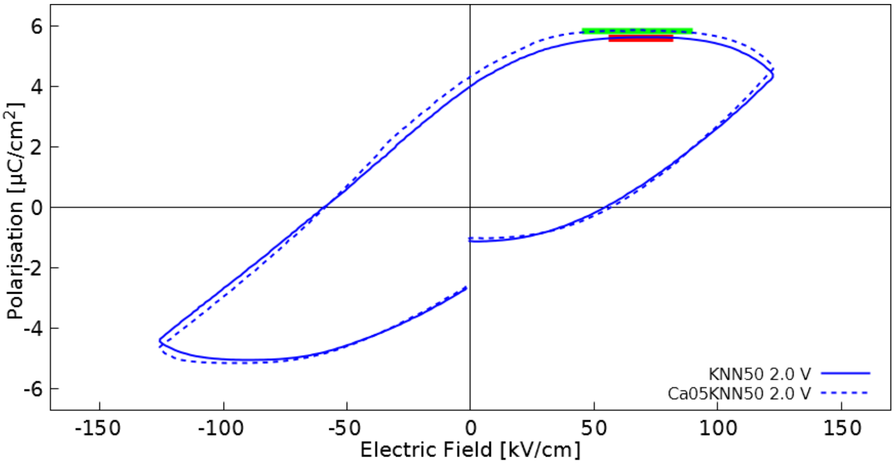

Figure 5.3: Measured hysteresis curves of polarisation vs. electric field at 1 Hz frequency of KNN50 and Ca05KNN50 thin films deposited on (100)-oriented Nb:STO substrates. The red and green colours mark the area for saturated polarisation in KNN50 and Ca05KNN50 thin films, respectively.

The measured piezoelectric coefficients d_{33} (17.4 and 18.6 $\mathrm{pC N^{-1}}$ for KNN50 and Ca05KNN50, respectively) show a slight increase when doping KNN with calcium. The values are smaller compared to the reported values (30.6-83.3[50], 40[10] and 46 $\mathrm{pC N^{-1}}$[15]) on KNN thin films. However, all the measurements are conducted with different set-ups and are therefore not comparable. It should be noticed that the d_{33} values measured on Berlincourt-meters have shown to be strongly depended on the aspect ratio between the film and the substrate. However, since the aspect ratio of the KNN50 and Ca05KNN50 thin films are significally high, the measured d_{33} values are believed to be close to the true d_{33} values of the films.[73]

5.3 Further work

New and promising results on the properties and reliability of KNN thin films were achieved in this work, although further research and improvements are necessary. More studies need to be carried out to understand how the (micro)structural, mechanical, ferroelectric and piezoelectric properties are affected when KNN thin films are exposed to biological environments.

In this study, a parallel plate electrode configuration was used to measure the out of plane ferroelectric properties of the thin films, where the results showed weak ferroelectric response. Therefore, in plane measurements by using other electrode configurations, like interdigiated electrodes, may provide better ferroelectric measurements.

More characterisation of the piezoelectric and ferroelectric properties as well as the dielectric losses in KNN thin films are required. The use of piezoresponse force microscopy (PFM) will be beneficial for more investigation on the piezoelectric properties. Also, further enhancement of the ferroelectric properties are necessary.

Long-term stability of the mechanical properties have not been investigated in this study. SEM images may indicate formation of bacteria on the film surface during soaking and it may be beneficial to further investigate this phenomenon. If more studies are carried out on the change of mechanical properties during soaking, sterilised equipment and solutions should be considered in order to avoid potential bacteria contamination on the surface.

Neither ferroelectric or piezoelectric measurements were conducted on soaked thin films. In the long term, to evaluate the potential for utilising piezoelectric KNN thin films in biomedical applications, this will need to be investigated.

Chapter 6

Conclusion

In this study, $K_{0.5}Na_{0.5}NbO_3$ and (KNN) $K_{0.495}Na_{0.495}Ca_{0.005}NbO_3$ (Ca-KNN) thin films have been synthesised by chemical solution deposition of an aqueous precursor solution onto $SrTiO_3$ substrates. Various amounts of alkali excess were added to the precursor solutions to compensate alkali loss during thermal processing. 5.0 mol% alkali excess was sufficient to obtain phase pure KNN and Ca-KNN thin films, while Nb rich secondary phases were found in the thin films containing 2.5 mol% alkali excess.

The effect of doping with 0.5 mol% Ca^{2+} in KNN on the mechanical properties was studied by nanoindentation on the films after exposure to water solutions at 37 °C, for 0 to 14 days. Ca-KNN thin films show slightly more stable mechanical properties during soaking, however, the effect of doping with 0.5 mol% Ca^{2+} in KNN was relatively subtle.

Doping with Ca^{2+} gave a weak enhancement of the piezoelectric coefficients d_{33} (18.6 ±0.16 pC/N) compared to pure KNN thin films (17.44 ±0.69 pC/N). All thin films displayed poor ferroelectric hysteresis loops and further improvements of the ferroelectric properties are necessary. However, relatively stable mechanical properties during 14 days of soaking indicates that ferroelectric KNN thin films are promising candidates for biomedical applications.

Bibliography

[1] B. Jaffe, W. Cook, and H. Jaffe. *Piezoelectric Ceramics*, volume **41**. Academic Press, 1971.

[2] J. Rödel, W. Jo, K. T. P. Seifert, E. M. Anton, T. Granzow, and D. Damjanovic. Perspective on the development of lead-free piezoceramics. *J. Am. Ceram. Soc.*, **92**:1153–1177, (2009).

[3] Council of European Union. Rohs directive 2002/95/ec, 2003. `http://ec.europa.eu/environment/waste/rohs_eee/index_en.html`.

[4] J. Wu, D. Xiao, and J. Zhu. Potassium-sodium niobate lead-free piezoelectric materials: Past, present, and future of phase boundaries. *Chem. Rev.*, **115**:2559–2595, (2015).

[5] S. W. Yu, S. T. Kuo, W. H. Tuan, Y. Tsai, and C. H. Su. Ion release from three lead-free piezoelectric ceramics and their physical and cytotoxicity characteristics. *Mater. Lett.*, **65**:3522–3524, (2011).

[6] S. W. Yu, S. T. Kuo, W. H. Tuan, Y. Y. Tsai, and S. F. Wang. Cytotoxicity and degradation behavior of potassium sodium niobate piezoelectric ceramics. *Ceram. Int.*, **38**:2845–2850, (2012).

[7] Y. Saito, H. Takao, T. Tani, T. Nonoyama, K. Takatori, T. Homma, T. Nagaya, and M. Nakamura. Lead-free piezoceramics. *Nature*, **432**:84–87, (2004).

[8] J. Rödel, K. G. Webber, R. Dittmer, W. Jo, M. Kimura, and D. Damjanovic. Transferring lead-free piezoelectric ceramics into application. *J. Eur. Ceram. Soc.*, **35**:1659–1681, (2015).

[9] J.-F. Li, K Wang, F.-Y. Zhu, L.-Q. Cheng, and F.-Z. Yao. $(K, Na)NbO_3$-based lead-free piezoceramics: Fundamental aspects, processing technologies, and remaining challenges. *J. Am. Ceram. Soc.*, **96**:3677–3696, (2013).

[10] C. W. Ahn, S. Y. Lee, H. J. Lee, A. Ullah, J. S. Bae, E. D. Jeong, J. S. Choi, B. H. Park, and I. W. Kim. The effect of K and Na excess on the ferroelectric and piezoelectric properties of $K_{0.5}Na_{0.5}NbO_3$ thin

films. *J. Phys. D. Appl. Phys.*, **42**:215304, (2009).

[11] Y. Chang, Z. Yang, X. Chao, R. Zhang, and X. Li. Dielectric and piezoelectric properties of alkaline-earth titanate doped $(K_{0.5}Na_{0.5})NbO_3$ ceramics. *Mater. Lett.*, 61:785–789, (2007).

[12] A. Safari and M. Abazari. Lead-Free Piezoelectric Ceramics and Thin Films. *IEEE Trans. Ultrason., Ferroelectr., Freq. Control*, **57**, (2010).

[13] B. Malic, J. Bernard, J. Holc, D. Jenko, and M. Kosec. Alkaline-earth doping in $(K, Na)NbO_3$ based piezoceramics. *J. Eur. Ceram. Soc.*, **25**:2707–2711, (2005).

[14] P. Mahesh and D. Pamu. Effect of deposition temperature on structural, mechanical, optical and dielectric properties of radio frequency sputtered nanocrystalline $(K_xNa_{1-x}NbO_3$ thin films. *Thin Solid Films*, **562**:471 – 477, 2014.

[15] Y. Nakashima, W. Sakamoto, T. Shimura, and T. Yogo. Lead-Free Piezoelectric $(K,Na)NbO_3$ Thin Films Derived from Metal Alkoxide Precursors. *Jpn. J. Appl. Phys.*, **46**:6971–6975, (2007).

[16] A. Kupec, B. Malic, J. Tellier, E. Tchernychova, S. Glinsek, and M. Kosec. Lead-free ferroelectric potassium sodium niobate thin films from solution: Composition and structure. *J. Am. Ceram. Soc.*, **95**:515–523, (2012).

[17] Dale S. M. *Lead-Free Piezoelectric Materials for Medical Technology.* Specialisation Project, Norwegian University of Technology and Science, 2017.

[18] Haugen A. *Synthesis and characterisation of textured lead-free piezoelectric ceramics.* PhD thesis, Norwegian University of Science and Technology, 2014.

[19] L. Jin, F. Li, and S. Zhang. Decoding the fingerprint of ferroelectric loops: Comprehension of the material properties and structures. *J. Am. Ceram. Soc.*, **97**:1 – 27, 2014.

[20] T. M. Shaw, S. Trolier-McKinstry, and P. C. McIntyre. The properties of ferroelectric films at small dimensions. *Annu. Rev. Mater. Sci.*, **30**:263–298, 2000.

[21] A.R. West. *Solid State Chemistry and its Applications.* Chichester: Wiley, second edition, 2014.

[22] R. J. D. Tilley. *Understanding Solids: The Science of Materials.* Chichester: Wiley, second edition, 2013.

[23] K. Momma and F. Izumi. Vesta: a three-dimensional visualization system for eletronic and structural analysis. *J. Appl. Crystallogr.*, **41**:1272–1276, (2008).

[24] B. D. Ratner, A. S. Hoffman, J. E. Lemons, and F. J. Schoen. *Biomaterials Science: An Introduction to Materials in Medicine.* Elsevier Academic Press, second edition, 2004.

[25] D. F. Williams. On the mechanisms of biocompatibility. *Biomaterials*, **29**:2941–2953, (2008).

[26] D. F. Williams. *The Williams Dictionary of Biomaterials.* Liverpool University Press, (1999).

[27] L.L. Hench and J.M. Polak. Third-generation Biomedical Materials. *Science*, **295**:1014–1017, (2002).

[28] B. Gupta, N. Revagade, and J. Hilborn. Poly(lactic acid) fiber: An overview. *Prog. Polym. Sci.*, **32**:455–482, (2007).

[29] J. D. Enderle, J. D. Bronzino, and S. M. Blanchard. *Introduction to biomedical engineering.* Boston: Elsevier Academic Press, second edition, 2005.

[30] S. Bauer, P. Schmuki, K. von der Mark, and J. Park. Engineering biocompatible implant surfaces: Part I: Materials and surfaces. *Prog. Mater Sci.*, **58**:261–326, (2013).

[31] J. Soar, G.D. Perkins, G. Abbas, A. Alfonzo, A. Barelli, J.J. Bierens, H. Brugger, C.D. Deakin, J. Dunning, M. Georgiou, A.J. Handley, D.J. Lockey, P. Paal, C. Sandroni, K.C. Thies, D.A. Zideman, and J.P. Nolan. European Resuscitation Council Guidelines for Resuscitation 2010 Section 8. Cardiac arrest in special circumstances: Electrolyte abnormalities, poisoning, drowning, accidental hypothermia, hyperthermia, asthma, anaphylaxis, cardiac surgery, trauma, pregnancy, electrocution. *Resuscitation*, **81**:1400–1433, (2010).

[32] B. T. Matthias and J. P. Remeika. Dielectric properties of sodium

and potassium niobates. *Phys. Rev.*, **82**:727–729, Jun 1951.

[33] G. Shirane, R. Newnham, and R. Pepinsky. Dielectric properties and phase transitions of $NaNbO_3$ and $(Na,K)NbO_3$. *Phys. Rev.*, **96**:581–588, (1954).

[34] L. Egerton and D.M Dillon. Piezoelectric and dielectric properties of Ceramics in the System Potassium-Sodium Niobate. *J. Am. Ceram. Soc.*, **42**:438–442, (1959).

[35] E. A. Wood. Polymorphism in potassium niobate, sodium niobate, and other ABO_3 compounds. *Acta Crystallogr.*, **4**:353–362, Jul 1951.

[36] Y. Shiratori, A. Magrez, and C. Pithan. Particle size effect on the crystal structure symmetry of $K_{0.5}Na_{0.5}NbO_3$. *J. Eur. Ceram. Soc.*, **25**:2075–2079, 2005. Elecroceramics IX.

[37] J. Tellier, B. Malic, B. Dkhil, D. Jenko, J. Cilensek, and M. Kosec. Crystal structure and phase transitions of sodium potassium niobate perovskites. *Solid State Sci.*, **11**:320–324, 2009.

[38] Handbook of nanostructured thin films and coatings : Vol. 1 : Mechanical properties, 2010.

[39] T. Schneller, R. Waser, M. Kosec, and D. Payne. *Chemical Solution Deposition of Functional Oxide Thin Films.* Wien: Springer-Verlag, first edition, 2013.

[40] R. W. Schwartz, T. Schneller, and R. Waser. Chemical solution deposition of electronic oxide films. *C. R. Chimie*, **7**:433–461, (2004).

[41] A. Chowdhury. Recent developments in the area of sodium potassium niobate (nkn) thin films by chemical solution deposition methods. In X. L. Huang and S. L. Ma, editors, *Ferroelectrics: New Research*, chapter 8, pages 247–260. New York: Nova, 2012.

[42] C. K. Jørgensen. *Inorganic complexes.* London: Academic Press, (1963).

[43] R.L Gufstason. Polymerization of metal chelates in aqueous solution. *J. Chem. Educ.*, **37**:603–606, (1960).

[44] R. Roy. Gel Route to Homogeneous Glass Preparation. *J. Am. Ceram. Soc.*, **52**:344–344, (1969).

[45] P. W. McMillan. *Glass-ceramics.* London: Academic Press, second edition, 1979.

[46] K. Shibata, F. Oka, A. Nomoto, T. Mishima, and I. Kanno. Crystalline Structure of Highly Piezoelectric (K, Na)NbO_3 Films Deposited by RF Magnetron Sputtering. *Jpn. J. Appl. Phys.*, **47**:8909–8913, (2008).

[47] V. M. Kugler, F. Söderlind, D. Music, U. Helmersson, J. Andreasson, and T. Lindbäck. Low temperature growth and characterization of (Na, K)NbO_x thin films. *J. Cryst. Growth*, **254**:400 – 404, 2003.

[48] X. Li, X. Wu, W. Ren, P. Shi, and Z. Ye. Preparation and characterization of sodium potassium niobate-silver niobate lead-free films by chemical solution deposition. *Ceram. Int.*, **41**:S228–S233, (2015).

[49] K. Tanaka, H. Hayashi, K. I. Kakimoto, H. Ohsato, and T. Iijima. Effect of (Na,K)-excess precursor solutions on alkoxy-derived (Na, K)NbO_3 powders and thin films. *Jpn. J. Appl. Phys.*, **46**:6964–6970, (2007).

[50] Y. Wang, K. Yao, M. S. Mirshekarloo, and F. E. H. Tay. Effects and Mechanism of Combinational Chemical Agents on Solution-Derived $K_{0.5}Na_{0.5}NbO_3$ Piezoelectric Thin Films. *J. Am. Ceram. Soc.*, **281**:1631–1636, (2016).

[51] H. Bruncková, L. Medvecký, and P. Hvizdos. Effect of substrate on microstructure and mechanical properties of sol-gel prepared (K, Na)NbO_3 thin films. *Mater. Sci. Eng. B Solid-State Mater. Adv. Technol.*, **178**:254–262, (2013).

[52] Helena Brunckovà, L'ubomír Medvecký, Pavol Hvizdoš, and Juraj Ďurišin. Structural and nanomechanical properties of sol–gel prepared (K, Na)NbO_3 thin films. *Surf. Interface Anal.*, **47**:1063–1071, (2015).

[53] F. Söderlind, P.-O. Käll, and Helmersson U. Sol-Gel synthesis and characterization of $Na_{0.5}K_{0.5}NbO_3$ thin films. *J. Cryst. Growth*, **281**:468–474, (2005).

[54] K.-N. Pham. *Potassium Sodium Niobate Thin Films by Chemical Solution Deposition.* PhD thesis, Norwegian University of Science and Technology, 2014.

[55] K. K. T. Lorentzen. Deposition of phase pure KNN thin Films. Master's thesis, Norwegian University of Technology and Science, 2016.

[56] E. R. Camargo and M. Popa, M. Kakihana. Sodium Niobate ($NaNbO_3$) Powders Synthesized by a Wet-Chemical Method Using a Water-Soluble Malic Acid Complex. *Chem. Mater*, **14**:2365–2368, (2002).

[57] E. R. Camargo and M. Kakihana. Chemical Synthesis of Lithium Niobate Powders ($LiNbO_3$) Prepared from Water-Soluble DL-Malic Acid Complexes. *Chem. Mater*, **13**:1905–1902, (2001).

[58] F. Madaro. *Synthesis of textured $K_xNa_{1-x}NbO_3$ materials.* PhD thesis, Norwegian University of Science and Technology, 2010.

[59] Gasperin M. and M. T. Le Bihan. Mecanisme d'hydratation des niobates alcalins lamellaires de formule $A_4Nb_4O_{17}$ (A = K, Rb, Cs). *J. Solid State Chem.*, **43**:346–353, 1982.

[60] F. Madaro, R. Sæterli, J. R. Tolchard, M.-A. Einarsrud, R. Holmestrand, and T. Grande. Molten salt synthesis of $K_4Nb_4O_{17}$, $K_2Nb_4O_{11}$ and KNb_3O_8 crystals with needle- or plate-like morphoplogy. *Cryst. Eng. Comm.*, **13**:1304–1313, 2011.

[61] J. Taub, L. Ramajo, and M. S. Castro. Phase structure and piezoelectric properties of Ca- and Ba-doped $K_{0.5}Na_{0.5}NbO_3$ lead-free ceramics. *Ceram. Int.*, **39**:3555–3561, (2013).

[62] F. Rubio-Marcos, M. G. Navarro-rojero, J. J. Romero, P. Marchet, and J. F. Fernandez. Piezoceramics properties as a function of the structure in the system $(K, Na, Li)(Nb, Ta, Sb)O_3$. *IEEE Trans. Ultrason., Ferroelectr., Freq. Control*, **56**:1835–1842, 2009.

[63] R. D. Shannon. Revised effective ionic radii and systematic studies of interatomic distances in halides and chalcogenides. *Acta Cryst.*, **32**:751–767, Sep 1976.

[64] X. G. Gong and M. Wai. *Strontium : Chemical Properties, Applications, and Health Effects.* Biochemistry Research Trends. Nova Science Publishers, Inc, 2013.

[65] Z. S. Ahn and W. A. Schulze. Conventionally Sintered

$Na_{0.5}K_{0.5}NbO_3$ with Barium Additions. *J. Am. Ceram. Soc.*, **70**:18–21, 1987.

[66] A. C. Fischer-Cripps. *Nanoindentation: Mechanical Engineering Series 1.* Springer Verlag, third edition, 2011.

[67] W. C. Oliver and G. M. Pharr. An improved technique for determining hardness and elastic modulus using load and displacement sensing indentation experiments. *J. Mater. Res.*, **7**:1564–1583, 1992.

[68] W. C. Oliver and G. M. Pharr. Measurement of hardness and elastic modulus by instrumented indentation: Advances in understanding and refinements to methodology. *J. Mater. Res.*, **19**:3–20, 2004.

[69] M. F. Doerner and W. D. Nix. A method for interpreting the data from depth-sensing indentation instrument. *J. Mater. Res.*, **4**:601–609, 1986.

[70] M. Jamal and M. N. Morgan. Materials characterization part i: contact area of the berkovich indenter for nanoindentation tests. *Int. J. Adv. Manuf. Technol.*, **92**:361–370, Sep 2017.

[71] C. Bréchignac, P. Houdy, and M. Lachmani. *Nanomaterials and nanochemistry.* Springer, 2007.

[72] L. Lian and N. Scottos. Stress effects in sol-gel derived ferroelectric thin films. *J. Appl. Phys..*, **95**:629–634, 2004.

[73] A. Barzegar, D. Damjanovic, and N. Setter. Analytical modeling of the apparent d_{33} piezoelectric coefficient determined by the direct quasistatic method for different boundary conditions. *IEEE Trans. Ultrason., Ferroelectr., Freq. Control*, **52**:1897–1903, 2005.

Appendix A

Thermal treatments

A.1 Thermogravimetric standardisation

The molal consentration of niobium in the niobium precursor solution was determined by thermalgravimetric standardisation. This was done by firing the precursor solution in air, using porcelain crucibles with porcelain lids and the temperature program given in Figure 3.3. Kaowool was used in the crucibles to avoid boiling and loss of solution during the firing. Before the standardisation, the crucibles and kaowool were fired at the same temperature program to remove organic materials and other impurities. Three crucibles were used for the standardisation to ensure accuracy in the measurements, and about 10 g of the niobum precursor solution was added to the crucibles. The crucibles were weighed before and after the solution was added, and after the firing. The crucibles were taken out of the furnace at 200 °C, and kept in a desiccator to prevent uptake of moisture from the air. The molality of niobum in the precursor solution was measured, based on the weight of Nb_2O_5 after calcination at 1100 °C, to $0.09940 \pm 5.02\text{x}10^{-5}$ $\mathbf{mmol\,g^{-1}}$solution. Measured weights before and after calcination are given in Table A.1 and the calculated molalities and average molality are given in Table A.2.

Table A.1: Weights measured during standardisation of the niobium precursor solution. All measurements are given in grams. Crucibles mass = Cruc., Kaowool = Kw, Precursor solution = sol. Oxide = Ox.

Mass Cruc.+Kw [g]	**Mass sol.** [g]	**Mass Cruc.+Kw+Ox.** [g]	**Mass Ox.** [g]
21.8362	10.7947	21.9789	0.1427
24.5501	8.8712	24.6680	0.1179
25.0020	11.9988	25.1595	0.1575

Table A.2: Calculation of average (avg) molality of the niobium precursor solution.

Mass Ox. [g]	**Moles Ox.** [mmol]	**MolesNb^{5+}** [mmol]	**Molality** [mmol/g]	**Avg. molality** [mmol/g]
0.1427	0.5368	1.0736	0.09946	
0.1179	0.4435	0.8870	0.09999	0.09940 ±
0.1575	0.5925	1.1850	0.09876	0.0000502

A.2 Calcination temperatures

Table A.3 show the different temperatures, and holding times used during calcination of pre-dried dried powders (160 °C, 12h) from the KNN and Ca-KNN precursor solutions.

Table A.3: List of calcination temperatures ($\mathbf{T_{Calc}}$) and holding times used to prepare powders from the precursor solutions. All precursor solutions were dried at 160 °C for 12 h before calcination.

Precursor solutions	$\mathbf{T_{Calc}}$ **[°C]**	**Time [min]**
KNN00	550	5
KNN00	600	5
KNN00	700	5
KNN25	550	5
KNN25	600	5
KNN25	700	5
KNN25	800	5
KNN50	500	5
KNN50	550	5
KNN50	600	5
KNN50	700	5
KNN50	800	5
Ca05KNN25	500	5
Ca05KNN25	550	5
Ca05KNN25	600	5
Ca05KNN25	700	5
Ca05KNN25	800	5
Ca05KNN25	900	5
Ca05KNN50	500	5
Ca05KNN50	550	5
Ca05KNN50	600	5
Ca05KNN50	700	5
Ca05KNN50	800	5
Ca05KNN50	900	5

Appendix B

Additional X-ray diffractograms

Additional x-ray diffractograms of calcined powders from the KNN00, KNN25, KNN50, Ca05KNN25 and Ca05KNN50 precursor solutions are given in Figure B.1 - Figure B.5, respectively.

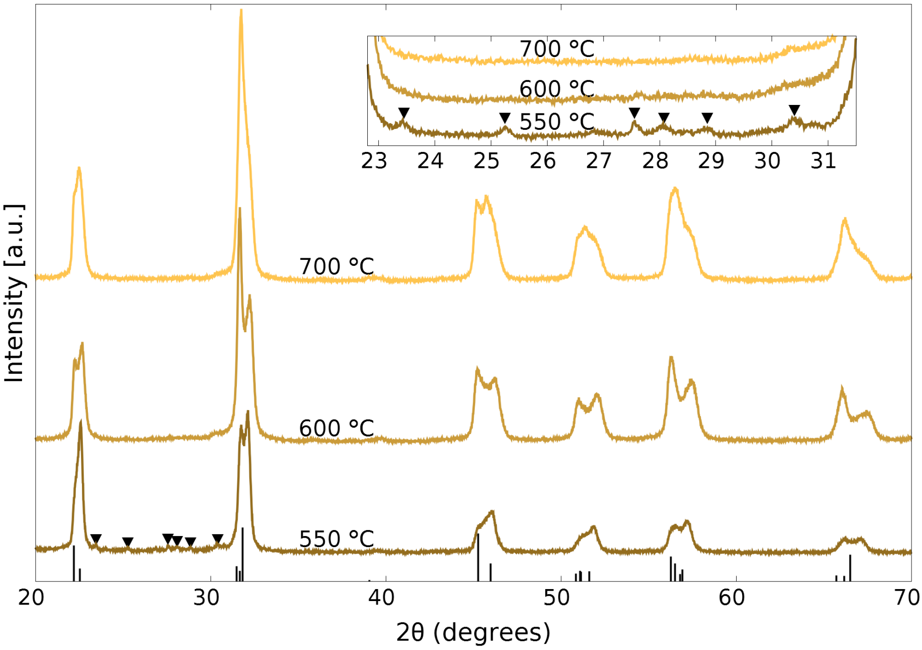

Figure B.1: X-ray diffractogram of KNN powders from the KNN00 precursor solution. ▼ reflections are assigned to $K_4Nb_6O_{17}$. Diffraction lines of $K_{0.5}Na_{0.5}NbO_3$ are included as references at the bottom (black, PDF card 00-061-0315)

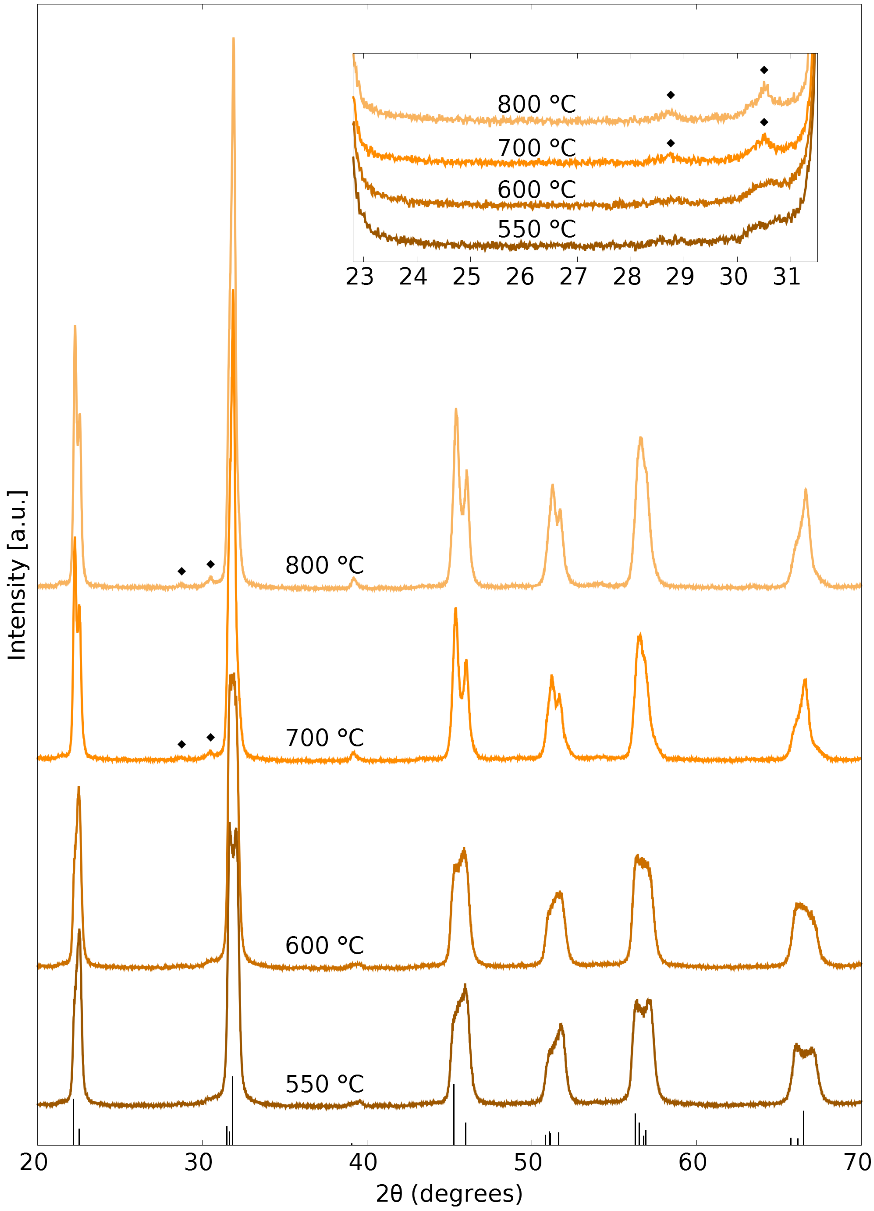

Figure B.2: X-ray diffractogram of KNN powders from the KNN25 precursor solution. ◆ reflections are assigned to Tungsten $K_{\alpha1}$ and $K_{\alpha2}$, and Copper $K_{\beta2}$. Diffraction lines of $K_{0.5}Na_{0.5}NbO_3$ are included as references at the bottom (black, PDF card 00-061-0315)

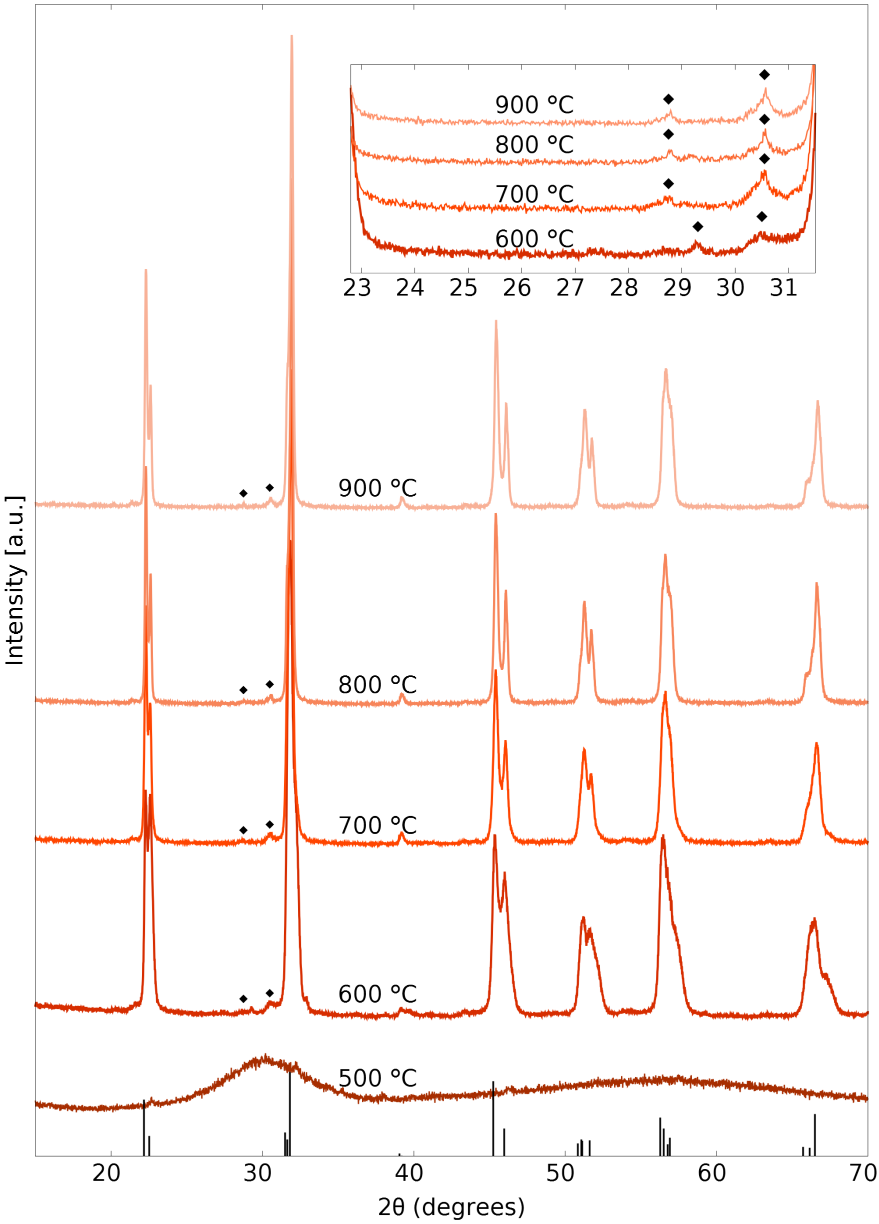

Figure B.3: X-ray diffractogram of KNN powders from the KNN50 precursor solution. ◆ reflections are assigned to Tungsten $K_{\alpha1}$ and $K_{\alpha2}$, and Copper $K_{\beta2}$. Diffraction lines of $K_{0.5}Na_{0.5}NbO_3$ are included as references at the bottom (black, PDF card 00-061-0315

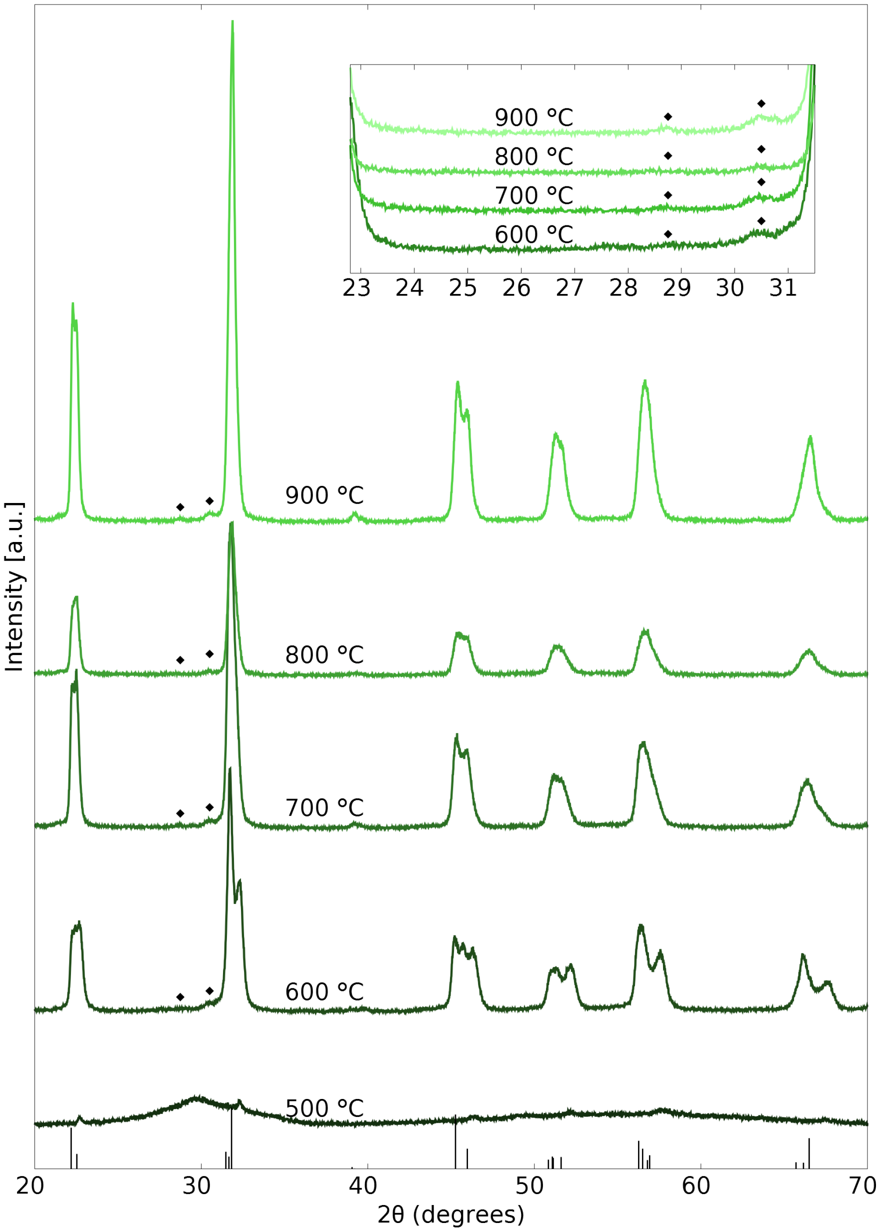

Figure B.4: X-ray diffractogram of Ca-KNN powders from the Ca05KNN25 precursor solution. ◆ reflections are assigned to Tungsten $K_{\alpha 1}$ and $K_{\alpha 2}$, and Copper $K_{\beta 2}$. Diffraction lines of $K_{0.5}Na_{0.5}NbO_3$ are included as references at the bottom (black, PDF card 00-061-0315

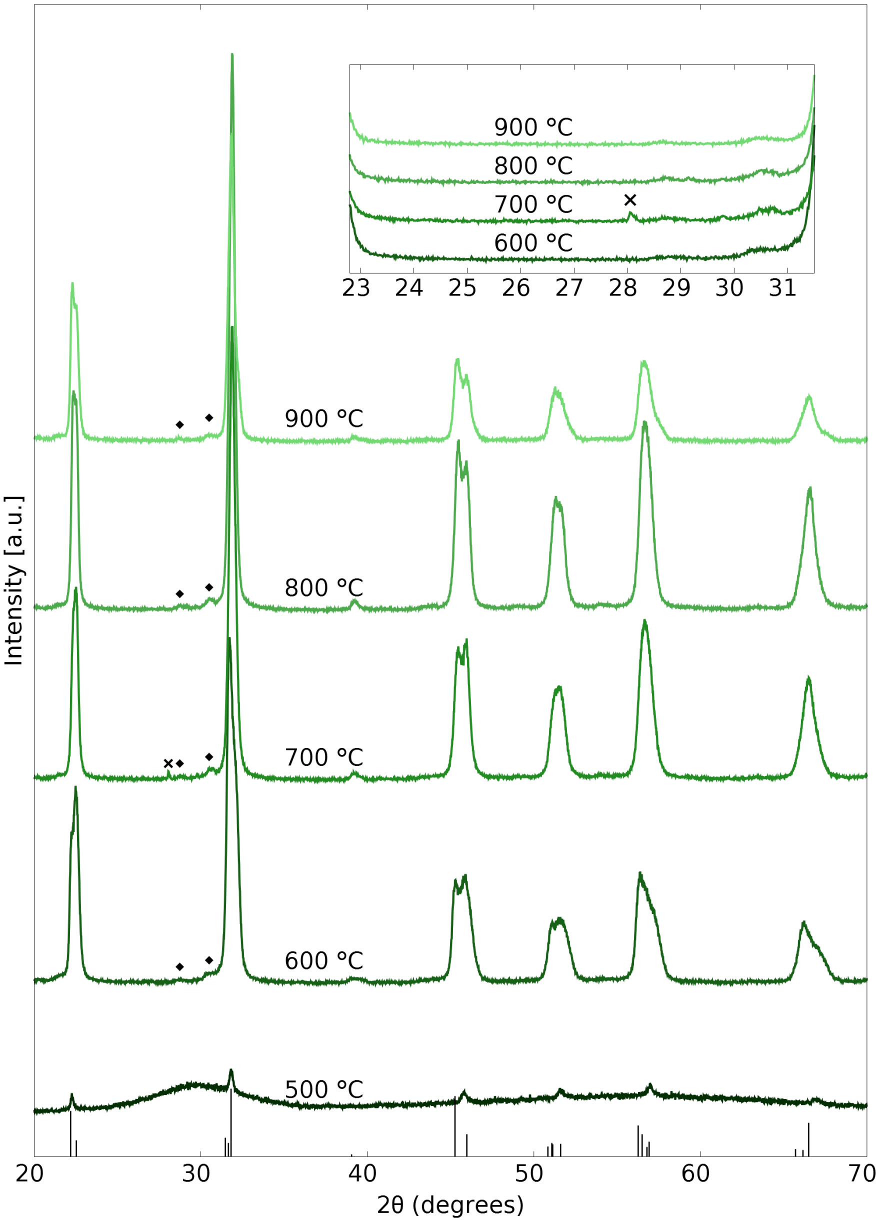

Figure B.5: X-ray diffractogram of Ca-KNN powders from the Ca05KNN50 precursor solution. ♦ reflections are assigned to Tungsten $K_{\alpha1}$ and $K_{\alpha2}$, and Copper $K_{\beta2}$. × reflection is assigned to an unknown phase. Diffraction lines of $K_{0.5}Na_{0.5}NbO_3$ are included as references at the bottom (black, PDF card 00-061-0315

Appendix C

Pawley refinements

Pawley refinements (within the space group *Pm*) of the diffractorgrams for the KNN25, Ca05KNN25 and Ca05KNN50 samples calcined at **800** °C, are given in Figure C.1, Figure C.2 and Figure C.3, respectively.

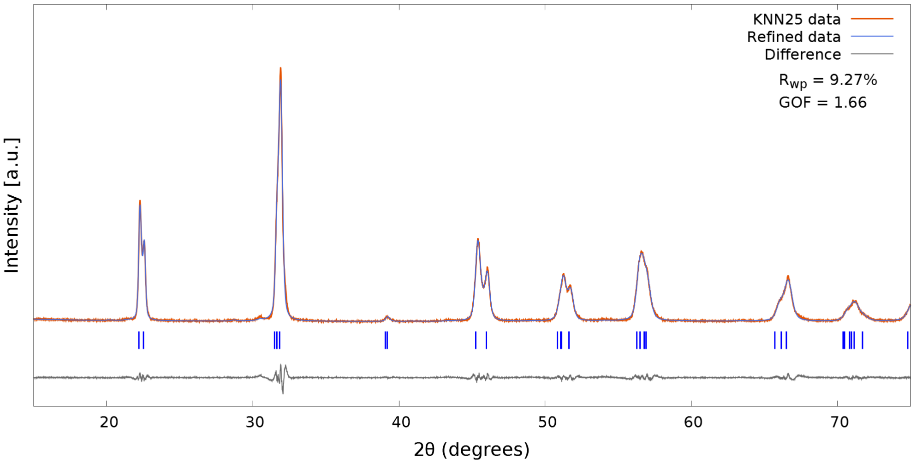

Figure C.1: Pawley refinement of KNN25 precursor solution powder, within the *Pm* space group.

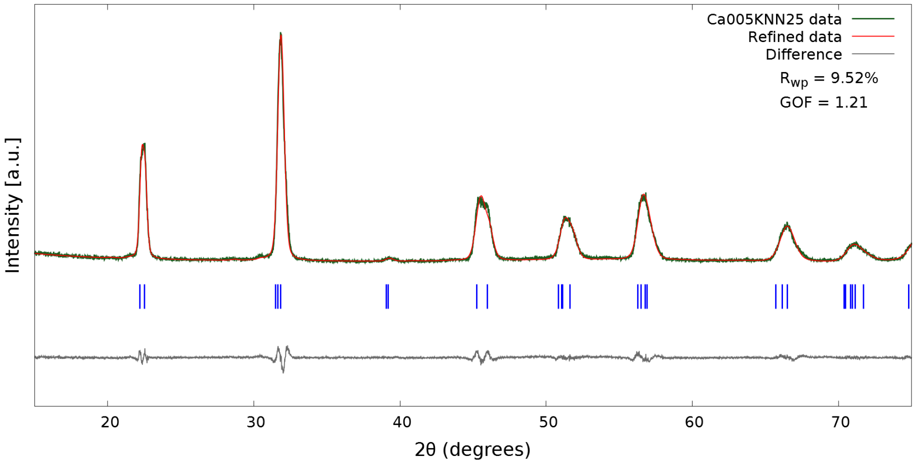

Figure C.2: Pawley refinement of Ca005KNN25 precursor solution powder, within the *Pm* space group.

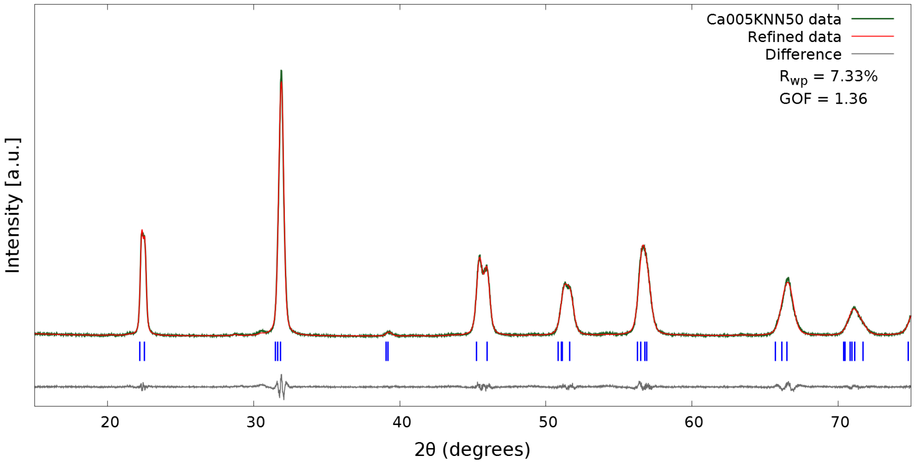

Figure C.3: Pawley refinement of Ca005KNN50 precursor solution powder, within the *Pm* space group.

Appendix D

Surface morphology

Figure D.1 show the development of potential bacteria on the surface of KNN25 thin films during soaking in disilled water at 37 °C. Additional scanning electron microscopy (SEM) images of the surface of KNN25 and Ca05KNN25 thin films at higher magnification are shown in Figure D.2 - Figure D.9.

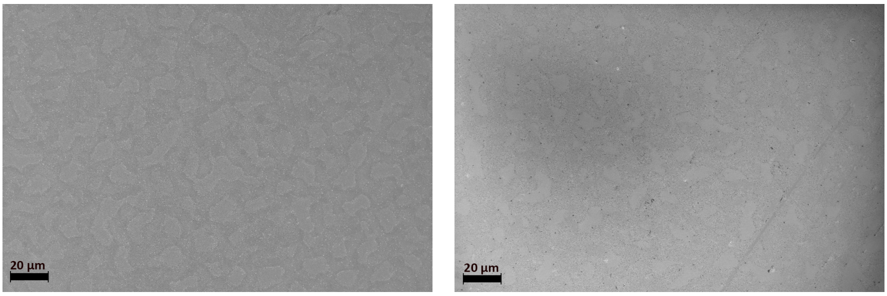

(a) Non-soaked **(b)** 1 day

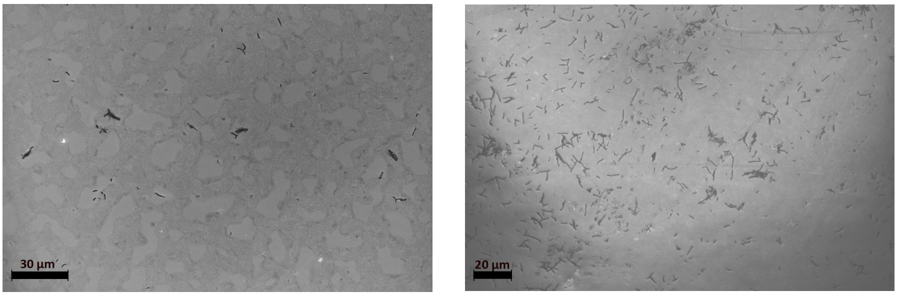

(c) 3 days. **(d)** 6 days

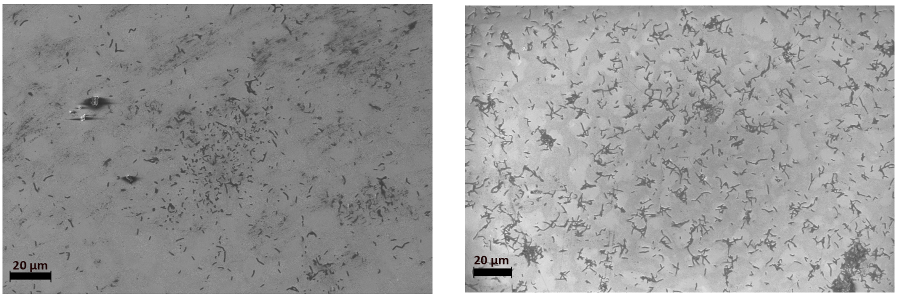

(e) 10 days **(f)** 14 days

Figure D.1: SEM images of KNN25 thin films showing the development of potential bacteria on the surface during soakingtime.

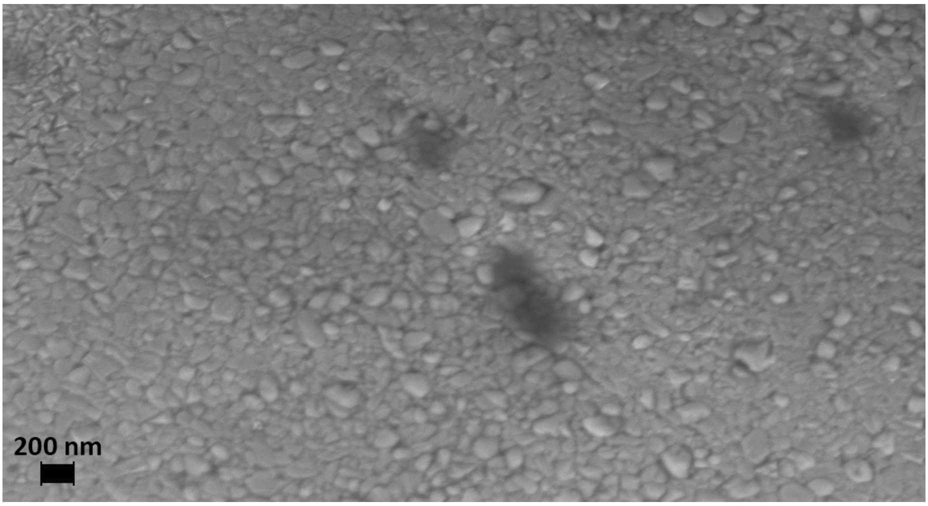

Figure D.2: SEM image showing the microstructure of the KNN25 thin film after being soaked for 1 day.

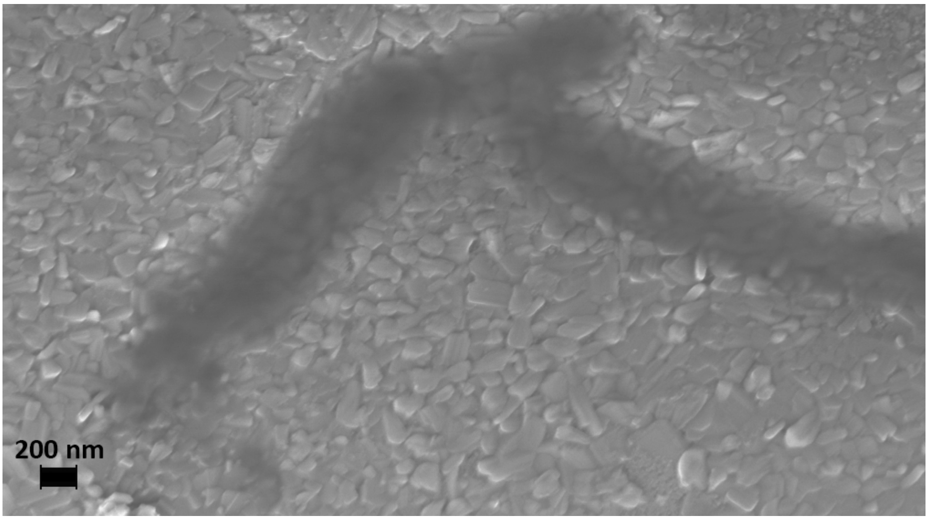

Figure D.3: SEM image showing the microstructure of the KNN25 thin film after being soaked for 6 days.

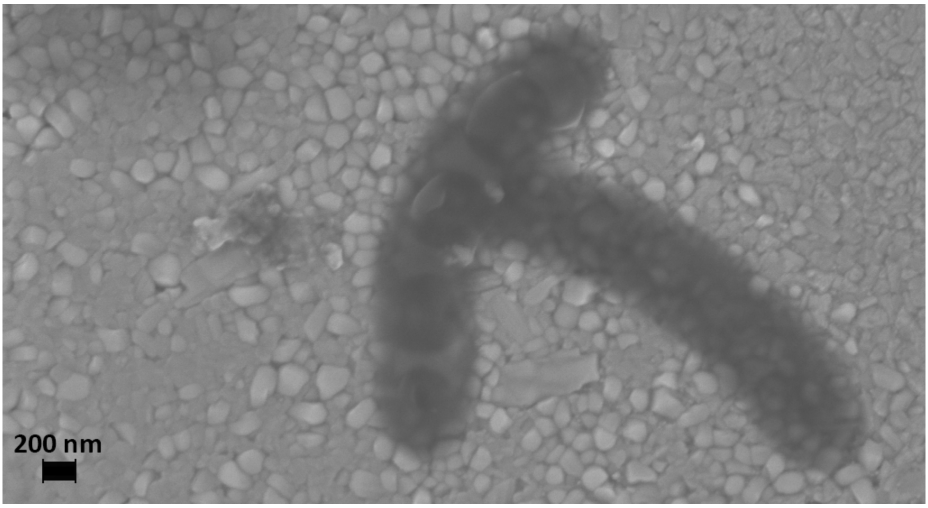

Figure D.4: SEM image showing the microstructure of the KNN25 thin film after being soaked for 10 days.

Figure D.5: SEM image showing the microstructure of the KNN25 thin film after being soaked for 14 days.

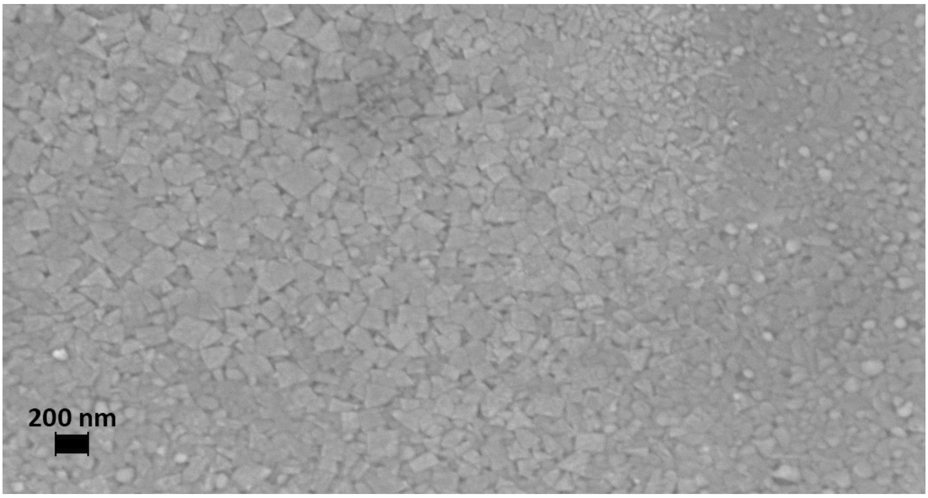

Figure D.6: SEM image showing the microstructure of the Ca05KNN25 thin film after being soaked for 1 day.

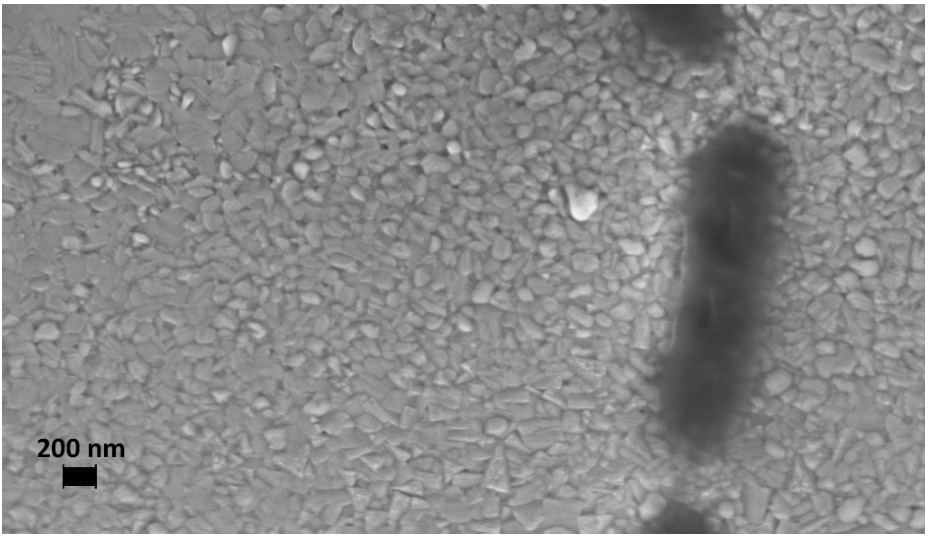

Figure D.7: SEM image showing the microstructure of the Ca05KNN25 thin film after being soaked for 6 days.

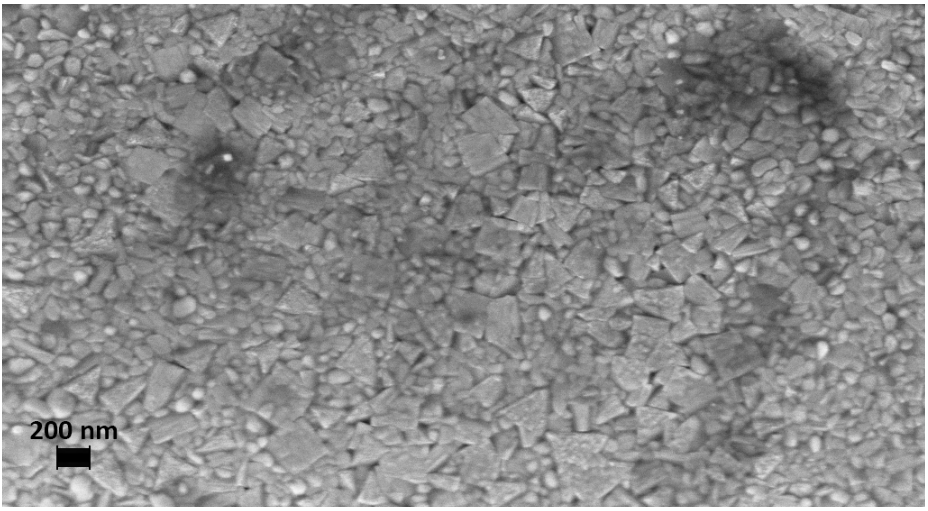

Figure D.8: SEM image showing the microstructure of the Ca05KNN25 thin film after being soaked for 10 days.

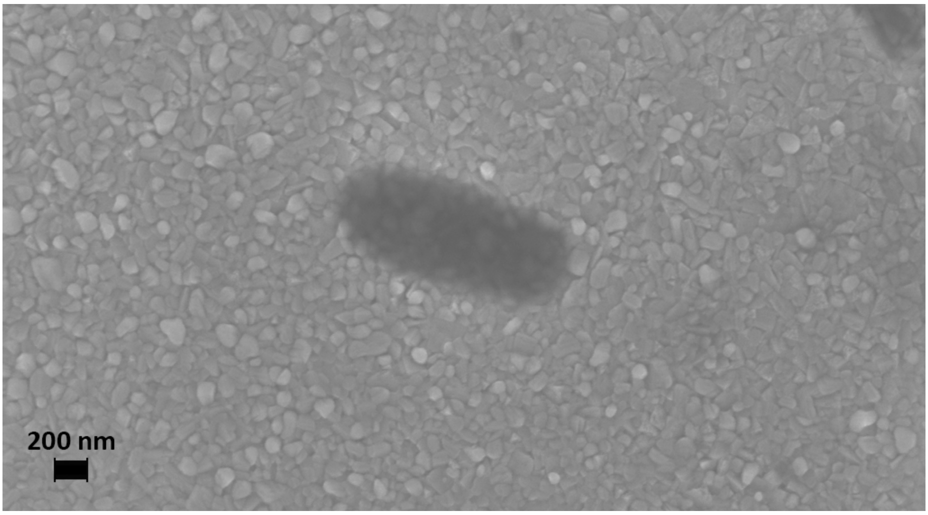

Figure D.9: SEM image showing the microstructure of the Ca05KNN25 thin film after being soaked for 14 days.

Appendix E

Nanoindentation

Calculated reduced modulus, hardness and standard deviations obtained from the nanoindentation experiments preformed on the KNN50 and Ca05KNN50 thin films are given in Table E.1, and in Table E.2 for the KNN25 and Ca05KNN25 thin films. Recorded loading-displacement curves from the nanoindendation experiments are given in Figure E.1, Figure E.2, Figure E.3 and Figure E.4 for the KNN25, Ca05KNN25, KNN50 and Ca05KNN50 thin films, respectively.

Table E.1: Calculated reduced modulus (E_r), Hardness (H), standard deviations (Std.Dev.) and number of indents (#Ind) from the nanoindentation experiments preformed on KNN50 and Ca05KNN50 thin films.

Sample	$\mathbf{E_r}$**[GPa]**	**Std.Dev.**	**H[GPa]**	**Std.Dev.**	**# Ind**
Ca05KNN50-14	189.97	15.81	9.01	1.35	9
Ca05KNN50-6	201.29	13.20	10.18	1.27	9
Ca05KNN50-2	202.88	24.57	8.91	1.83	9
Ca05KNN50-0	195.88	7.50	10.31	0.82	9
KNN50-14	205.79	15.79	9.35	1.98	9
KNN50-6	200.46	16.05	9.19	1.14	9
KNN50-2	172.74	5.45	6.22	0.45	9
KNN50-0	210.77	24.46	10.75	1.99	9

Table E.2: Calculated reduced modulus (E_r), Hardness (H), standard deviations (Std.Dev.) and number of indents (#Ind) from the nanoindentation experiments preformed on KNN25 and Ca05KNN25 thin films.

Sample	$\mathbf{E_r}$**[GPa]**	**Std.Dev.**	**H[GPa]**	**Std.Dev.**	**# Ind**
Ca05KNN25-14	176.86	24.17	7.29	1.13	6
Ca05KNN25-10	245.87	99.547	17.13	11.58	6
Ca05KNN25-6	181.99	41.51	8.35	3.35	9
Ca05KNN25-3	166.21	51.13	9.00	6.74	9
Ca05KNN25-1	191.23	44.08	9.64	3.92	9
Ca05KNN25-0	165.86	58.64	12.12	6.21	9
KNN25-14	159.35	63.73	7.08	5.09	8
KNN25-10	159.12	30.57	6.68	2.50	7
KNN25-6	206.99	52.77	11.53	6.79	9
KNN25-3	165.62	26.95	6.25	1.72	9
KNN25-1	195.15	41.66	8.76	2.39	9
KNN25-0	193.20	100.16	15.78	16.95	9

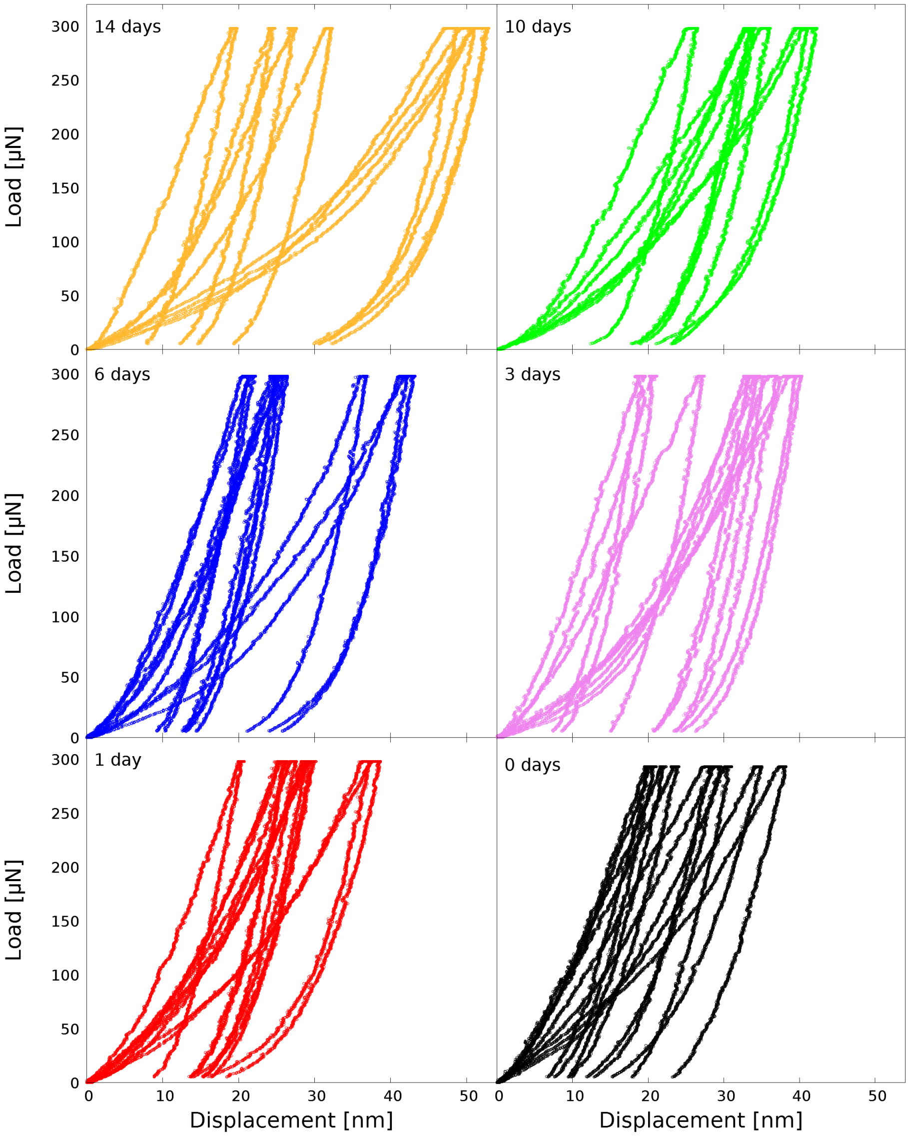

Figure E.1: All loading-displacement curves for the KNN25 thin films.

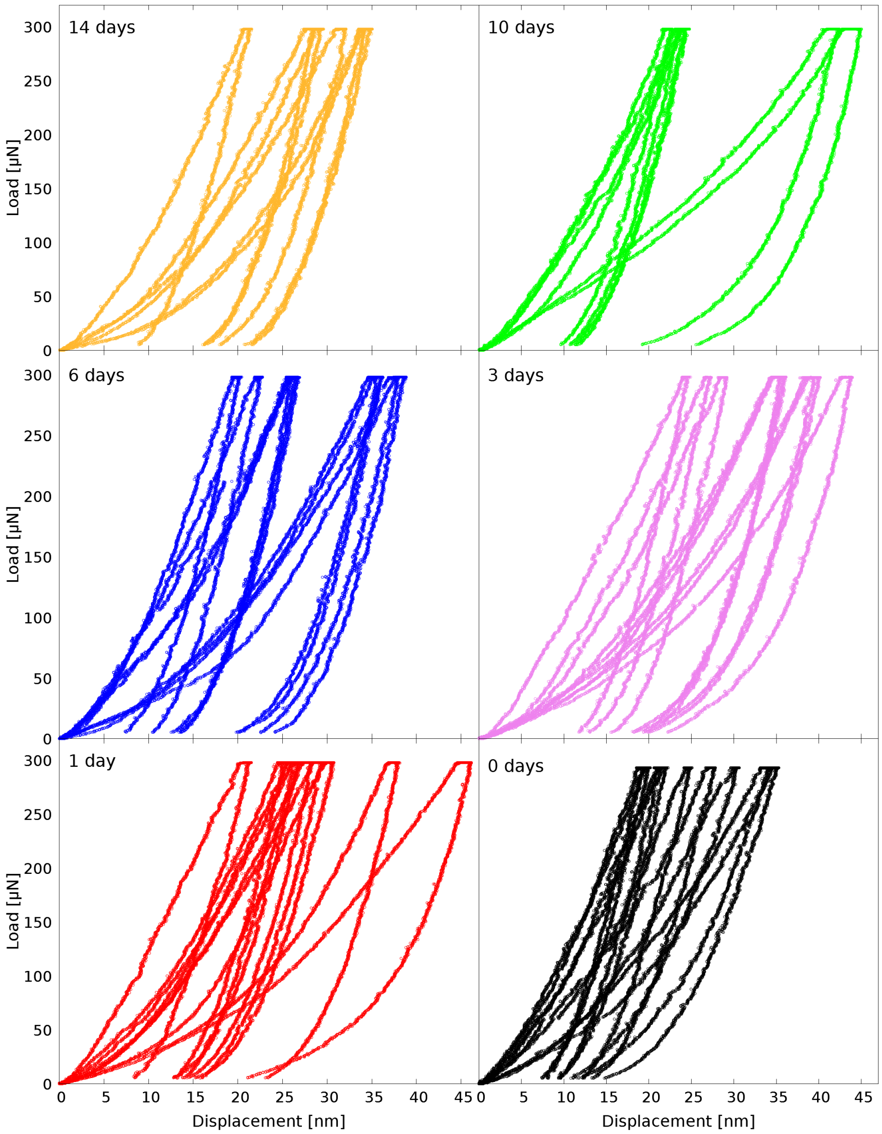

Figure E.2: All loading-displacement curves for the Ca05KNN25 thin films.

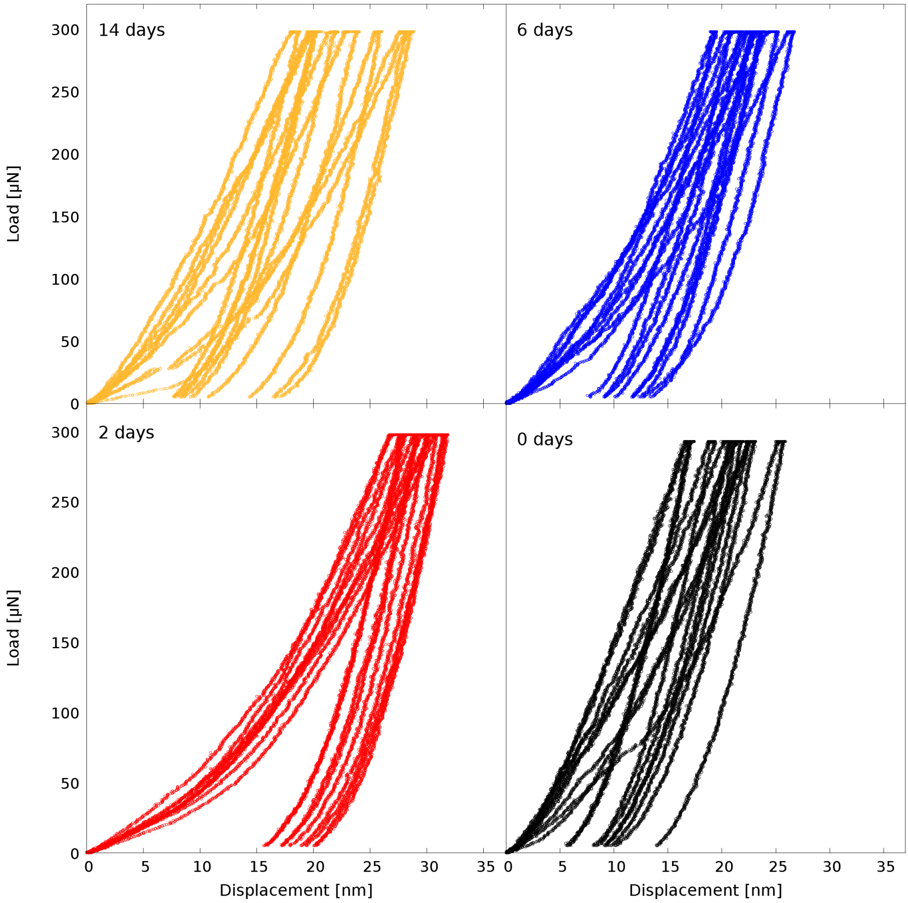

Figure E.3: All loading-displacement curves for the KNN25 thin films.

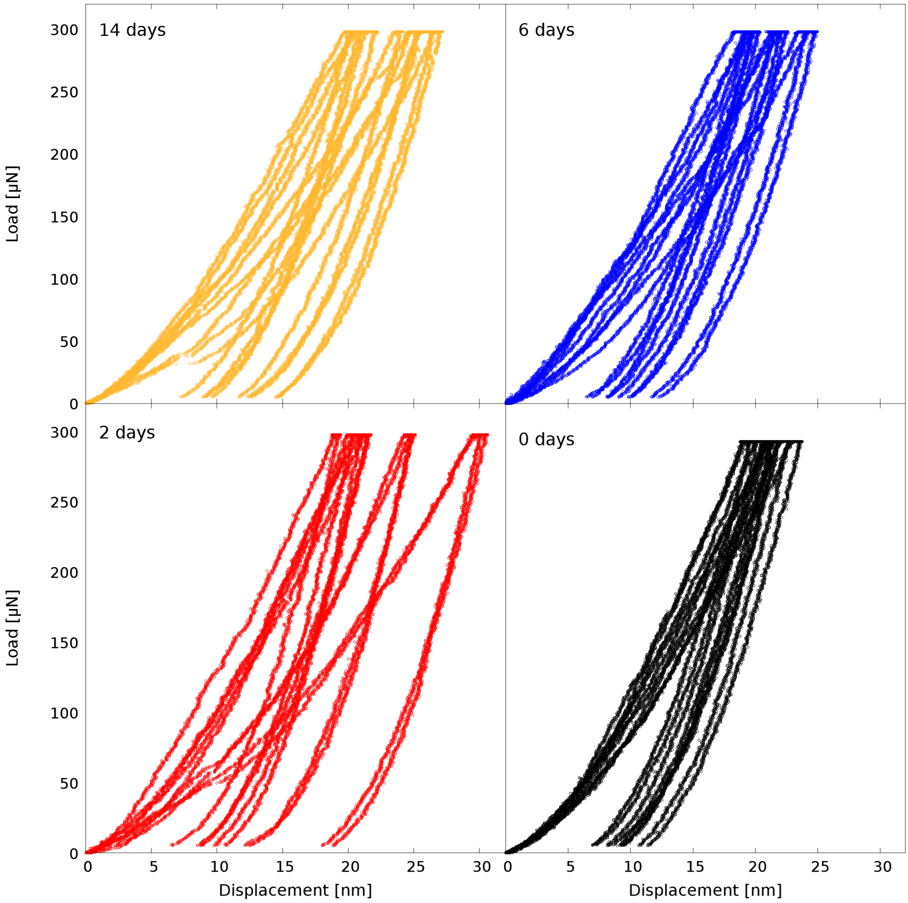

Figure E.4: All loading-displacement curves for the Ca05KNN25 thin films.